Part I
Wind Turbine Blades

Chapter 2
Design of Wind Turbine Blades

Malcolm McGugan

Abstract In this section the research program framework for European PhD network MARE-WINT is presented, particularly the technology development work focussing on reliability/maintenance and the models describing multi-body fluid structure interaction for the Rotor Blade structure. In order to give a context for the effort undertaken by the individual researchers this section gives a general background for Wind Turbine blades identifying the trends and issues of importance for these structures as well as concepts for "smarter" blades that address these issues.

2.1 Rotor Blades as a Common Research Topic

In order to meet its objective of strengthening the fundamental scientific work within the multi-disciplinary engineering field of hydro-aero-mechanical coupling in the wind energy conversion process, the MARE-WINT project was organised as five cross-linked work packages in a common research programme. The first three research work packages focus on the major structural components of the Offshore Wind Turbine; Blade, Drive train, and Support structure. In addition to these independent structure based work packages, there were two consolidating technology based work packages focussing on Reliability and Predictive maintenance, and Fluid–Structure interaction. In this way the goal of integrating multiple disciplines was to be achieved. This concept is visualised in Fig. 2.1 where the three vertical, structure-based Work Packages, are connected by the two horizontal technology-based Work Packages.

Work Package 1 is the focus of this chapter and concerns the challenges for offshore wind turbines with regard to the rotor blades, as well as proposing an innovative response to address these. Within the network two researchers were allocated within Work Package 1; Gilmar Pereira, based at the Technical University of Denmark (DTU) and Vladimir Leble, based initially at the University of Liverpool, and later at the University of Glasgow. In addition three researchers in the network allocated within Work Packages 4 and 5 conducted work at the nexus

M. McGugan (✉)
Department of Wind Energy, Technical University of Denmark (DTU), DTU Risø Campus, Frederiksborgvej 399, 4000 Roskilde, Denmark
e-mail: mamc@dtu.dk

W. Ostachowicz et al. (eds.), *MARE-WINT*, DOI 10.1007/978-3-319-39095-6_2

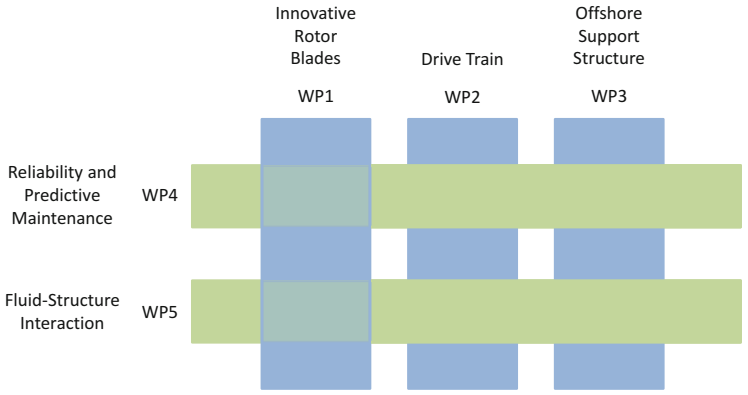

Fig. 2.1 Diagram showing the cross-linked MARE-WINT Work Packages

between their technology area and the blade structure. Borja Hernandez Crespo, based at The Welding Institute in Cambridge, worked on Reliability and Predictive Maintenance for the blades, and Alexander Stäblein worked with wind turbine blade Fluid–Structure Interaction models at DTU Wind Energy, as Javier Martinez Suarez did at the Institute of Fluid-Flow Machinery in the Polish Academy of Sciences.

In Work Package 1 the structural and fluid dynamic investigations on the rotor blade are approached by numerical and experimental methods. Within the work package individual projects were developed, the first considering the behaviour of the composite material (particularly when in damaged condition) within the blade structure and the use of embedded sensors to detect this behaviour, and the second describing structural behaviour and rotor performance in Computational Fluid Dynamics models, including the use of leading and trailing edge flaps to modify this.

These activities cross-link with the combinatory horizontal work packages (4 and 5) by providing, among other things, structural health information to the reliability and predictive maintenance work package, and input to the fluid–structure interaction models developed for the entire turbine.

In Work Package 4 the prime consideration is the economic efficiency of an offshore wind farm as depending upon the individual turbines availability and reliability. For the blades this involves the study of the various damages observed in service, and understanding their root causes and criticality with respect to operational lifetime. Detecting damages that initiate and propagate during service is not straightforward and developing inspection technologies alongside remote sensing systems is a key part of the future optimisation in this area.

In Work Package 5 the structural description of the various Offshore Wind Turbine components are combined with flow models in a fluid–structure interaction description of the complete system. The key task involves identifying and integrating the various aero/hydro loadings and their effect on the structural responses, particularly any coupled effects. Of the three researchers in Work Package 5,

two worked specifically on the complex blade structure. The areas of interest here include the use of twist-coupled aeroelastic blades to achieve structural load reduction at high wind loads, and the development of flow control technology for advanced blades.

In order to provide a common platform for the different Work Packages, a reference model was agreed as one of the first deliverables within the project. Described by Bak et al. (2013), the DTU 10 MW reference wind turbine was developed by DTU Wind Energy together with Vestas Wind Systems as part of a collaborative research intended to create the design basis for the next generation of wind turbines. As such it is an ideal, publically available reference for MARE-WINT to work on the optimisation of large offshore wind installations; and indeed many of the inputs within this chapter use this shared reference.

2.2 General Background for WT Blades

Access to affordable, reliable, sustainable and modern energy is one of the 2030 targets for the United Nations (UN 2016). This requires a substantial increase in the share of renewable energy within the global energy mix, and wind is a prominent part of the solution if the world is to achieve such a target. The potential for offshore wind energy is enormous with industry projections in Europe showing an increase from 5 GW in 2012 to 150 GW in 2030 (European Wind Energy Association, Fig. 2.2 (EWEA 2016)). By moving to offshore sites the Industry can establish larger wind farms with turbines of a size that would not be easily accepted onshore where land use is at a premium. In addition to this, the quality of the wind resource is greatly improved away from the effect of land contours, forests, and so on.

However, moving such a large portion of the industrial production capacity offshore is a major challenge. The environment offshore can be extreme and requires a more robust and durable design for all components, access is expensive for establishing and maintaining production offshore, and support structure designs for deep water sites are yet to be proven commercially. At the European Wind Energy Association conference in 2014, the delegates were warned that without a reduction in energy costs corresponding to at least 40 %, offshore wind could not persist in the current energy market beyond 2020 (EWEA 2014). While costs for onshore wind are already competitive, targeting a reduction in the cost of energy offshore was vital if the ambitious political and industrial targets are to be achieved. It was further observed that initial offshore developments were based on technology from the offshore oil and gas supply chain which is driven by a need to maximise production, rather than by cost reduction. The solution agreed was for a more focussed investment in research and development that produces innovations in logistics, transport and operation.

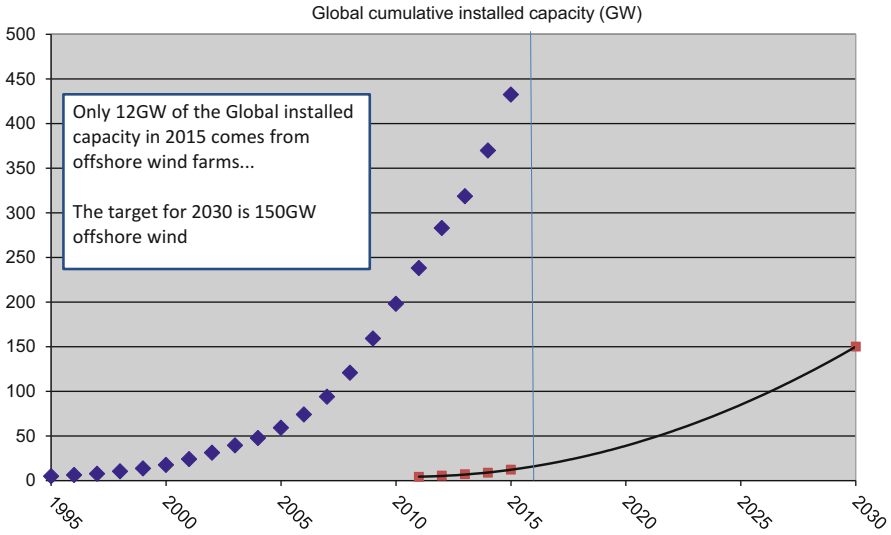

Fig. 2.2 Growth in Wind Energy capacity from 1995 to 2015 (data available on www.gwec.net)

Table 2.1 Comparison example between commercial turbines developed by Vestas in 2000 and 2015

Year	Manufacturer (rotor diameter)	Effect	Tip height
2000	Vestas Wind Systems V52	2.5 MW	70 m
2014	Vestas Wind Systems V164	8.0 MW	222 m

One of the most eye-catching developments in the wind energy industry over the last 15 years has been the increase in the size of the turbines being manufactured with new turbine designs consistently providing larger turbines with higher power ratings, as shown in Table 2.1.

As the rotors become larger, the industry has relied on improvements in blade structural design, manufacturing processes and material properties in order to meet the requirements for ever longer blades that remain light-weight, strong and stiff. It can be argued that the blades present the most challenging materials, design and engineering problems being a complex, anisotropic material in an aerodynamic structure that is subjected to continuous dynamic loadings of a combined and non-uniform nature over long periods of time. These operational requirements and conditions lead to materials that must exhibit a high stiffness, a low density, and long fatigue life.

Material performance criteria therefore identify fibre reinforced polymer composites as the prime candidate for rotor blades. Here the stiff fibres (usually glass, sometimes carbon) are aligned in the primary load directions within a cured matrix of resin (usually thermosetting polyester or epoxy). The processing technology for such material (whether pre-preg, resin infusion, or wet layup) involves considering the material properties, design approach and manufacturing process as an integrated

issue as already at this stage the characteristics of the material (and hence the behaviour of the final structure) are determined. For example, in longer rotor blades the reinforcing (stiffening) fibres must be aligned along the length of the blade, but with sufficient understanding of the out-of-plane properties and weak laminate interfaces and bond lines so as not to generate problems with durability when the complex combined loads are encountered.

Blade design combines a relatively thin shelled aerodynamic profile supported by a longitudinal beam or webs which carry the bulk of the structural load. The blades are heavier at the root section and taper towards the tip to match the load distribution in a cantilever beam structure and maintain the allowed material strain levels. Industry demands have spurred improvements in design with an optimised aerodynamic profile, relative reduction in weight for longer blades and integrated bend-twist coupling into the structural response.

For much more on material and structure requirements for wind turbine blades see Brøndsted and Nijssen (2013).

The design philosophy for rotor blades (as with all fibre reinforced polymer structures) began with large safety factors and addressing simple issues of linear elastic behaviour. With time, as knowledge about the materials, structural behaviour and manufacturing approaches increased (coupled with the pressure to make more daring multi-MW designs) it became possible to adopt more advanced structural design approaches. The development in light weight structure design is nicely illustrated in a general way by Braga et al. (2014) and here we see that an implementation of "smart" structure technology is the anticipated innovation to supersede the current state of the art not only for offshore wind turbine blades, but also in other industries where polymer composites are utilised.

Recent trends in the wind energy industry can be summarized as follows:

- A rapid increase in the level of installed capacity world-wide
- An increase in the physical size (dimensions) of the structures
- An increase in the size (number of multi-MW turbines) of individual wind farms
- A tendency to place these wind farms offshore
- Higher industry requirements for reliability, safety and easy maintenance
- A strong focus on a reduction in the cost per "unit" of energy produced
- New materials, designs, and production methods continuously adopted

2.3 Innovative Blade Concept

As the most effective way to increase the power produced per turbine is to make each turbine bigger, we now have an industry that manufactures extremely large rotor blades using low-cost fibre composite material and low-cost manufacturing methods. A consequence of the components in a wind turbine blade being so large (in some companies almost the entire structure is manufactured in one piece via resin infusion of dry laminate layers), is that there is little scope for improving the

performance of a finished blade by rejecting parts that do not meet very high quality standards. This is because the low-cost manufacturing approach demanded by the industry makes manufacturing a "perfect" blade challenging, and parts thus rejected would be too costly to simply discard.

Instead the situation is that each blade has a unique set of "variations" (we might call then defects) from the intended "perfect" design; these are then more or less mitigated with repair technology before leaving the factory. And in operation the specific load profile will also vary for each turbine. Without detailed information about the distribution of structural/material defects and repairs present, combined with detailed loading and response history for each blade, it will be impossible to make accurate predictions about the lifetime performance of these blades individually; only a generalised probability analysis is possible. And prescribing regular manual inspection is neither an economical nor technically efficient solution to control the health of the structures as for large offshore farms this would be both costly and difficult.

Having an isolated understanding of the individual stages in the wind turbine blade operational life, such as manufacturing, operational, emergency situations, repairing, etc., is therefore not enough to achieve a smart wind turbine blade concept. Rather knowledge of how each stage interconnects with the processor and successor, and the impact of a change in any of the properties to the individual wind turbine blades operational life is required. The traditional Mono-Stage design and methodology, as shown in Fig. 2.3, is no longer applicable to match this requirement; especially as blades become larger, more complex and expensive to manufacture, more information feedback is required to maximise their lifetime and improve processes.

Thus, methods to measure and evaluate structural integrity and operational parameters through all the wind turbine blade life stages need to be implemented from the design stage (McGugan et al. 2015).

The smart blade design and methodology is shown in Fig. 2.4. The presence of sensors integrated in the structure since manufacture will provide feedback at each stage of the structure life time. For example, if during an extreme load a change in

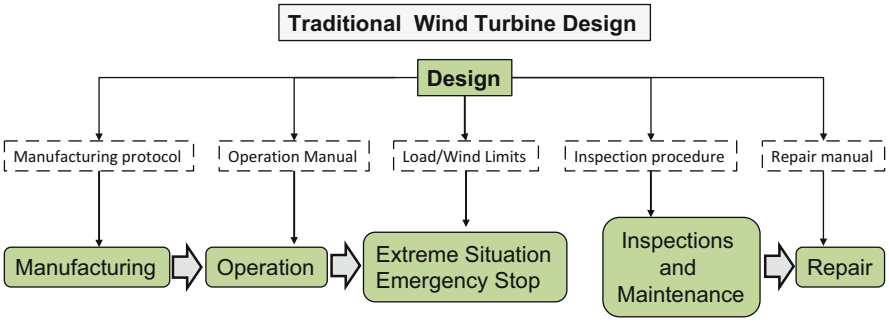

Fig. 2.3 Life stages of a wind turbine blade: traditional design methodology

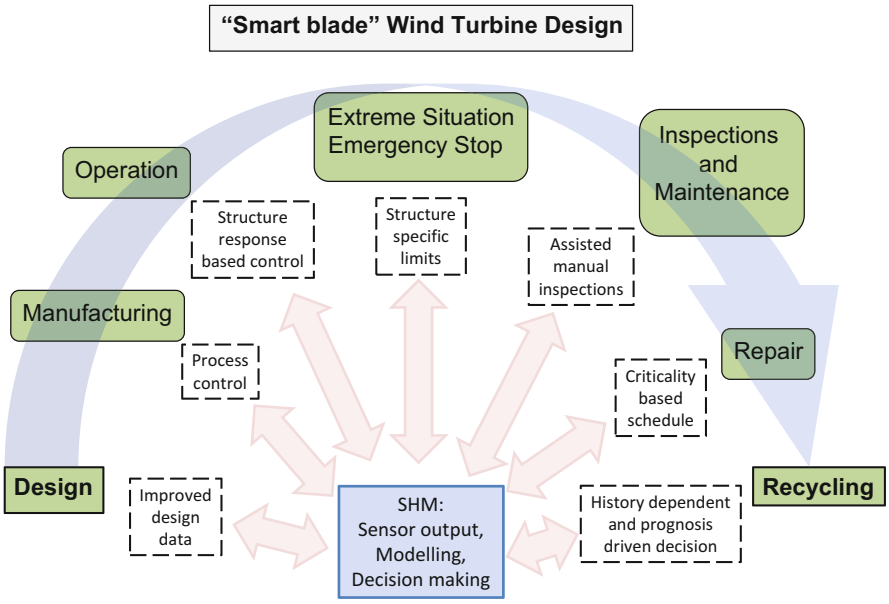

Fig. 2.4 Life stages of a wind turbine blade: "smart-blade" design methodology

the material stiffness is detected, caused by delamination or a crack in the adhesive joint, the wind turbine operation limit can be decreased based on this information. This will enable the structure to operate safely until the next repair action, continue to generate energy, and minimise monetary loses.

Structural Health Monitoring is a well-known engineering area concerned with assessing the current state of a specific asset in order to ensure proper performance. It has the perspective to function both as an automated (and remote) maintenance and inspection process, as well as a "smart" structure feedback allowing activation and response based on condition and environment.

The novel approach proposed is thus that blades are allowed to contain defects and develop stable damage under operation as under the current "passive" damage tolerant design philosophy. But the implementation of structural feedback from the embedded sensors and active response is combined with improved damage tolerant materials and design methods in order to expand the current design philosophy and include SHM and applied fracture mechanics from the initial concept. This allows a design that ensures any defects present cannot develop into unstable damage that leads to blade failure. Furthermore, a full life-time perspective is given that enables a holistic optimisation of the structural resources.

2.4 Operational Concept

Many industrial sectors share similar ambitions regarding polymer composite structural materials, structural diagnosis, and development of prognostic approaches. However each one differs in how they intend to exploit the new technology and apply the new developments. The different expectations and priorities across the sectors will influence the entire design, processing, and maintenance line. For example, the aerospace sector can be characterised by polymer composite structures that are high cost material and high value structures, whereas the wind energy sector considers the rotor blades as low cost material and high value structure.

In practice this means that a common "toolkit" of deliverables and work areas exist for defining a physics-based polymer composite structural component life analysis that can be investigated by researchers and industry across different sectors. However from this "open-source" framework, sector specific implementations will then be developed.

The upper part of Fig. 2.5 shows the concept of a blade structure operational lifetime being "consumed" during its' use in a more or less controlled and progressive manner throughout the planned service life. The usage depends on a loading input which is monitored and understood and in some cases controlled (active management) to a greater or lesser extent.

This control could be in the form of a simple measurement of wind speeds and a calculation of the resulting aerodynamic loads on the structure which provide a "cut off" wind speed above which the turbine should not be permitted run (in part to avoid overload situations). Progressively more advanced turbine control systems can include passive bend-twist blade designs, an active control of pitch and leading/trailing edge settings combined with turbine specific in-flow measurements

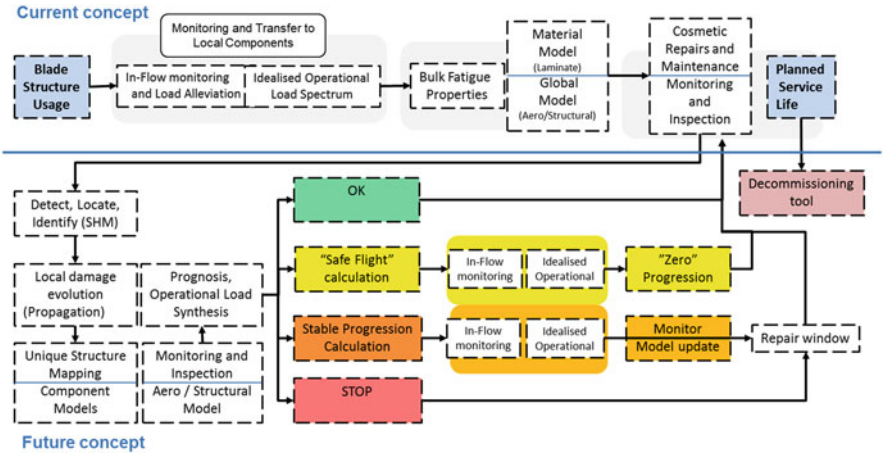

Fig. 2.5 Health Management Concept for future Innovative Rotor Blades

to allow for load alleviation from tower shadow effects, shear loads, turbulence, and so on. The degree of structure control available will define the quality of the load spectra applied and specify the risk of stochastic peak loads that can progress (or initiate) damage. The greater the degree of control, the more availability a damaged structure can exhibit. The availability of a distributed in-situ load monitoring capability will enhance aerodynamic load control options.

Moreover, combining Structural Health Monitoring with other inspection technology will detect and characterise localised damage for each structure, generating a "damage map" for each wind turbine blade with local and global damage models communicating to define critical (and sub-critical) failure criteria. A prognosis tool based on the local forecast of operation can propose the suitable structural sustainment action:

- an unaltered operation (exploiting the passive/designed damage tolerance capability of the material/structure)
- a modification of the structure control settings to limit load conditions that risk progressing damage (a "safe flight" operation)
- an operation of the structure that will allow a progression of damage but in a stable regime allowing repair to be scheduled for the next available maintenance period
- or an immediate stop pending critical repair

In all cases the target for the individual structures is to meet the planned service life whereupon "problem" structures can be decommissioned and the remainder assessed for the feasibility of an extended operational lifetime. The updated database of structural integrity information generated by this process improves the decision making regarding which structures can be safely licensed for continued operation and those that need to go to refit, resale, or recycling.

2.5 Research and Development Work Supporting the Concept

The work carried out by the MARE-WINT researchers associated with Work Package 1 supports the implementation of this new operating concept for wind turbine blades across a broad area of material and structural advances. Each area of research and development is a valuable and acknowledged area of technology in and of itself and includes failure and damage mechanics, new sensing techniques, load spectra monitoring, characterisation of structural damages, data acquisition and analysis, handling environmental effects and other sources of uncertainties, residual properties prognosis, and the assessment of various maintenance and damage mitigation actions. The challenge for the adoption of innovative blade concepts is to combine the many fields into a multi-disciplinary technology within the minds of the next generation of designers and engineers.

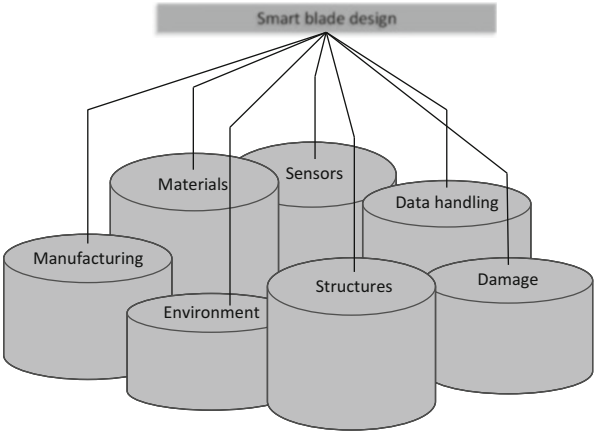

Fig. 2.6 Independent technology platforms supporting a "Smart" blade design concept

This idea of a set of independent technology platforms that can be combined to support a specific "smart" design concept is illustrated in Fig. 2.6. Note that the names of the technology platforms are illustrative only and far from exhaustive.

In Chap. 3 the topic of damage in composite materials and structural failures in the blades is discussed. In conjunction with the deepening understanding of the causes and effects of these, technology developments are also underway to provide remote sensing solutions and release the pressure on manual inspection procedure. Monitoring this degradation of structural material via manual Non-Destructive Inspection (NDI) during the service lifetime is an expensive, hazardous, and inefficient proposal for offshore wind farms. Therefore, integrating various robust and inexpensive remote sensing technologies and developing them to detect the most common and/or most critical of in-service failures is a clear target for research groups. The demands for improved material performance to achieve the structural designs for extremely long multi-Megawatt blades has propelled research in composite material fabrication, minimising imperfections and improving understanding of the behaviour especially in damaged condition. Crack propagation sensing techniques using embedded fibre optics are described in Chap. 4 and these offer a tool for optimising structural bondlines, and the remote monitoring of known damages (active damage tolerance).

In Chap. 5 the potential for blade design tailored to twist upon deflection and thus enjoy a passive load reduction capacity is explored; and the analysis and design of such blades that can safely exploit this effect at regions along their length whilst maintaining required structural stiffness is proposed. In Chap. 6 the development of flow control devices is described as designers seek to optimise performance for the rotor and researchers deepen the understanding of complex flow control cases. And in Chap. 7 the modelling of active flaps on the leading and trailing edges of the blades is described suggesting that a localised effect on the load distribution can

be effected in-service, possibly eliminating adverse effects caused by tower shadow without generating any additional pitching moment.

Each area of research contains innovative aspects involving new approaches that improve on existing blade design procedures in a sustaining manner. Improving the sensor implementation via more robust and price competitive systems, better analysis tools, a deeper understanding of material and structural behaviour and degradation processes, ameliorating flow control devices, and providing assessment of designs for passive and active load alleviation.

These are all advances that are welcomed by an industry working to reduce Cost of Energy for offshore wind farms in the short term. However the greatest advance possible comes from a disruptive implementation of the new technology in a fully realised concept for structural sustainment. This essentially establishes a new relationship between the owner and their assets. This concept involves using permanent on-board health monitoring systems within a holistic management/control approach. It is a complex and multi-disciplinary field that has not been (and in fact cannot be) addressed by advancements in research alone.

Its realisation faces numerous training and research challenges; the main training challenge is the lack of young research scientists and engineers possessing the skills, research experience, and multi-disciplinary background required for undertaking the demanding research tasks of integrating, supporting and maintaining the innovative holistic structural health management systems and to propel their application in wind energy and other industries. The main research challenge is to focus and coordinate research in the previously mentioned fields to address technical voids which hinder the integration of the envisioned holistic approach. Training networks like MARE-WINT are successful in overcoming such challenges.

References

Bak C, Zahle F, Bitsche R et al (2013) The DTU 10-MW Reference Wind Turbine. In: DTU Orbit – The Research Information System. Available via Technical University of Denmark. http://orbit.dtu.dk/files/55645274/The_DTU_10MW_Reference_Turbine_Christian_Bak.pdf. Accessed 06 Apr 2016

Braga DFO, Tavares SMO, da Silva LFM et al (2014) Advanced design for lightweight structures: review and prospects. Prog Aerosp Sci 69:29–39. doi:10.1016/j.paerosci.2014.03.003

Brøndsted P, Nijssen R (eds) (2013) Advances in wind turbine blade design and materials, 1st edn. Woodhead Publishing, Cambridge

EWEA (2014) EWEA 2014, Recharge news, Day 3. Available via http://www.ewea.org/annual2014/wp-content/uploads/RechargeDaily03.pdf. Accessed 06 Apr 2016

EWEA (2016) European Wind Energy Association. http://www.ewea.org/. Accessed 06 Apr 2016

McGugan M, Pereira GF, Sørensen BF, Toftegaard HL, Branner K (2015) Damage tolerance and structural monitoring for wind turbine blades. Phil Trans R Soc A. doi:10.1098/rsta.2014.0077

UN (2016) United Nations Department of Economic and Social Affairs. https://sustainabledevelopment.un.org/topics/energy. Accessed 06 Apr 2016

Chapter 3
Damage Sensing in Blades

Borja Hernandez Crespo

Abstract This chapter is divided into three parts; the problem, possible solutions and the chosen option to address the problem, which is my PhD topic within the project MAREWINT. So firstly, the chapter presents an overview of the typical damages that a wind turbine blade can suffer during its life operation. Then, a review of different Structural Health Monitoring (SHM) techniques which are currently being investigated for wind turbine blades is presented. Finally, the chapter provides the state-of-the-art of Guided Wave Technology in composite materials; where different aspects of this SHM technique are explained in more detail.

3.1 Introduction

Wind energy is an important renewable energy source which has gained high relevance during the last decades. Different countries have released plans to invest in wind energy in the future years; such as the USA that will generate 20 % of the country's electricity from wind power by 2030 or Denmark that have set the targets of producing 50 % of the power from the wind by 2020 and also of making Denmark completely free of dependence on fossil fuels by 2050. So, the use of wind power is not expected to decrease within the next decade (Márquez et al. 2012). The trend is to manufacture bigger wind turbines and deploy them offshore. These new wind turbines have around 6 MW power output, 120-metre height tower and 80-metre long blades. They are designed to be operating in rough conditions in difficult-to-reach areas. Therefore, the deployment of Structural Health Monitoring (SHM) techniques becomes essential in order to assess remotely the integrity of the structure. The advantages of using these techniques are many (Schulz and Sundaresan 2006), such as reducing expensive costs for periodic inspections of turbines which are hard to reach, prevention of unnecessary replacement of components based on time of use, or minimizing down time and frequency of sudden breakdowns.

B. Hernandez Crespo (✉)
TWI Limited, Granta Park, Great Abington, Cambridge CB21 6AL, UK,
e-mail: borja.hernandez@twi.co.uk

W. Ostachowicz et al. (eds.), *MARE-WINT*, DOI 10.1007/978-3-319-39095-6_3

3.2 Structural Damages in Wind Turbine Blades

Wind turbine blades are composed by composite materials, mainly glass fibre, carbon fibre, balsa wood or foam, in order to improve efficiency by increasing the strength-weight ratio. The structure can be represented as a rectangular beam formed by the upper and lower spar caps and by two vertical shear webs, providing bending stiffness and torsional rigidity in order to withstand all the loads applied on the blade. The aerodynamic shape is given by two shells joint to the spars at both sides. Highly-toughness adhesive is used to bond both shells to each other at the leading and trailing edges, and also to join the shear webs to the spar caps. The outside of the blade is covered by a gel coat to be protected from ultraviolet degradation and water penetration. Typically in offshore wind turbine blades, the spar caps are formed by a thick laminate of glass fibre or glass/carbon hybrids, while the shells and the shear webs are sandwich panels composed by glass fibre skins and a thick foam or balsa wood core.

All those structures are susceptible to be damaged since they are continuously in operation under cycle loads in harsh environments. Structural damages, such as debonding or delamination, can be potentially generated in a number of ways.

- Leading Edge Erosion: It is a damage produced by abrasive airborne particles which impact and erode the leading edge, especially affects the region close to the tip where the velocity is higher. This erosion modifies the aerodynamic shape of the blade reducing the aerodynamic efficiency and hence, the power production. It also creates delaminations along the leading edge (Sareen et al. 2014).
- Lightning: The blades are the most vulnerable parts of the wind turbine to be impacted by a lightning. Currently, all blades have in place a lightning protection system to reduce as much as possible the damages generated by the impact, since otherwise the blade could be destroyed. Although it is common to have damages and cracks around the point of lightning attraction (Cotton et al. 2001).
- Icing: It is the accumulation of ice on the surface of the blade due to the combination of particular climate conditions and low temperature climate (Cattin 2012). Several problems can be caused by icing, such as the complete stop of the wind turbine due to highly severe icing, the disruption of aerodynamics with a reduction in energy generation or the increased fatigue due to imbalance loads caused by the ice mass resulting in a shortening of the structure lifetime (Homola 2005).
- Fatigue loads: Wind turbines are designed to be in continuous operation an average of 20 years. During this time, blades are permanently withstanding cycle loads which could lead in the creation of incipient damages due to fatigue mechanisms and then consequently their propagation till the collapse of the entire structure.

The different types of damages that a wind turbine blade can suffer during operation are reviewed in (Debel 2004) as follows. In Fig. 3.1, they are represented for further clarifications.

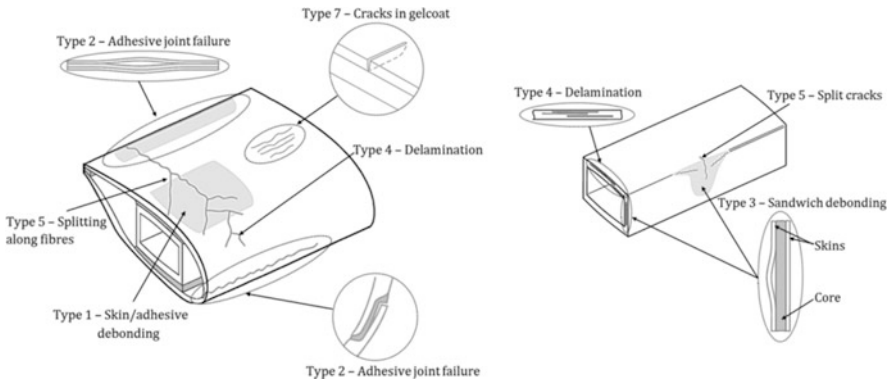

Fig. 3.1 Sketch of the different types of damage that can occur in a wind turbine blade (Sørensen et al. 2004)

- Type 1: Damage formation and growth in the adhesive layer joining skin and main spar flanges (skin/adhesive debonding and/or main spar/adhesive layer debonding)
- Type 2: Damage formation and growth in the adhesive layer joining the up- and downwind skins along leading and/or trailing edges (adhesive joint failure between skins)
- Type 3: Damage formation and growth at the interface between face and core in sandwich panels in skins and main spar web (sandwich panel face/core debonding)
- Type 4: Internal damage formation and growth in laminates in skin and/or main spar flanges, under a tensile or compression load (delamination driven by a tensional or a buckling load)
- Type 5: Splitting and fracture of separate fibres in laminates of the skin and main spar (fibre failure in tension; laminate failure in compression)
- Type 6: Buckling of the skin due to damage formation and growth in the bond between skin and main spar under compressive load (skin/adhesive debonding induced by buckling, a specific type 1 case)
- Type 7: Formation and growth of cracks in the gel-coat; debonding of the gel-coat from the skin (gel-coat cracking and gel-coat/skin debonding).

Ciang et al. (2008) also presented the most likely locations of the blade where damages can appear, which are at 30–35 % and 70 % of the blade length from the root, the root of the blade, the maximum chord area, and the upper spar cap/flange of the spar.

3.3 SHM on Wind Turbine Blades

The value of the blades is around the 15–20 % of the total costs of the wind turbine (Li et al. 2015a, b), thus the blades are critical parts that need to be monitored in order to ensure the cost-efficiency of the entire structure and its integrity. Currently, the blade assessment is based on costly periodic manned inspections. The techniques used are visual inspections and manual tapping tests, which require highly experienced experts. These techniques are not able to detect internal damages at early stages, so different NDT and SHM techniques have come out to fill this gap. In the following, current SHM techniques applied to wind turbine blades are presented.

3.3.1 Modal Analysis

This technique is based on the analysis of the dynamic response of the wind turbine blade during operation. The modal parameters extracted from the structure, such as frequencies and modal shapes, are directly related to the physical properties of the blade, such as mass and stiffness. Therefore, the analysis of modal parameters will detect variations in the physical properties, such as stiffness reduction caused by incipient damages or mass increasing caused by icing. In order to apply this technique, it is required to induce an excitation over the structure. Ideally for a SHM application, it would be preferred to use an ambient energy during the normal operation of the wind turbine, such as the blade vibrations caused by the wind turbulence which has been proved that excites a wide range of blade modes (Yang et al. 2014; Requeson et al. 2015). Other excitation sources used in this analysis are external shakers or embedded actuators which usually provide better results since a well-distributed excitation is created over the entire structure and also a flat spectrum is generated in the desired frequency range. To monitor the modal responses accelerometers, piezoelectric transducers and strain gauges are used.

Damage identification method is commonly based on the comparison between an undamaged and a damaged state. Simple analyses using the eigenfrequencies are valid for controlled laboratory tests, but under more realistic conditions these methods are unable to detect damages, since the modal property variations caused by them are the same order as the ones created by the environmental effects and noise contamination (Salawu 1997). Therefore, sophisticated and robust methods, such as continuous wavelet transformation, have to be used along with modal analysis in order to be deployed as a SHM application (Ulriksen et al. 2014).

Figure 3.2 depicts a modal measurement setup. The advantages of Modal Analysis are that it is a mature technology widely used for gearbox and bearing faults, feasible, well-proven and low cost. The disadvantages are small sensitivity (detection of relatively big damages), so there is a necessity to have a fine measurement density (more sensors) and the impossibility to install sensors close

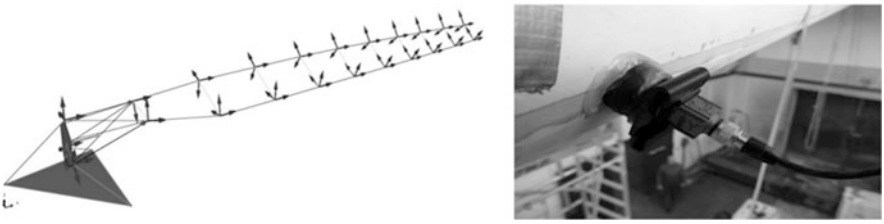

Fig. 3.2 Modal measurement system setup for SSP 34 m blade: (**a**) accelerometer location and orientation; and (**b**) utilized accelerometers (Brüel & Kjær Type 4524-B) mounted on a swivel base (Brüel & Kjær UA-1473) (Ulriksen et al. 2014)

to the tip due to the small section since they should be placed inside the blade for SHM applications.

3.3.2 Fibre Optics

Optical fibres are cylindrical dielectric waveguides designed to propagate the light along its length. The core of the fibre has a refractive index slightly higher than the core cladding, so when the light confined in the core reaches the cladding/core interface with an angle greater than the critical angle (Snell's law); the light is reflected back to the core enabling its propagation along the fibre (Ostachowicz and Güemes 2013). The light may leaks out when the optical fibre is bent with sharp radius; decreasing the optical power transmitted. This principle is used as a damage detection technique, called microbending fibre, where two solid corrugated parts bend the fibre, so relative displacement between both parts will cause sharper or flatter bends (decreasing or increasing the transmitted optical power) enabling the local monitoring of the structure. Optical fibres can be used to measure different type of properties, such as strain, temperature, loads or vibrations.

In wind energy applications, they have been mainly used as strain sensors. Two different measurement techniques have been utilized to monitor the strain in wind turbine blades, Fibre Bragg Gratings (FBGs) and distributed sensing. FBGs are local sensors with high sensitivity and reliability, allowing the possibility to multiplex several FBG sensors in a single optical fibre. In recent years, most of the investigations about fibre optic applications have been related to FBGs due to the variety of advantages that they offer (Choi et al. 2012; Glavind et al. 2013; Kim et al. 2013, 2014). FBGs are periodic variations in the refractive index of the core of the optical fibre. These refractive index variations are equally spaced a distance, Λ_0, and they behave like multiple mirrors which reflect a very narrow wavelength window, λ_B, of the light spectrum transmitted along the fibre, following this equation, Eq. (3.1):

$$\lambda_B = 2\overline{n_e}\Lambda_0 \tag{3.1}$$

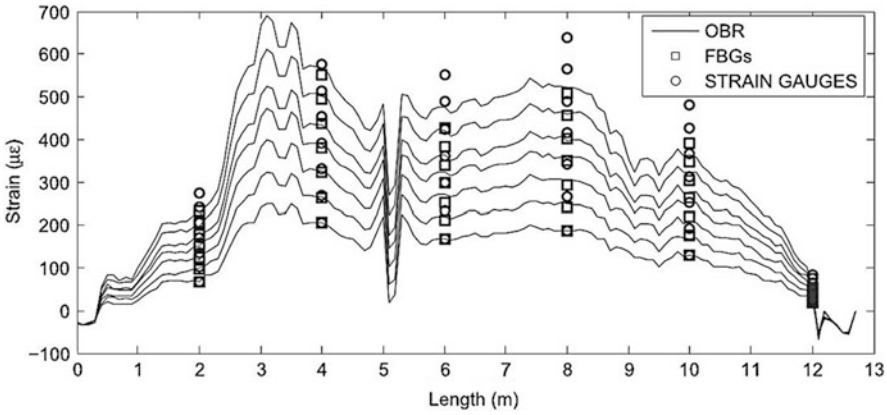

Fig. 3.3 Example of strain profiles for seven load magnitudes along the blade length gathered with the OBR (distributed sensing), the FBGs and the strain gauges. Sensors located at intrados, trailing edge. Results for a Wind Turbine Blade test in flapwise configuration, pressure side to suction side (PTS) (Sierra-Pérez et al. 2016)

where $\overline{n_e}$ is the average refractive index. Therefore, when the FBG is attached to a structure and it is strained or affected by changing temperature, the distance between the periodic variations changes, so the reflected wavelength shifts linearly enabling the monitoring of the local strain or temperature. In (Sierra-Pérez et al. 2016), a comparison between strain gauges and FBGs is studied for wind turbine applications, see Fig. 3.3. Both present similar detection capabilities and sensitivities, but FBGs offer comparative advantages, such as electromagnetic immunity, possibility to be embedded into composites or longest life. So, thinking in a future SHM application for wind turbine blades, FBGs would be more suitable than strain gauges. The other measurement method is the distributed sensing, where the entire length of the fibre works as a sensor. Several sensing methods have been used to provide distributed sensing; being the most used the Optical Frequency Domain Reflectometry (OFDR) based on the Rayleigh scatter. This Rayleigh backscattering component is caused by changes in density or composition along the fibre, so by controlling the slope of the decaying intensity curve, it is possible to identify breaks and heterogeneities along the fibre (Sundaresan et al. 2001). This technique can be used to measure the strain and the temperature with high resolution (better than 1 $\mu\varepsilon$ and 0.1 °C) (Sierra-Pérez et al. 2016), and also with a high spatial resolution along the fibre, in the order of millimetres. Strain measurements in wind turbine blades have been performed in recent investigations (Pedrazzani et al. 2012; Niezrecki et al. 2014; Sierra-Pérez et al. 2016) with good results, but this technique is almost limited to static tests because the acquired light power is too low, so several test repetitions are needed to increase the Signal to Noise Ratio (SNR).

The advantages of Fibre Optics are its high sensitivity, small size (may be embedded in composites), low weight, immunity to electromagnetic interferences

and electrical noise, fatigue resistance and wide operation temperature range. The disadvantages are its fragility, highly costly equipment and bulky equipment.

3.3.3 Guided Wave Technology

Guided waves (GW) are ultrasonic elastic waves that propagate in finite solid media. The technique is based on the analysis of guided waves which have propagated along the structure. Piezoelectric transducers are attached on the structure and excited by a signal generator with a predefined input signal, usually an n-cycle sinusoidal pulse with a Hanning window centred at a specific frequency. The transducers convert the electrical input into mechanical strain which enables the generation of the wave into the structure. The waves propagate along the structure passing through/interacting with defects, such as delamination, debonding, cracks or thickness reduction due to corrosion. This interaction makes the wave change during its propagation enabling the identification of damage. The waves can be acquired by the same transducer, in a Pulse-Echo configuration, where the damage is detected by the echoes reflected backwards when the wave passes through the defect; or acquired by another transducer, in a Pitch-Catch configuration where the damage is detected due to changes in amplitude, phase or time of flight (TOF) of the acquired wave modes. The great advantage is that GW technology inspects wide areas from a small number of points, in contrast to the others techniques which are locally, like conventional ultrasonic testing, see Fig. 3.4.

Commercially, GW technology has been successfully applied for inspection of pipelines in the oil & gas industry (Mudge and Harrison 2001). This inspection is able to scan tens of metres from one position and detect wall thickness variations caused by corrosion. In wind turbines where the structure is composed by different materials, such as glass fibre, carbon fibre or balsa; the complexity of the wave propagation increases hindering the application of GW. In recent years, there have

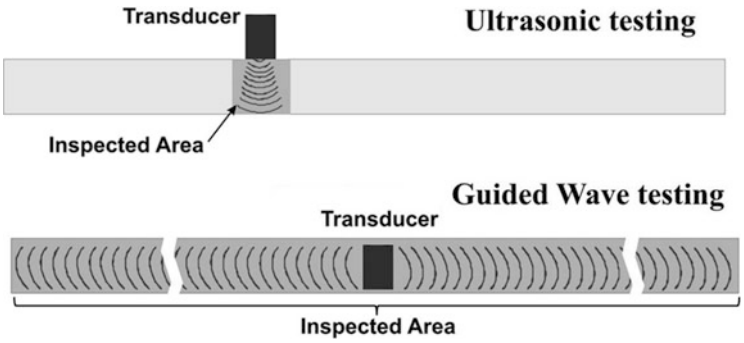

Fig. 3.4 Comparison of the inspected area between ultrasonic testing and GW testing

been many investigations studying the utilization of GW technology on wind turbine blades for damage detection (Claytor et al. 2010; Taylor et al. 2012, 2013a, b; Zak et al. 2012; Song et al. 2013; Li et al. 2015a, b). It has been demonstrated that GW are capable to detect composite damages (Su et al. 2002; Hay et al. 2003; Discalea et al. 2007; Sohn et al. 2011), such as delamination, debonding or fibre cracking; and also to locate the damages analysing the TOF of the wave modes. One issue for GW application in blades is the wave attenuation, since the amplitude of the wave decreases rapidly during its propagation in this type of materials allowing the inspection within a limited area. Investigations about ice detection and ice removal in wind turbine blades have been also carried using GW technology (Habibi et al. 2015; Shoja Chaeikar et al. 2015). The use of GW for composite materials is still in development, but it is seen as a promising technique for the future.

Another important improvement that is needed for the implementation of this technology in wind energy is the reliability. Wind turbine operators are usually reticent to install extra equipment in their turbines after investing a great deal of money. Therefore, more robust and reliable systems (transducers and equipment) are required in order to deploy this technology in wind turbine blades. Investigations in self-diagnosis of transducers during operation have been carried out by Taylor et al. (2013c), where they proposed a technique to analyse the impedance of the transducer in order to distinguish between structural damage and transducer malfunction, avoiding false positives in damage detection.

Figure 3.5 depicts a signal that can be acquired through the application of Guided Wave Technology in an aluminium plate. The advantages of Guided Wave Technology are that it is able to detect external and internal damages at early stages, it is capable to inspect large areas from a few locations, it is cost-effective and the transducers are small. The disadvantages are its improvable reliability and its bulky equipment.

3.3.4 Acoustic Emission

Acoustic Emission (AE) technique is based on the acquisition of transient elastic waves generated from a rapid release of energy caused by a damage or deformation (Pao et al. 1979). This wave generation can be produced by various phenomena such as cracks, rubbing, deformation, leakage, etc. The most detectable AE signals take place when plastic deformation is caused in the material or when it is loaded near its yield stress (NDT 2016). These phenomena create elastic waves which propagate in the material. The AE sensors, usually made of piezoelectric material, convert the strain caused by the elastic waves into electrical energy enabling the processing and signal analysis.

AE waves are comprised in a broad frequency range between 100 kHz and 1 MHz (Li and He 2012); conversely the waves in a lower frequency range are called vibration. The most common signal processing technique is to extract

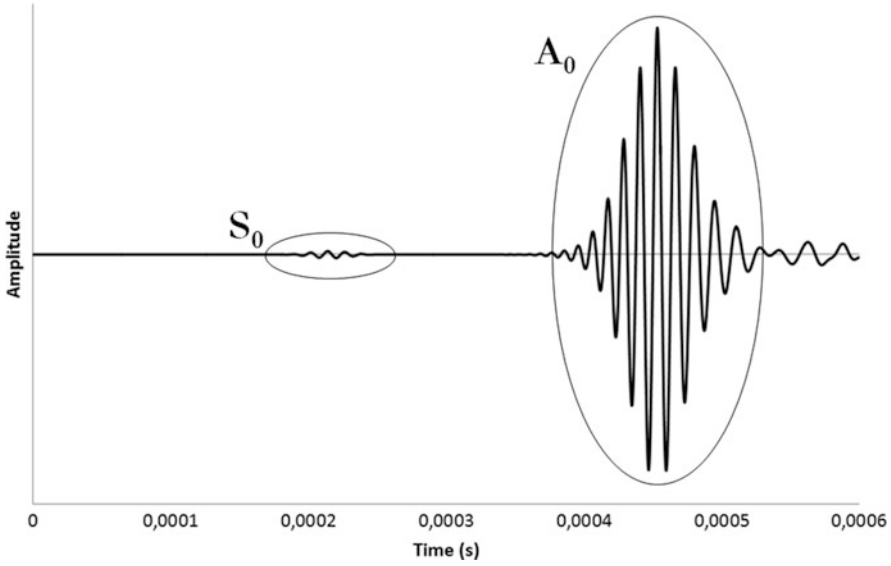

Fig. 3.5 Example of a signal acquired in a "pitch-catch" configuration in an aluminium plate. The two fundamental wave modes are highlighted, symmetric S_0 and antisymmetric A_0 modes

features from the time-domain signal due to its simplicity. However, more advanced signal processing techniques, such as wavelet transform, pattern recognition or classification methods, are needed in order to assess in a better manner the integrity of the structure (Chacon et al. 2015). This technique has been used in rotating machines and metallic structures, such as tanks or bridges with good results (Rauscher 2004; Nair and Cai 2010; Chacon et al. 2014). In wind turbine blades, AE has been applied in different investigations where it has been able to detect typical composite damages such as delamination or debonding (Han et al. 2014; Zhou et al. 2015). However, due to the high frequency content of the AE signals, attenuation is a major obstacle for this technique, especially in composite materials. Consequently, early stage damages where the amplitude signal is low will not be detectable, unless the sensors are placed close to the damage. Other disadvantages are that it is expensive and it generates large datasets due to the high sampling rate. Figure 3.6 shows an example of an acoustic emission signal.

3.3.5 Thermography

Thermal imaging technique is based on the measurement of the heat on the surface of the inspected structure in order to detect internal defects by observing temperature differences. The basic idea is that the thermal diffusivity will change if irregularities

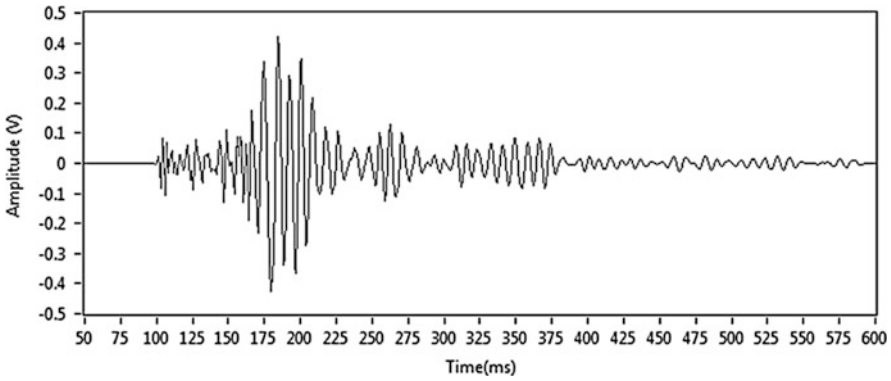

Fig. 3.6 Example of an AE signal

are present in the material, so temperature differences will be observable externally. There are two approaches to apply this technique, passive and active. The passive method is utilized when the materials to inspect have different temperature in comparison to the ambient temperature. And the active method is when external excitation, such as heat lamps, is used to apply thermal energy into the specimen making more clearly the temperature differences.

Two big concerns with this technique are the limitation of amount of thermal energy applied on the surface of the structure, and the difficulty to apply thermal energy over large surfaces in a uniform manner (Manohar 2012). The former is caused by the application of too much energy to the surface in order to generate sufficient contrast to detect deeper defects which may cause permanent damages. The latter is due to non-uniform heating (unwilling temperature differences) which could cause erroneous results and the reduction of the accuracy of the technique. This limitation makes quite difficult its applicability in wind turbine blades during operation. Further investigations are needed to overcome this problem and gain sensitivity to spatial and temporal variations (Manohar 2012).

The advantages of Thermography are that it is a non-contact technique, no baseline is needed and it has a full-field defect imaging capability enabling a rapid structural evaluation. The disadvantages are that it is very difficult to be applied in-service and the equipment is highly costly.

3.4 Guided Wave Technology in Composites

Guided wave (GW) technology is a growing Non Destructive Testing (NDT) technique in order to inspect and monitor the health of structures. The advantages of this technique are the capacity to scan an area of several metres from few locations and to make the inspection to structures in-service. This allows the system

potentially capable to be permanently installed on the structure enabling it to be monitored continuously. Guided Wave technology has been widely applied in metallic structures in order to inspect pipes, plates, rails (Alleyne and Cawley 1992a; Alleyne and Cawley 1992b; Cawley et al. 2003; Hayashi et al. 2003; Rose et al. 2004). During the 1990s, significant research was focused on pipe inspection (Ditri and Rose 1992; Alleyne et al. 1998; Lowe et al. 1998), because there was a need to assess in a rapid manner the integrity of hundreds of kilometres of pipelines in the oil & gas, nuclear and chemical industries. As a result of these investigations, guided wave commercial devices were released to service these industries (Mudge and Harrison 2001) which are able to inspect tens of metres from one position and detect wall thickness variations caused by corrosion.

In addition to metallic structure inspection, composite inspection using guided waves has been investigated in the recent years (Cawley 1994; Monkhouse et al. 1997; Su et al. 2002; Han et al. 2006; Lissenden and Rose 2008; Giurgiutiu and Santoni-Bottai 2011; Castaings et al. 2012; Rose 2012; Torkamani et al. 2014; Baid et al. 2015; Rekatsinas et al. 2015; Zhong et al. 2015). Much interest has arisen in this topic due to the increasing implementation of composite materials in the aerospace and wind energy industries and the necessity to inspect and monitor large composite structures, such as wings or wind turbine blades, in a cost-effective and rapid way. Moreover, composite materials, especially carbon fibre-epoxy due to its high Young's modulus and high strength to low weight ratio, are commonly used as structural parts like the spar in wings and blades. It is essential the inspection of those members to assure the integrity of the entire structure. Composite materials can be easily damaged when impacted, presenting damages such as delamination or matrix cracking which are difficult to detect in a visual based inspection. Currently, conventional ultrasonic inspection is widely used as the preferred NDT technique for composite structures (Kapadia 2012). This technique is able to detect the most common composite damages (delamination, debonding, porosity), but dependence on manual inspection of parts with difficult accessibility and the slowness of the inspection are obstacles, as well as the interruption of the operation of the entire structure means that an automatic inspection is also desirable. Guided wave technology provides an alternative solution for an in-service assessment of the integrity of the structure which can be deployed automatically. Damage detectability in composites using guided waves has been proved in many scientific publications (Hayashi and Kawashima 2002; Su et al. 2002; Hay et al. 2003; Paget et al. 2003; Sohn et al. 2004; Su and Ye 2004; Park et al. 2005; Discalea et al. 2007; Su et al. 2007; Diamanti and Soutis 2010; Gao et al. 2010; Ramadas et al. 2011; Sohn et al. 2011; Yeum et al. 2012; Torkamani et al. 2014). The anisotropic nature of composites due to the different ply-orientations produces a directional dependence of the wave propagation properties in terms of velocity and wave directionality (Rose 2012) which increases the difficulty of the data analysis. Also the complex designs of in-service composite structures, such as wind turbine blades, which are composed of different materials, e.g. carbon fibre, glass fibre, balsa or honeycomb hinder the implementation of this technique commercially, since it is difficult to

extract relevant information from the complex signals. So, many investigations and great progress are being carried out to overcome these issues.

3.4.1 Fundamentals of Guided Waves

Guided waves are elastic waves that propagate in solid plates. The main characteristics of this kind of waves are that the phase velocity and group velocity are not necessarily the same and they can vary according to the frequency, which is called dispersion. Depending on the boundary conditions of the medium where the wave is propagating through, different guided wave modes can be obtained (Rose 2014). In the case of thin plate-like structure (Fig. 3.7) with free upper and lower surfaces, Lamb waves will propagate within both surfaces, established as boundaries, guiding the propagation of the waves. The governing equation of guided wave motion is Navier's equation, Eq. (3.2) (Rose 2014):

$$\mu \cdot \frac{\partial^2 u_i}{\partial {x_j}^2} + (\lambda + \mu) \cdot \frac{\partial^2 u_j}{\partial x_j \partial x_i} + \rho \cdot f_i = \rho \cdot \frac{\partial^2 u_i}{\partial t^2} \qquad (i, j = 1, 2, 3) \qquad (3.2)$$

where u_i is the displacement in the x_i direction, f_i is the body force which is assumed to be zero, ρ is the density and λ and μ are the Lamé constants. By using the method of potentials, this second order partial differential equation can be decomposed into two uncoupled parts through Helmholtz decomposition, details in (Rose 2014).

Finally, Eq's. (3.3a) and (3.3b) are obtained that, together with the displacement equations, it is possible to calculate the motion of the guided waves in an isotropic and homogeneous plate-like structure (Rose 2014):

$$\frac{\tan(qh)}{\tan(ph)} = -\frac{4k^2qp}{(k^2 - q^2)^2} \qquad \text{for symmetric modes} \qquad (3.3a)$$

$$\frac{\tan(qh)}{\tan(ph)} = -\frac{(k^2 - q^2)^2}{4k^2qp} \qquad \text{for antisymmetric modes} \qquad (3.3b)$$

Fig. 3.7 Coordinates for thin plate-like structure

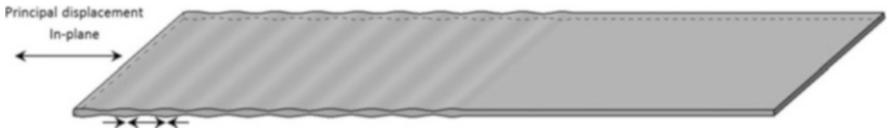

Fig. 3.8 Symmetric mode of propagation

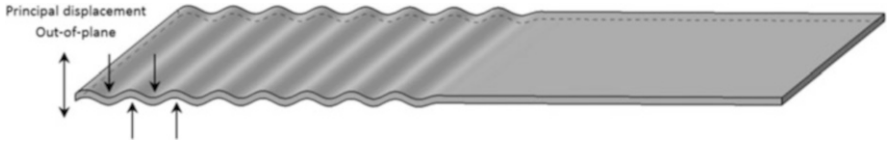

Fig. 3.9 Antisymmetric mode of propagation

Fig. 3.10 Shear mode of propagation

As it is shown in Eq's. (3.3a) and (3.3b), the solution of guided wave propagation presents a symmetric (S_i) and an antisymmetric (A_i) solution, consequently there will exist in the same plate two different modes of propagation one symmetric and one antisymmetric with respect to the middle plane along the thickness. Both wave motions are represented in Figs. 3.8 and 3.9 respectively.

Another wave motion related to guided waves is the shear horizontal (SH) wave mode where the particles displace transversally to the propagation direction, see Fig. 3.10. This mode presents advantages in comparison to S_i and A_i in terms of dispersion and attenuation, since the fundamental shear mode is non-dispersive so has less energy attenuation during its propagation (Rose 2014). Because of the non-dispersive nature of shear mode, the wave energy in the direction of propagation does not spread during its propagation, so the energy remains concentrated in the transmitting pulse enabling the wave to achieve longer distances. Also, the in-plane particle displacement of SH wave mode reduces the interaction with the surrounding media (Petcher et al. 2014). So, the wave energy transmitted remains inside the host material minimizing the energy leakage. These advantages are particularly important when a structure which is subsea, buried or with heavy coatings has to be inspected, or when longer distances are needed to reach in order to inspect areas where the accessibility is limited or prohibitive.

Regarding the attenuation, it may be divided in absorption, scattering and leakage (Wilcox et al. 2001). The first attenuation mechanism is due to the material damping of the host material which converts the wave energy into heat. The second one is produced when part of the wave energy is transmitted or reflected in other directions

than the original one. This scattering is mainly produced by defects or irregularities in the way of the wave which reflect part of the wave energy in other directions. This mechanism enables the identification of damages by guided wave technology inspection. And the third one is produced by the energy leakage which is the wave energy transmitted to the surrounding media. This energy transmission depends on the acoustic impedance compatibility between the surrounding material and the host material, the smaller the acoustic impedance mismatch the larger the energy is transmitted to the surrounding media. This energy leakage is commonly negligible for air, but it becomes more influential when coatings, paints or high damping materials are applied on the surface, or even more when the structure is subsea or buried, where the energy loss is highly significant (Wilcox et al. 2001).

3.4.1.1 Phase Velocity and Group Velocity

Generally, the velocity of guided waves can be described by the phase velocity and the group velocity. These two velocities measure different features of the wave, where phase velocity is the velocity related to the frequency, f, and wavelength, λ, $v_p = \lambda \cdot f$, which is the speed at which any fixed phase of the cycle is displaced. And group velocity is defined as the speed with which the information or energy of the wave propagates through the media. In other words, the speed at which the whole wave packet propagates.

The propagation velocity of the guided waves, in most of the cases, is frequency-dependent. It is different at different frequencies, so consequently frequency components of the same wave packet will travel at different velocities distorting the original input signal along its propagation. This phenomenon is called dispersion, which will be explained further on. A graphic example is shown in Fig. 3.11.

A consequence of this dispersion is that phase velocity is different to group velocity. In terms of angular frequency, $\omega = 2\pi f$, and wavenumber, $k = 2\pi/\lambda$, phase velocity and group velocity can be expressed as Eq's. (3.4a) and (3.4b):

$$v_p = \frac{\omega}{k} \tag{3.4a}$$

$$v_g = \frac{d\omega}{dk} \tag{3.4b}$$

3.4.1.2 Dispersion Curves

The relationship between velocity and frequency can be plotted in graphs called "dispersion curves", where the variation of different wave mode velocities is shown along the frequency. In Fig. 3.12, dispersion curves of phase velocity and group velocity are represented against the frequency for symmetric and antisymmetric modes of a 3-mm thick aluminium plate.

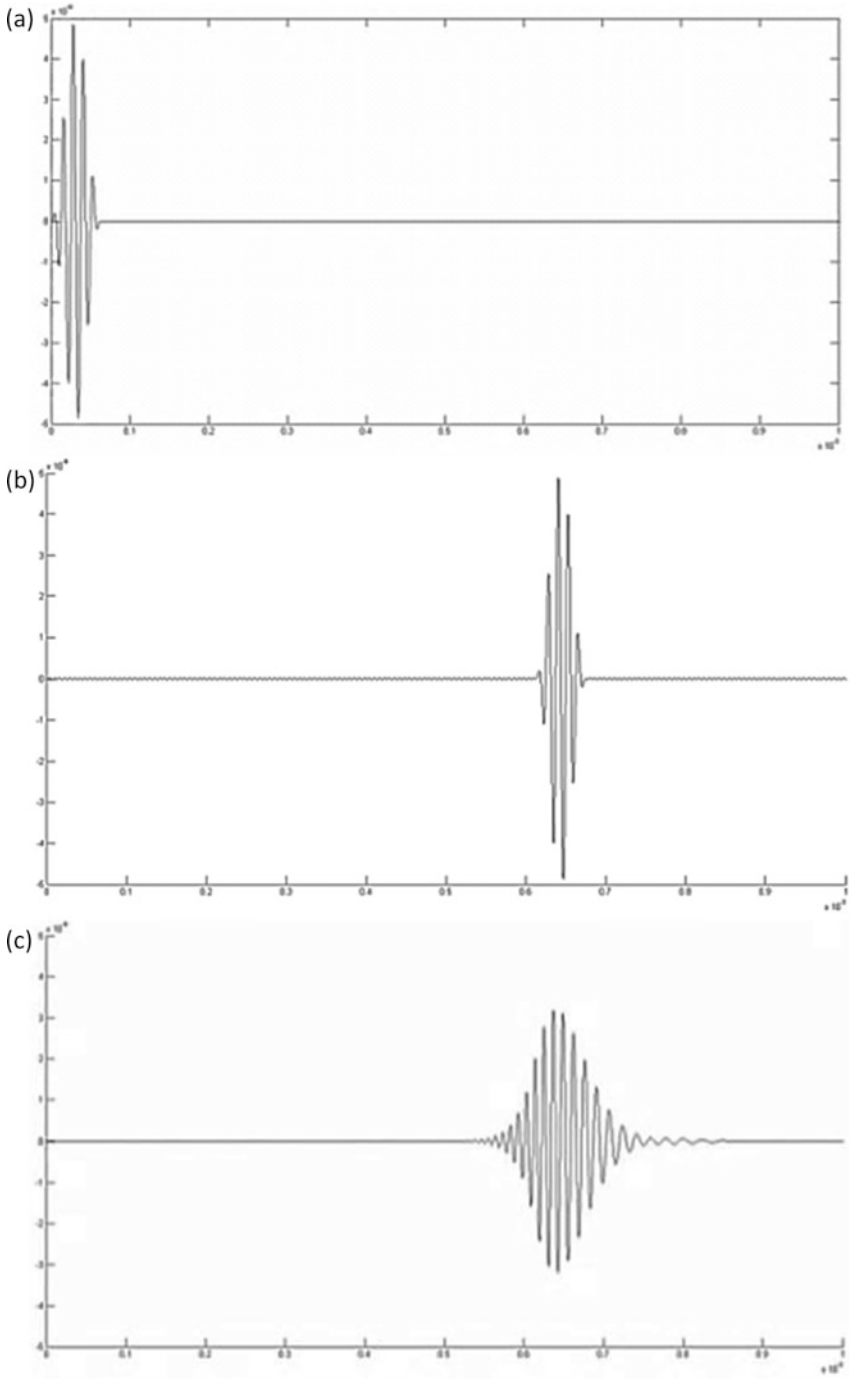

Fig. 3.11 Example of dispersion. (**a**) Input signal. (**b**) Non-dispersive wave. (**c**) Dispersive wave

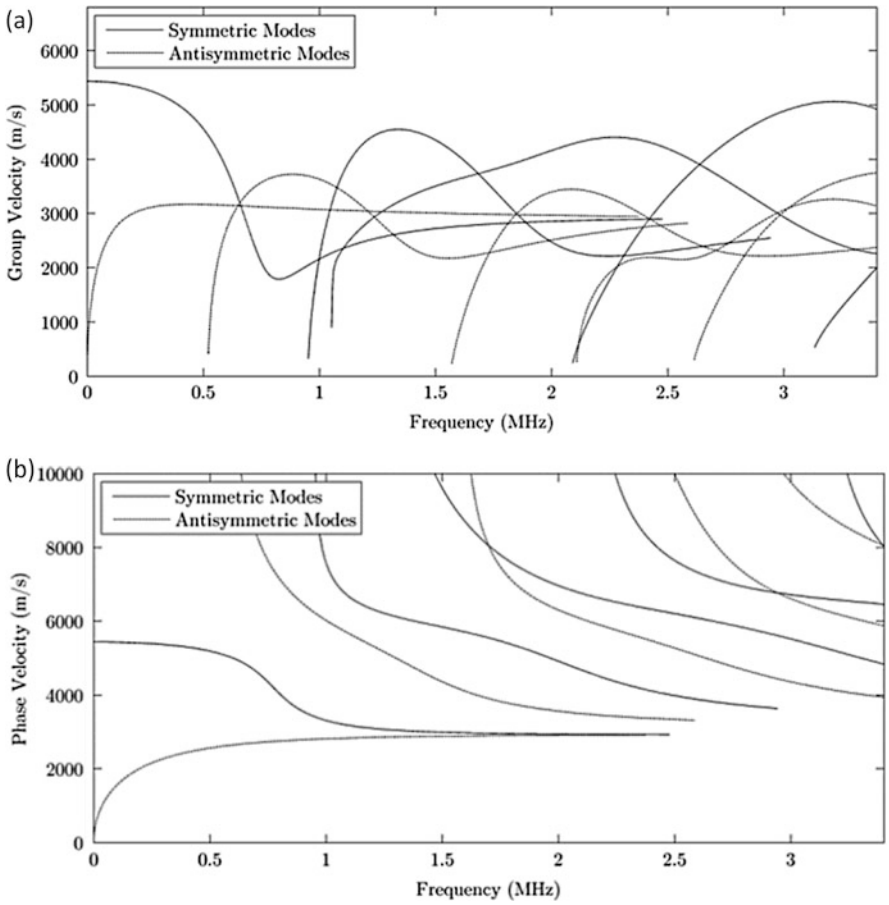

Fig. 3.12 Dispersion Curves of a 3-mm thick aluminium plate. (**a**) Phase velocity against frequency. (**b**) Group velocity against frequency. Extracted from Disperse Software (Pavlakovic et al. 1997)

The dispersion equations of Lamb waves for plate-like isotropic structures are (Rose 2014):

$$\frac{\tan(qh)}{q} + \frac{4k^2 p \tan(ph)}{(k^2 - q^2)^2} = 0 \qquad \text{for symmetric modes} \tag{3.5a}$$

$$q\tan(qh) + \frac{(k^2 - q^2)^2 \tan(ph)}{4k^2 p} = 0 \qquad \text{for antisymmetric modes} \tag{3.5b}$$

$$p^2 = \frac{\omega^2}{c_L^2} - k^2, \quad q^2 = \frac{\omega^2}{c_T^2} - k^2 \qquad \text{and} \qquad k = \frac{2\pi}{\lambda_{wave}} \tag{3.5c}$$

where h is the plate half thickness, k is the wavenumber, c_L is the longitudinal velocity, c_T is the transverse velocity, ω is the wave angular frequency and λ_{wave} is the wavelength. At each frequency, the wavenumber is modified in order to find the roots of the Eq's. (3.5a) and (3.5b) (Su and Ye 2009). The dispersion curves can be plotted by joining the roots of the different wave modes. These curves are highly important to guided wave damage detection in order to predict the time of arrival, to excite desired modes, to design phased arrays and generally to deploy any guided wave application.

Due to the utilization of finite number of cycles in a pulse to interrogate the structure in guided wave inspection, this technique is especially affected by dispersion. This is because short pulses contain broadband frequency ranges centred at the transmitting frequency, so more different frequency components are involved in the travelling wave packet distorting the acquired signal to a higher extent, instead of using a narrowband input signal. Consequently, when guided waves propagate long distances, very distorted and attenuated signals are acquired for dispersive wave modes. Many of the investigations related to dispersion compensation are based on time reversal, in which the excitation signal is modified in order to concentrate the wave packet energy at a certain distance. Wilcox (2003) also proposed dispersion compensation based on a signal processing methodology, in which the dispersion effect is removed by replacing the time domain signal into a distance domain signal. Very accurate data of the dispersion curves of the studied wave modes is required, as the proposed methodology is very sensitive to small variations.

3.4.2 Guided Waves in Composites

Composites are characterised by their multi-layered structure, in contrast to metallic materials which are a continuous media with no interfaces. Composites are commonly used in aerospace or wind energy industry, such as carbon fibre/epoxy or glass fibre/epoxy laminates, and constituted by a number of layers orientated at different directions. These layers are formed by fibres and resins. The high anisotropy of the fibres confers to the laminate anisotropic nature, which depends on the stacking sequence of the plies (Nadella et al. 2010). Therefore, a laminate can be highly anisotropic if all the fibres are oriented in the same direction or it can be weakly anisotropic if the fibres are equally oriented in all directions. This anisotropy makes the wave velocity dependent to the angle of propagation, so this angular dependency will be more significant for highly anisotropic composites, unlike the weakly anisotropic laminates which will have a velocity profile similar to the one of an isotropic material (Karmazin et al. 2011).

Another important consequence of the wave propagation in composites is the absence of pure modes of propagation. In isotropic materials Lamb waves have displacements in x and z directions and the shear horizontal only in y direction but in anisotropic materials guided waves have displacements in the

three directions (Rose 2012). For example, symmetric modes S_i have displacements in the propagating direction (x axis) and in the out-of-plane direction (z axis) but in composites small displacements in the perpendicular direction (y axis) will be induced as well. Consequently, another way to designate these non-pure modes was established. The modes which have their main displacement component in the direction of the wave propagation are called quasi-symmetric qS_i, the modes which have the main displacement component in the out-of-plane direction are called quasi-antisymmetric qA_i, and the modes with the main displacement component perpendicular to the wave propagation and parallel to the surface are called quasi-shear horizontal qSH_i (Karmazin et al. 2013). Hereafter called symmetric S_i, antisymmetric A_i and shear horizontal SH_i modes for simplicity reasons. The attenuation is another factor to have in mind for guided wave propagation in composites, since it gets significant at higher frequencies, due to the viscoelastic behaviour of the resin which damps the wave energy and also because of the scattering caused by the fibres (Wang and Yuan 2007).

For the dispersion curves creation, it is necessary to make a distinction between isotropic or anisotropic materials. Since for isotropic materials the wave velocity depends only on the magnitude of the wave vector $k = |k|$, which is the wavenumber. But for anisotropic materials, it is required to consider the magnitude and also the direction of the wave vector. This distinction expands the previous definition of the phase velocity for anisotropic materials in order to involve in the equation the direction of the wave vector, which can be expressed as Eq. (3.6) (Wang and Yuan 2007):

$$\mathbf{c_p} = \left(\frac{\omega}{k}\right)\left(\frac{\mathbf{k}}{|\mathbf{k}|}\right) = \left(\frac{\omega}{k^2}\right)\mathbf{k} \tag{3.6}$$

where ω is the angular frequency and $\mathbf{k}$ the wave vector. A new concept that was not indicated before for isotropic materials is the slowness. Mathematically, it is defined as the inverse velocity and it is given by Eq. (3.7):

$$\mathbf{s} = \frac{\mathbf{k}}{\omega} \tag{3.7}$$

Note that the wave vector direction is always normal to the wave front of constant phase, so the phase velocity and the slowness always have the same direction as the wave vector. In order to calculate the group velocity, the wave vector direction has to be taken into consideration as well. So from the group velocity Eq. (3.4b) presented before, the group velocity can be defined as Eq. (3.8) (Wang and Yuan 2007; Karmazin et al. 2013):

$$\mathbf{c_g} = \frac{d\omega\,(k,\ \theta)}{d\mathbf{k}} = \nabla\omega\,(k,\ \theta) = \frac{\partial\omega}{\partial k}\mathbf{e_k} + \frac{1}{k}\frac{\partial\omega}{\partial\theta}\mathbf{e_\theta} \tag{3.8}$$

where $\mathbf{e_k}$ is the unit vector in the radial direction and $\mathbf{e_\theta}$ is the unit vector in the angular direction. The group velocity in Cartesian coordinates can be calculated

using a transformation matrix, Eq. (3.9):

$$\begin{Bmatrix} c_{gx} \\ c_{gy} \end{Bmatrix} = \begin{bmatrix} \cos\theta & -\sin\theta \\ \sin\theta & \cos\theta \end{bmatrix} \begin{Bmatrix} \frac{\partial\omega}{\partial k} \\ \frac{1}{k}\frac{\partial\omega}{\partial\theta} \end{Bmatrix} \tag{3.9}$$

So the magnitude of the group velocity is given by Eq. (3.10):

$$c_g = \sqrt{c_{gx}^2 + c_{gy}^2} \tag{3.10}$$

And the angle of the group velocity direction is given by Eq. (3.11):

$$\theta_g = \tan^{-1}\frac{c_{gy}}{c_{gx}} \tag{3.11}$$

The difference between the wave vector angle and the group velocity angle is known as the skew angle, $\varphi_{skew} = \theta - \theta_g$. A different way to calculate the skew angle from the complex Poynting vector is described in (Rose 2012). The equation of the Poynting vector is Eq. (3.12):

$$\mathbf{P} = -\frac{\tilde{\mathbf{v}} \cdot \boldsymbol{\sigma}_{\mathbf{M}}}{2} \tag{3.12}$$

where $\tilde{\mathbf{v}}$ is the conjugate of particle velocity vector and $\boldsymbol{\sigma}_{\mathbf{M}}$ is the stress tensor as shown in Eq. (3.13):

$$\boldsymbol{\sigma}_{\mathbf{M}} = \begin{bmatrix} \sigma_{kk} & \sigma_{k\theta} & \sigma_{kz} \\ \sigma_{\theta k} & \sigma_{\theta\theta} & \sigma_{\theta z} \\ \sigma_{zk} & \sigma_{z\theta} & \sigma_{zz} \end{bmatrix} \tag{3.13}$$

The integral of the Poynting vector across the thickness in a specific direction yields the power flow density in this chosen direction. Therefore in the case of plane waves, it is possible to determine the skew angle with Eq. (3.12) by calculating the power flow density in the wave vector direction P_k, and in the perpendicular direction (angular direction) P_θ. For anisotropic materials, P_θ is nonzero for certain wave modes. Hence, this component introduces a wave skew effect, which can be calculated by Eq. (3.14):

$$\varphi_{skew} = \tan^{-1}\left(\frac{\int P_\theta dz}{\int P_k dz}\right) \tag{3.14}$$

This is not the case for isotropic materials, where the component P_θ will be equal to zero as there is no angular dependency of the velocities. So the skew angle will be zero and the wave vector and group velocity will have the same direction.

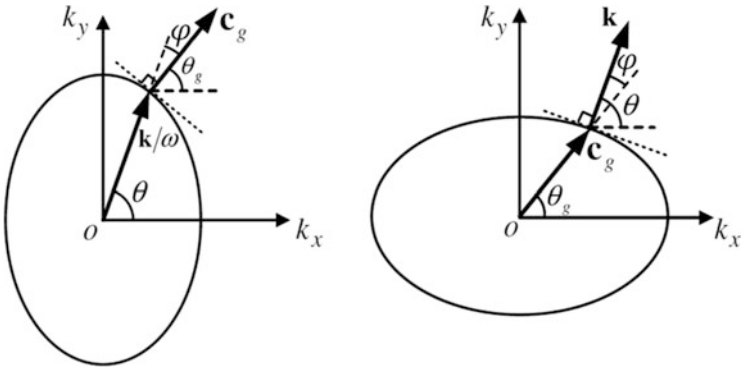

Fig. 3.13 Relationship between wave vector and group velocity vector. (**a**) Slowness curve. (**b**) Group velocity wave front (Wang and Yuan 2007)

Geometrically, the wave vector can be related to the group velocity, see Fig. 3.13. The normal direction of group velocity wave front is the direction of the wave vector; vice versa, the normal direction of the slowness curve is the group velocity direction. Figure 3.13 also depicts the skew angle φ, in which the different directions of the group, θ_g, and phase velocities, θ, are clearly shown.

3.4.2.1 Simulation

The simulation of guided waves is an essential step for the understanding of the wave propagation in multi-layered structures and is also useful for validating new damage detection techniques or new transducer arrays. The wide range of different layups makes the experimental analysis of each one individually impracticable; therefore the simulation is used to investigate different materials or layups in an efficient manner. In guided wave analysis of composites, the hypothesis of considering each layer isotropic across the thickness is commonly adopted; each ply is a homogeneous orthotropic layer. This assumption is based on the fact that the wavelengths of the propagating guided waves are substantially longer than the characteristic size of the cross section of the fibres (Tauchert and Guzelsu 1972; Wang and Yuan 2007). In Tauchert and Guzelsu (1972), it is shown that the scattering produced by the fibres of each layer occurs when the wavelength is of the same order of the diameter of the fibres for longitudinal modes, and 40 times the order of the diameter for flexural modes.

The dispersion properties of composite materials and the analysis of the 3D propagation of guided waves are being commonly studied by numerical or analytical methods. Different techniques have been proposed, such as traditional Finite Element Method (FEM) (Lissenden et al. 2009; Song et al. 2009; Ricci et al. 2014), semianalytical finite element method (SAFE) (Hayashi et al. 2003; Deng and Yang 2011; Rose 2014), finite differences (Saenger and Bohlen 2004; Moczo et al.

2007) or applying the elasticity theory using the global matrix and transfer matrix (Wang and Yuan 2007; Karmazin et al. 2011, 2013). Finite Element Methods have limitations due to the available computational resources, since for high frequencies a very fine discretization, both temporal and spatial, is necessary to comply with the Nyquist theorem and to ensure a minimum number of elements per wavelength in order to replicate the wave. This problem is overcome with the use of SAFE, where the waveguide is only discretized in a cross section of the structure, reducing considerably the computational load. In the literature the analytical methods have been established as a good approach for the analysis of guided waves in composites, but they are more susceptible to miss roots of the dispersion equations and distort the results.

The wave mode displacements depending on the angle of propagation and the stacking sequence of the composite have been described in many publications (Rhee et al. 2007; Wang and Yuan 2007; Karmazin et al. 2011, 2013). For instance, it has been shown that the propagation in unidirectional laminates has a preferential direction along the fibre direction. In the case of cross-ply laminates 0°/90°, the simulations show that there are two preferential directions 0° and 90° and it is also noticeable that for the angles in between the wave propagation is at 45° direction, see Fig. 3.14. For quasi-isotropic laminates, the wave front profile is very similar to the isotropic materials; the wave velocity has very small variations with the angle. In Karmazin et al. (2013), the authors analysed the wave propagation in a cross ply laminate using the analytical method of Green's matrix in a frequency-wavenumber domain. In this work, they concluded that the symmetric mode depends strongly on the wave propagation direction in high anisotropic laminates, in contrast to the antisymmetric modes which weakly depend on the propagation angle, as can be

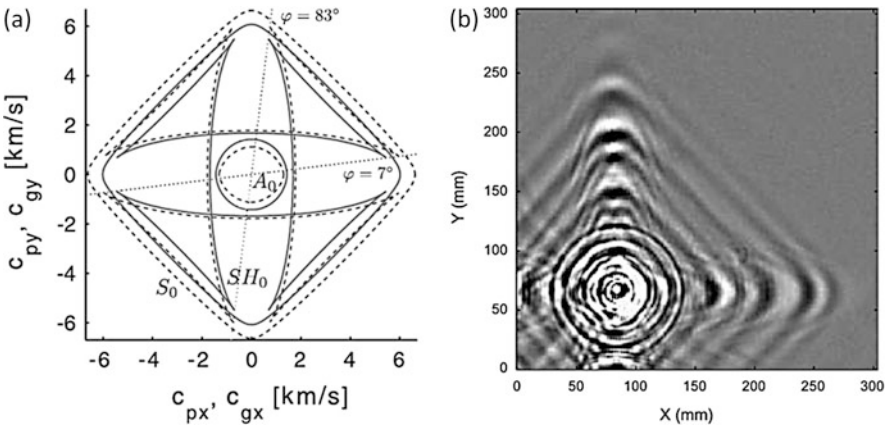

Fig. 3.14 Representation of the group velocity wave front in a cross-ply laminate by two different methods. (**a**) An analytical method using the Fourier Transform of Green's matrix. *Solid line* (Karmazin et al. 2013). (**b**) An experimental technique using scanning air-coupled ultrasonic transducers (SAUT) (Michaels et al. 2011)

seen in Fig. 3.14. Another important observation in Fig. 3.14 is the shape of the wave front in the shear horizontal mode, which is caused when the curvature of the slowness shifts from convex to concave shape. This effect is well-known in the analysis of bulk waves in anisotropic solids (Wang and Yuan 2007). It is called the phenomenon of energy focusing. Note that near the angles of 7° and 83°, there is a concentration of energy.

In the example shown in Fig. 3.14a, the shear horizontal mode presents several group velocity values—particularly, it presents one, two or three different group velocities for the same direction. Therefore, in these particular multi-valued directions usually called caustics (Karmazin et al. 2013), three pulses of the same wave mode will propagate at different velocities.

3.4.2.2 Damage Detection

In composite materials, the most common damage is the delamination between plies caused by impacts or cyclic loads. This mode of failure consists in the separation of layers which leads to significant loss of strength. Typically, the flaws created inside the laminate by impacts are not visible to the naked eye, therefore guided wave inspection in composite is highly recommended since the wave modes propagate along the structure sweeping the entire thickness. Internal damages will interact with the propagating wave modes, inducing changes in its propagation pattern. The wave modes will be affected by the delamination in different ways depending on its mode of vibration. In the literature (Grondel et al. 2002; Su et al. 2007; Hu et al. 2008; Ramadas et al. 2009; Rekatsinas et al. 2015), the three fundamental wave modes S_0, A_0 and SH_0 are the most studied and the most commonly used in order to interrogate a structure. The symmetric mode is chosen at low frequencies, below 200 kHz, because they are less dispersive so the shape of the pulse does not spread along the propagation direction which eases the post-analysis and reduce the complexity of the acquired signals. In addition, the symmetric mode has less attenuation since its displacement is an in-plane motion and the carried energy remains inside the structure avoiding scattering. The S_0 mode also has more sensitivity to delaminations than the A_0 mode (Wang and Yuan 2007). Nevertheless, the A_0 mode has more resolution in order to detect smaller flaws, since the wavelength of the A_0 mode is shorter than the others and the size defect detectability is commonly established at the same order of the wavelength of the propagating mode. The passing through of wave modes across a delamination produces a split in energy creating a new mode of propagation. This wave mechanism is called mode conversion and it also occurs when the wave reaches the edge of a plate, so new wave modes are created and reflected backwards. Mode conversion in delaminations has been studied in several investigations in order to take advantage of these changes and use them to detect and locate these defects (Su et al. 2007; Hu et al. 2008; Ramadas et al. 2009). Hu et al. (2008) analysed numerically the propagation of the S_0 mode through a delamination. When the S_0 mode enters in the delamination, a small amount of the energy of S_0 (almost undetectable) is reflected backwards and most of

it is transmitted forward, but also mode conversion is produced, so a new A_0 mode is reflected and a new A_0 mode is transmitted. The same mechanism occurs when the wave mode moves out of the delamination, the S_0 and a new A_0 are transmitted forward and a reflected S_0 and a new A_0 are transmitted backwards. In this case the reflected S_0 mode has a greater amount of energy which enables the detection of the delamination in a pulse-echo configuration. So, in the publication, they are able to locate the end of the delamination calculating the propagating distance with the dispersion curves but they cannot determine the extent of the delamination which is highly important. Other detection techniques are based on a pitch-catch configuration, where the acquired signal is usually compared to a baseline signal from an undamaged condition. These techniques analyse the incoming wave packets and study their phase, amplitude and time of arrival establishing a damage index in order to compare different damage states (Giurgiutiu and Santoni-Bottai 2011; Torkamani et al. 2014). The use of this technique on its own is quite limited since only the path between transmitter and receiver is inspected. Thus, a network of transducers covering the structure has been performed by many researchers (Zhao et al. 2007; Lissenden and Rose 2008; Ng and Veidt 2009) in order to interrogate in a pitch-catch configuration the entire structure. With this technique, the system is able to map the inspected area by analysing all the paths between transducers. The paths affected by damages are highlighted facilitating the visual localization of the damage. Another interesting technique is to apply a data processing algorithm to a wave field image acquired by a laser vibrometer system (Michaels et al. 2011; Sohn et al. 2011; Rogge and Leckey 2013). In (Michaels et al. 2011), the authors use a signal processing technique in order to remove specific wave modes from the images in order to reveal low amplitude reflections from damages masked by high amplitude wave modes. To do this, the images are transformed to a frequency-wavenumber plane using the 2D Fourier Transform. In this domain, the different propagating wave modes are easily recognisable, so by applying a filter it is possible to remove a specific wave mode, and subsequently perform the inverse Fourier Transform to get the images without this mode. The disadvantage of this technique is that is not applicable to in-service structures, since the equipment to get the images is very sensitive to external vibrations so the acquisition has to be performed in very controlled conditions. Wavelet Transform is another signal processing technique widely used in guided wave technology, mainly in a pitch-catch configuration (Kessler et al. 2002; Yan and Yam 2002; Paget et al. 2003). In composite materials, it has been proved that it provides good detectability results.

Another important damage in composites that has been studied in the literature is the debonding, which is the separation between the shell and the core in a sandwich structure or between two parts joined by adhesive or co-curing. This kind of damage is structurally of great importance, since the debonding of a stiffener from the shell in a wing or the shear web from the spar in a wind turbine blade can cause a great loss of stiffness and a possible collapse of the entire structure. Investigations of this type of damage with guided waves follow a similar approach to the delamination detection. Since most of the studies are based on a transducer network in order to map the bonding area and locate the debonding by analysing the paths between

transducers (Lissenden et al. 2009; Mustapha et al. 2012; Song et al. 2012; Ricci et al. 2014).

References

Alleyne DN, Cawley P (1992a) Optimization of Lamb wave inspection techniques. NDT&E Int 25:11–22

Alleyne DN, Cawley P (1992b) The interaction of Lamb waves with defects. IEEE Trans Ultrason Ferroelectr 39:381–397

Alleyne DN, Lowe M, Cawley P (1998) The reflection of guided waves from circumferential notches in pipes. J Appl Mech 65:635–641. doi:10.1115/1.2789105

Baid H, Schaal C, Samajder H et al (2015) Dispersion of Lamb waves in a honeycomb composite sandwich panel. Ultrasonics 56:409–416

Castaings M, Singh D, Viot P (2012) Sizing of impact damages in composite materials using ultrasonic guided waves. NDT&E Int 46:22–31

Cattin R (2012) Icing of wind turbines: Vindforsk projects, a survey of the development and research needs. In Reports. ELFORSK. Available via ELFORSK. http://elforsk.se/Rapporter/?download=report&rid=12_13_. Accessed 06 Apr 2016

Cawley P (1994) The rapid non-destructive inspection of large composite structures. Composites 25:351–357

Cawley P, Lowe M, Alleyne D et al (2003) Practical long range guided wave inspection applications to pipes and rail. Mater Eval 61:66–74

Ciang CC, Lee J-R, Bang H-J (2008) Structural health monitoring for a wind turbine system: a review of damage detection methods. Meas Sci Technol 19(12):2001

Claytor TN, Ammerman CN, Park G et al (2010) Structural damage identification in wind turbine blades using piezoelectric active sensing with ultrasonic validation. In Publications. Los Alamos National Laboratory. Available via LANL. http://permalink.lanl.gov/object/tr?what=info:lanl-repo/lareport/LA-UR-10-00416. Accessed 06 Apr 2016

Cotton I, Jenkins N, Pandiaraj K (2001) Lightning protection for wind turbine blades and bearings. Wind Energy 4:23–37

Chacon JLF, Andicoberry EA, Kappatos V et al (2014) Shaft angular misalignment detection using acoustic emission. Appl Acoust 85:12–22

Chacon JLF, Kappatos V, Balachandran W et al (2015) A novel approach for incipient defect detection in rolling bearings using acoustic emission technique. Appl Acoust 89:88–100

Choi K-S, Huh Y-H, Kwon I-B et al (2012) A tip deflection calculation method for a wind turbine blade using temperature compensated FBG sensors. Smart Mater Struct 21:025008

Debel C (2004) Identification of damage types in wind turbine blades tested to failure. In: Somers MAJ (ed) Materialeopførsel og skadesanalyse. DMS, Lyngby, pp 123–127

Deng Q, Yang Z (2011) Propagation of guided waves in bonded composite structures with tapered adhesive layer. Appl Math Model 35:5369–5381
Diamanti K, Soutis C (2010) Structural health monitoring techniques for aircraft composite structures. Prog Aerosp Sci 46:342–352
Discalea FL, Matt H, Bartoli I et al (2007) Health monitoring of UAV wing skin-to-spar joints using guided waves and macro fiber composite transducers. J Intell Mater Syst Struct 18:373–388
Ditri JJ, Rose JL (1992) Excitation of guided elastic wave modes in hollow cylinders by applied surface tractions. J Appl Phys 72:2589–2597
Gao H, Ali S, Lopez B (2010) Efficient detection of delamination in multilayered structures using ultrasonic guided wave EMATs. NDT&E Int 43:316–322
Giurgiutiu V, Santoni-Bottai G (2011) Structural health monitoring of composite structures with piezoelectric-wafer active sensors. AIAA J 49:565–581
Glavind L, Olesen IS, Skipper BF et al (2013) Fiber-optical grating sensors for wind turbine blades: a review. Opt Eng 52:030901
Grondel S, Paget C, Delebarre C et al (2002) Design of optimal configuration for generating A0 Lamb mode in a composite plate using piezoceramic transducers. J Acoust Soc Am 112:84–90
Habibi H, Cheng L, Zheng H et al (2015) A dual de-icing system for wind turbine blades combining high-power ultrasonic guided waves and low-frequency forced vibrations. Renew Energy 83:859–870
Han B-H, Yoon D-J, Huh Y-H et al (2014) Damage assessment of wind turbine blade under static loading test using acoustic emission. J Intell Mater Syst Struct 25:621–630
Han J, Kim C-G, Kim J-Y (2006) The propagation of Lamb waves in a laminated composite plate with a variable stepped thickness. Compos Struct 76:388–396
Hay TR, Wei L, Rose JL et al (2003) Rapid inspection of composite skin-honeycomb core structures with ultrasonic guided waves. J Compos Mater 37:929–939
Hayashi T, Kawashima K (2002) Multiple reflections of Lamb waves at a delamination. Ultrasonics 40:193–197
Hayashi T, Song W-J, Rose JL (2003) Guided wave dispersion curves for a bar with an arbitrary cross-section, a rod and rail example. Ultrasonics 41:175–183
Homola M (2005) Impacts and causes of icing on wind turbines. Available via Høgskolen i Narvik. http://ansatte.hin.no/mch/documents/Wind%20energy%20BSR-Impacts%20and%20causes%20of%20icing%20on%20wind%20turbines.pdf. Accessed 06 Apr 2016
Hu N, Shimomukai T, Yan C et al (2008) Identification of delamination position in cross-ply laminated composite beams using S0 Lamb mode. Compos Sci Technol 68:1548–1554
Kapadia A (2012) Best practice guide: non-destructive testing of composite materials. Composites UK. Available via National Composites Network. https://compositesuk.co.uk/system/files/documents/ndtofcomposites.pdf. Accessed 06 Apr 2016
Karmazin A, Kirillova E, Seemann W et al (2011) Investigation of Lamb elastic waves in anisotropic multilayered composites applying the Green's matrix. Ultrasonics 51:17–28
Karmazin A, Kirillova E, Seemann W et al (2013) A study of time harmonic guided Lamb waves and their caustics in composite plates. Ultrasonics 53:283–293
Kessler SS, Spearing SM, Atalla MJ et al (2002) Damage detection in composite materials using frequency response methods. Compos Part B Eng 33:87–95
Kim H-I, Han J-H, Bang H-J (2014) Real-time deformed shape estimation of a wind turbine blade using distributed fiber Bragg grating sensors. Wind Energy 17:1455–1467
Kim S-W, Kang W-R, Jeong M-S et al (2013) Deflection estimation of a wind turbine blade using FBG sensors embedded in the blade bonding line. Smart Mater Struct 22:125004
Li D, Ho S-CM, Song G et al (2015a) A review of damage detection methods for wind turbine blades. Smart Mater Struct 24:033001
Li R, He D (2012) Rotational machine health monitoring and fault detection using EMD-based acoustic emission feature quantification. IEEE Trans Instrum Meas 61:990–1001
Li X, Yang Z, Zhang H et al (2015b) Crack growth sparse pursuit for wind turbine blade. Smart Mater Struct 24:015002

Lissenden C, Puthillath P, Rose J (2009) Guided wave feature identification for monitoring structural damage in joints between composite laminates. Mater Forum 33:279–285
Lissenden CJ, Rose JL (2008) Structural health monitoring of composite laminates through ultrasonic guided wave beam forming. In: Abstracts of the RTO Applied Vehicle Technology Panel (AVT) symposium, NATO, Montreal, 13–16 Oct 2008
Lowe MJ, Alleyne DN, Cawley P (1998) Defect detection in pipes using guided waves. Ultrasonics 36:147–154
Manohar A (2012) Quantitative nondestructive testing using infrared thermography. Dissertation, University of California
Márquez FPG, Tobias AM, Pérez JMP et al (2012) Condition monitoring of wind turbines: techniques and methods. Renew Energy 46:169–178
Michaels TE, Michaels JE, Ruzzene M (2011) Frequency-wavenumber domain analysis of guided wavefields. Ultrasonics 51:452–466
Moczo P, Robertsson JO, Eisner L (2007) The finite-difference time-domain method for modeling of seismic wave propagation. Adv Geophys 48:421–516
Monkhouse R, Wilcox P, Cawley P (1997) Flexible interdigital PVDF transducers for the generation of Lamb waves in structures. Ultrasonics 35:489–498
Mudge P, Harrison J (2001) TELETEST guided wave technology-case histories. Paper presented at nondestructive testing. In: 1st Middle East conference and exhibition, Bahrain, 24–26 September 2001
Mustapha S, Ye L, Wang D et al (2012) Debonding detection in composite sandwich structures based on guided waves. AIAA J 50:1697–1706
Nadella KS, Salas KI, Cesnik CES (2010) Characterization of guided-wave propagation in composite plates. In Kundu T (ed) Proceedings of the SPIE 7650, health monitoring of structural and biological systems, California, 2010
Nair A, Cai C (2010) Acoustic emission monitoring of bridges: review and case studies. Eng Struct 32:1704–1714
NDT Resource Center (2016) Theory - AE sources. https://www.nde-ed.org/EducationResources/CommunityCollege/Other%20Methods/AE/AE_Theory-Sources.htm. Accessed 25 Jan 2016
Ng CT, Veidt M (2009) A Lamb-wave-based technique for damage detection in composite laminates. Smart Mater Struct 18:074006
Niezrecki C, Avitabile P, Chen J et al (2014) Inspection and monitoring of wind turbine blade-embedded wave defects during fatigue testing. Struct Health Monit 13(6):629–643
Ostachowicz W, Güemes A (eds) (2013) New trends in structural health monitoring. Springer, Berlin
Paget CA, Grondel S, Levin K et al (2003) Damage assessment in composites by Lamb waves and wavelet coefficients. Smart Mater Struct 12:393
Pao Y-H, Gajewski RR, Ceranoglu AN (1979) Acoustic emission and transient waves in an elastic plate. J Acoust Soc Am 65:96–105
Park G, Rutherford AC, Wait JR et al (2005) High-frequency response functions for composite plate monitoring with ultrasonic validation. AIAA J 43:2431–2437
Pavlakovic B, Lowe M, Alleyne D et al (1997) Disperse: a general purpose program for creating dispersion curves. In: Thompson DO, Chimenti DE (eds) Review of progress in quantitative nondestructive evaluation, vol 16. Springer, Heidelberg, p 185
Pedrazzani JR, Castellucci M, Sang AK et al (2012) Fiber optic distributed strain sensing used to investigate the strain fields in a wind turbine blade and in a test coupon with open holes. In: Proceedings of the SAMPE technical conference, Charleston, 22–24 Oct 2012
Petcher P, Burrows SE, Dixon S (2014) Shear horizontal (SH) ultrasound wave propagation around smooth corners. Ultrasonics 54:997–1004
Ramadas C, Balasubramaniam K, Joshi M et al (2009) Interaction of the primary anti-symmetric Lamb mode (Ao) with symmetric delaminations: numerical and experimental studies. Smart Mater Struct 18:085011
Ramadas C, Padiyar J, Balasubramaniam K et al (2011) Lamb wave based ultrasonic imaging of interface delamination in a composite T-joint. NDT&E Int 44:523–530

Rauscher F (2004) Defect detection by acoustic emission examination of metallic pressure vessels. J Acoust Em 22:49–58

Rekatsinas C, Nastos C, Theodosiou T et al (2015) A time-domain high-order spectral finite element for the simulation of symmetric and anti-symmetric guided waves in laminated composite strips. Wave Motion 53:1–19

Requeson OR, Tcherniak D, Larsen GC (2015) Comparative study of OMA applied to experimental and simulated data from an operating Vestas V27 wind turbine. In: Abstracts of the international operational modal analysis conference, Gijón, 12–14 May 2015

Rhee S-H, Lee J-K, Lee J-J (2007) The group velocity variation of lamb wave in fiber reinforced composite plate. Ultrasonics 47:55–63

Ricci F, Mal AK, Monaco E et al (2014) Guided waves in layered plate with delaminations. In: Abstracts of the EWSHM-7th European workshop on structural health monitoring, Nantes, 8–11 July 2014

Rogge MD, Leckey CA (2013) Characterization of impact damage in composite laminates using guided wavefield imaging and local wavenumber domain analysis. Ultrasonics 53:1217–1226

Rose JL (2012) Health monitoring of composite structures using guided waves. In: The Defense Technical Information Center. Available via DTIC. http://www.dtic.mil/cgi-bin/GetTRDoc?Location=U2&doc=GetTRDoc.pdf&AD=ADA563790 Accessed 06 Apr 2016

Rose JL (2014) Ultrasonic guided waves in solid media. Cambridge University Press, New York

Rose JL, Avioli MJ, Mudge P et al (2004) Guided wave inspection potential of defects in rail. NDT&E Int 37:153–161

Saenger EH, Bohlen T (2004) Finite-difference modeling of viscoelastic and anisotropic wave propagation using the rotated staggered grid. Geophysics 69:583–591

Salawu O (1997) Detection of structural damage through changes in frequency: a review. Eng Struct 19:718–723

Sareen A, Sapre CA, Selig MS (2014) Effects of leading edge erosion on wind turbine blade performance. Wind Energy 17:1531–1542

Schulz M, Sundaresan M (2006) Smart sensor system for structural condition monitoring of wind turbines. In: National Renewable Energy Laboratory Documents. Available via NREL. http://www.nrel.gov/docs/fy06osti/40089.pdf. Accessed 06 Apr 2016

Shoja Chaeikar S, Berbyuk V, Boström A (2015) Investigating the application of guided wave propagation for ice detection on composite materials. In: Boltež M, Slavič J, Wiercigroch M (eds) Proceedings of the international conference on engineering vibration, Ljubljana, 2015

Sierra-Pérez J, Torres-Arredondo MA, Güemes A (2016) Damage and nonlinearities detection in wind turbine blades based on strain field pattern recognition. FBGs, OBR and strain gauges comparison. Compos Struct 135:156–166

Sohn H, Dutta D, Yang J et al (2011) Delamination detection in composites through guided wave field image processing. Compos Sci Technol 71:1250–1256

Sohn H, Park G, Wait JR et al (2004) Wavelet-based active sensing for delamination detection in composite structures. Smart Mater Struct 13:153

Song F, Huang G, Hu G (2012) Online guided wave-based debonding detection in honeycomb sandwich structures. AIAA J 50:284–293

Song F, Huang G, Hudson K (2009) Guided wave propagation in honeycomb sandwich structures using a piezoelectric actuator/sensor system. Smart Mater Struct 18:125007

Song G, Li H, Gajic B et al (2013) Wind turbine blade health monitoring with piezoceramic-based wireless sensor network. Int J Smart Nano Mater 4:150–166

Sørensen BF, Jørgensen E, Debel CP et al (2004) Improved design of large wind turbine blade of fibre composites based on studies of scale effects (Phase 1). Summary report. In: DTU Orbit - The Research Information System Publications. Available via DTU Orbit. http://orbit.dtu.dk/fedora/objects/orbit:90493/datastreams/file_7702048/content. Accessed 06 Apr 2016

Su Z, Yang C, Pan N et al (2007) Assessment of delamination in composite beams using shear horizontal (SH) wave mode. Compos Sci Technol 67:244–251

Su Z, Ye L (2004) Lamb wave-based quantitative identification of delamination in CF/EP composite structures using artificial neural algorithm. Compos Struct 66:627–637

Su Z, Ye L (2009) Identification of damage using lamb waves: from fundamentals to applications. Springer, Heidelberg

Su Z, Ye L, Bu X (2002) A damage identification technique for CF/EP composite laminates using distributed piezoelectric transducers. Compos Struct 57:465–471

Sundaresan M, Pai P, Ghoshal A et al (2001) Methods of distributed sensing for health monitoring of composite material structures. Compos Part A Appl Sci Manuf 32:1357–1374

Tauchert TR, Guzelsu A (1972) An experimental study of dispersion of stress waves in a fiber-reinforced composite. J Appl Mech-T ASME 39:98–102. doi:10.1115/1.3422677

Taylor SG, Farinholt KM, Jeong H et al (2012) Wind turbine blade fatigue tests: lessons learned and application to SHM system development. In: The 6th European workshop on structural health monitoring – EWSHM. Available via NDT Net. http://www.ndt.net/article/ewshm2012/papers/we2b4.pdf. Accessed 06 Apr 2015

Taylor SG, Farinholt K, Choi M (2013a) Incipient crack detection in a composite wind turbine rotor blade. J Intell Mater Syst Struct 25(5):613–620. doi:10.1177/1045389X13510788

Taylor SG, Park G, Farinholt KM et al (2013b) Fatigue crack detection performance comparison in a composite wind turbine rotor blade. Struct Health Monit 12:252–262

Taylor SG, Park G, Farinholt KM et al (2013c) Diagnostics for piezoelectric transducers under cyclic loads deployed for structural health monitoring applications. Smart Mater Struct 22:025024

Torkamani S, Roy S, Barkey ME et al (2014) A novel damage index for damage identification using guided waves with application in laminated composites. Smart Mater Struct 23:095015

Ulriksen MD, Tcherniak D, Kirkegaard PH et al (2014) Operational modal analysis and wavelet transformation for damage identification in wind turbine blades. In: The 7th European workshop on structural health monitoring – EWSHM. Available via NDT Net. http://www.ndt.net/article/ewshm2014/papers/0210.pdf. Accessed 06 Apr 2016

Wang L, Yuan F (2007) Group velocity and characteristic wave curves of Lamb waves in composites: modeling and experiments. Compos Sci Technol 67:1370–1384

Wilcox P, Lowe M, Cawley P (2001) Mode and transducer selection for long range Lamb wave inspection. J Intell Mater Syst Struct 12:553–565

Wilcox PD (2003) A rapid signal processing technique to remove the effect of dispersion from guided wave signals. IEEE Trans Ultrason Ferroelectr 50:419–427

Yan Y, Yam L (2002) Online detection of crack damage in composite plates using embedded piezoelectric actuators/sensors and wavelet analysis. Compos Struct 58:29–38

Yang S, Tcherniak D, Allen MS (2014) Modal analysis of rotating wind turbine using multiblade coordinate transformation and harmonic power spectrum. In: De Clerck J (ed) Topics in modal analysis I: Proceedings of the 32nd IMAC, a conference and exposition on structural dynamics, Brescia, July 2012. Conference proceedings of the society for experimental mechanics series, vol 7. Springer, Heidelberg

Yeum CM, Sohn H, Ihn JB et al (2012) Instantaneous delamination detection in a composite plate using a dual piezoelectric transducer network. Compos Struct 94:3490–3499

Zak A, Krawczuk M, Ostachowicz W (2012) Spectral finite element method for propagation of guided elastic waves in wind turbine blades for SHM purposes. In: The 6th European workshop on structural health monitoring – EWSHM. Available via NDT Net. http://www.ndt.net/article/ewshm2012/papers/tu2d2.pdf. Accessed 06 Apr 2016

Zhao X, Gao H, Zhang G et al (2007) Active health monitoring of an aircraft wing with embedded piezoelectric sensor/actuator network: I. Defect detection, localization and growth monitoring. Smart Mater Struct 16(4):1208–1217

Zhong C, Croxford A, Wilcox P (2015) Remote inspection system for impact damage in large composite structure. P Roy Soc Lond A Mat. doi:10.1098/rspa.2014.0631

Zhou W, Li Y, Li Z et al (2015) Interlaminar shear properties and acoustic emission monitoring of the delaminated composites for wind turbine blades. In: Shen G, Wu Z, Zhang J (eds) Advances in acoustic emission technology, vol 158, Springer proceedings in physics. Springer, Heidelberg, pp 557–566

Chapter 4
Fibre Bragg Grating as a Multi-Stage Structure Health Monitoring Sensor

Gilmar Ferreira Pereira

Abstract There is a clear need to implement models and measurement systems through the entire life of the wind turbine blade. In this chapter will be presented some work conducted to implement optical fibres as a multi-stage sensor, capable to measure different structural properties, and link them with all the different life stages and support a better design of the wind turbine blades. The characteristics and functionality of fibre Bragg grating sensors are briefly introduced. Their application as multi-stage structure health monitoring sensors for polymer laminate composite is then described. At the manufacturing stage, where the sensors can measure several parameters of infusion and curing, sensor feedback can help control the process, avoid residual strain, and contribute to the product certification; and then in operation where cracks can be detected and monitored. Experimental mechanical testing involving crack growth and fibre Bragg sensing is described that highlights the response from the fibre optic which will correctly detect the presence and growth of damage. Models to implement these results in a damage detection system for a wind turbine blade can then be developed.

4.1 Fibre Bragg Grating Sensors

Fibre Bragg grating (FBG) sensors are the most commonly used type of sensors in the fibre optic field. An FBG sensor can be embedded in the Fibre reinforced polymer material (main material of the wind turbine blade), without compromising its structural resistance. This is due to the FBG reduced size, with a diameter of 125 μm it is virtual non-intrusive to the material. Also, FBG sensors present other interesting features, such high resolution, multiplexing capability, immunity to electro-magnetic fields, chemical inertness and long term stability.

A FBG is formed by a permanent periodic modulation of the refractive index along a section of an optical fibre, by exposing the optical fibre to an interference pattern of intense ultra-violet light. The photosensitivity of the silica exposed to the

G.F. Pereira (✉)
Department of Wind Energy, Technical University of Denmark (DTU), DTU Risø Campus, Frederiksborgvej 399, 4000 Roskilde, Denmark
e-mail: gilmar.fepe@gmail.com

W. Ostachowicz et al. (eds.), *MARE-WINT*, DOI 10.1007/978-3-319-39095-6_4

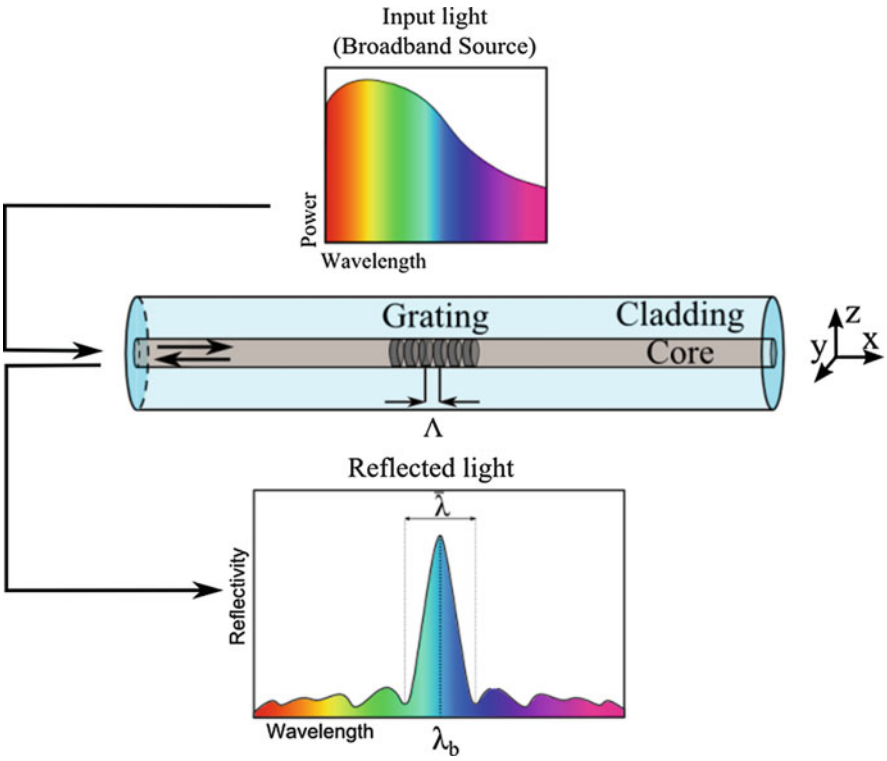

Fig. 4.1 Fibre Bragg grating: strongest mode coupling at the Bragg wavelength

ultra-violet light is increased, so that when light propagates through the periodically alternating regions of higher and lower refractive index within the fibre, it is reflected by successive, coherent scattering from the index variations. When the reflection from a crest in the index modulation is in phase with the next one, it is generated the maximum mode coupling or reflection. The strongest mode coupling occurs at the Bragg wavelength, λ_b, as shown in Fig. 4.1. The wavelength λ_b, is described by the Bragg condition:

$$\lambda_b = 2n_{eff}\Lambda \tag{4.1}$$

where n_{eff} is the mean effective refractive index at the location of the grating and Λ is the constant nominal period of the refractive index modulation (Hill and Meltz 1997).

The bandwidth $\overline{\lambda}$ (distance between the two first minima) is given by:

$$\frac{\overline{\lambda}}{\lambda_b} = \frac{1}{n_{eff}}\sqrt{\left(\zeta\overline{\delta n_{eff}}\right)^2 + \left(\frac{\lambda_b}{L}\right)^2} \tag{4.2}$$

where L is the gauge length, $\overline{\delta n_{eff}}$ is the mean induced change in n_{eff} and ζ is the amplitude of the induced index change (Peters et al. 2001). An external load or temperature variation will change the effective index of refraction and/or the period of modulation; this will create a shift of the wavelength reflected peak from its original value.

4.2 Manufacturing Stage: Residual Stress Induced by Resin Shrinkage and Curing Process Control

The FBG sensors are an excellent choice to monitor the curing process of wind turbine blades, where their capability of surveying the curing process is combined with their capability to monitor strain and other features over the structure lifetime. Because the FBG sensor small size that makes them virtually non-intrusive to the structure, they can be embedded in the composite layers from the first manufacturing step.

This embedded sensor will monitor several parameters of the curing process: temperature of the resin, which enables a retro-feedback of temperature to the process controller; residual stress that are a big issue in the fatigue performance of the composite; resin flow, by measuring the position of dry spots in the laminate; etc. Additionally, the FBG sensor can be used as part of the process certification, by giving information about the curing profile of the structure, the residual stress, the load history during manufacturing, transport and installation.

4.2.1 Embedded FBG Response to Strain and Temperature Variation

Assuming a perfect strain transfer between an embedded FBG sensor and the host material, the wavelength shift, $\Delta\lambda_b$, under variation of strain in the longitudinal direction of the fibre optic, ε_1, and temperature, ΔT, is given by Eq (4.3):

$$\frac{\Delta\lambda_b}{\lambda_b} = (1\text{-}p_e)\,\varepsilon_1 + [(1\text{-}p_e)\,(\alpha_s\text{-}\alpha_f) + \xi]\,\Delta T \tag{4.3}$$

The parameter p_e is the optical fibre photo-elastic coefficients, α_s and α_f are the thermal expansion coefficient of the host material and the optical fibre, respectively, and ξ is the thermos-optic coefficient (Magne et al. 1997). Figure 4.2 depicts a typical Fibre Bragg grating response.

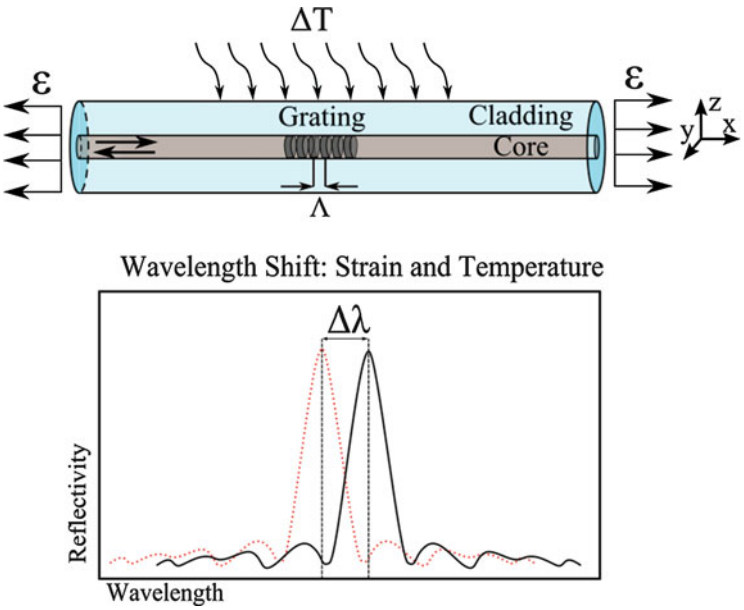

Fig. 4.2 Fibre Bragg grating response: strain and temperature variation

4.2.2 Residual Stress Measurement

Curing cycles are often defined on the basis of experience and economical aspects, missing the opportunity to improve curing cycles and blades, by understanding the physic-chemical process. Reducing the reaction time by increasing the temperature leads to a decrease in production time and consequent lower production cost. But this can lead to residual stress induced by the curing process, which causes worst mechanical properties and reduces the fatigue life of the structure. Equation (4.3) was rewritten to measure the residual stress caused by the material shrinkage:

$$\varepsilon_{shrinkage} = \frac{\frac{\Delta\lambda_b}{\lambda_b} - \xi\Delta T}{1 - p_e} + \alpha_f \Delta T \tag{4.4}$$

By measuring the temperature in the resin using a thermocouple, it is possible to decouple the temperature-strain cross sensitivity of the FGB and calculates the epoxy shrinkage.

4.3 Operation Stage: Crack Growth Detection by Embedded FBG Sensors

Often in fibre reinforced polymers (FRP), delamination is accompanied by the formation of a crack bridging zone, where intact fibres connect the crack faces behind the crack tip, as shown in Fig. 4.3. Thus, the energy required for the crack to propagate is higher than required to initiate. The relationships between the crack bridging stresses and the crack opening displacement (bridging laws) are used to describe the effect of fibres on the crack propagation (Sørensen 2010). The cracking in homogeneous isotropic materials usually occurs under pure Mode I (opening loading) but in weak planes or along interfaces, like in composite materials cracking, occurs under a combination of Modes (Shear and opening loading).

In order to detect delamination/crack in FRP materials the sensor/monitoring system need to track specific fracture features that only appear in the vicinities of the

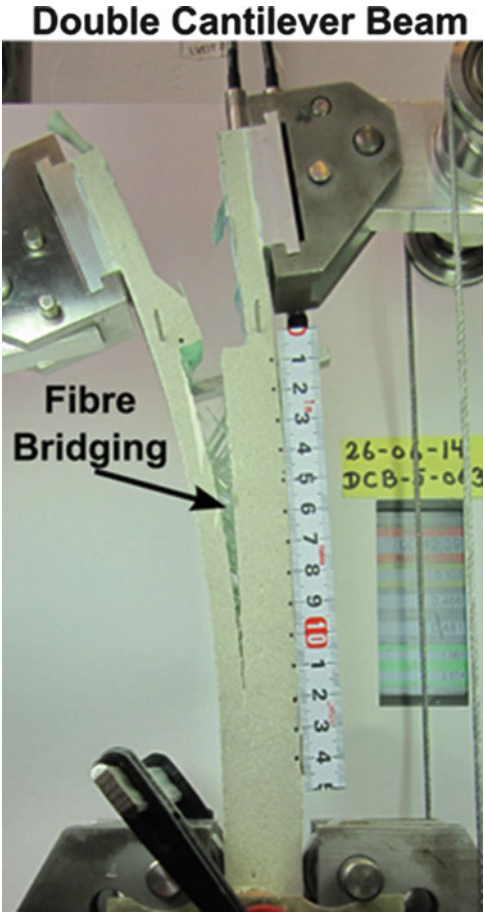

Fig. 4.3 Fibre bridging during delamination of a DCB specimen

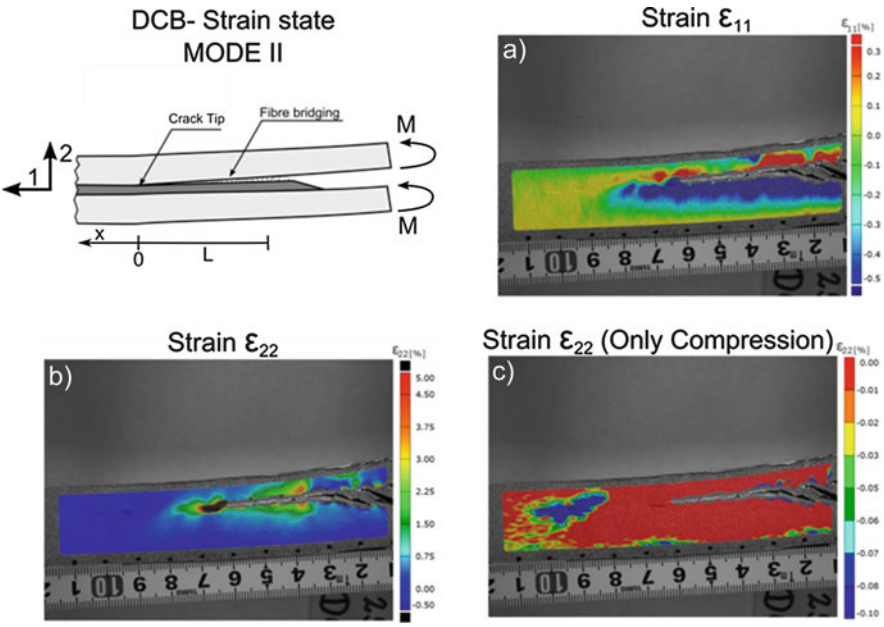

Fig. 4.4 Strain distribution at the crack tip during Mode II fracture (Pereira et al. 2015)

crack, independent of geometry and loading conditions. Thus, to link these fracture features with the measured parameters, the strain distribution around a crack tip during delamination was analysed using Digital Image Correlation (DIC), as shown in Fig. 4.4 (Pereira et al. 2015). The DIC technique is a non-contact optical method that, by tracking changes in a random pattern on the specimen, can correlate it with deformation/strain of the material.

It is possible to divide the strain distribution in two distinct contributions: crack tip singularity/material damage and fibre bridging. Near the crack tip, the stress field closely approaches the singular stress field of linear elastic fracture mechanics. This means that the stress tends to infinity and has a fast variation (high gradient). Also, with the progression of the crack the material/structure losses stiffness increasing the strain, here it is possible to observe higher values of strain ε_{11} at the crack faces, as showed in Fig. 4.4a. In the fibre bridging zone ($L < x < 0$), a positive strain ε_{22} was observed, due to the forces transferred by the fibre that are connecting the two crack faces, as shown in Fig. 4.4c. These forces are balanced by a compression stress that appears ahead of the crack tip ($x > 0$), which creates a negative strain ε_{22}, shown in Fig. 4.4c as a blue area.

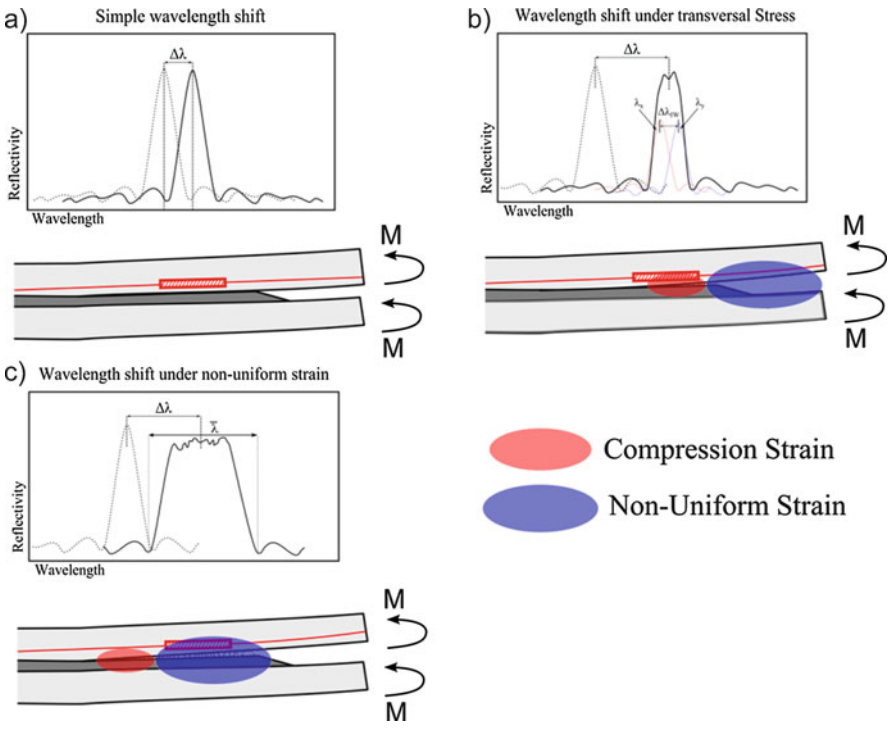

Fig. 4.5 Stages of the FBG response under a crack growth event

4.3.1 Crack/Delamination Detection by Embedded Fibre Bragg Gratings

As measured using DIC technique, during a crack/delamination event different fracture features will be present near the crack tip. Being able to identify and measure these specific phenomena with a FBG sensor is the key factor to correctly determine the presence of damage and its growth.

The three different stages of the FBG responses under a crack growth event are presented in Fig. 4.5. First, before the crack reaches the proximity of the grating (Fig. 4.5a), the material will build-up strain, that will create a uniform wavelength shift in the FBG reflected peak. Next, a compression field is formed ahead of the crack tip due to the formation of a crack bridging zone (Fig. 4.5b). When this compression field reaches the grating area it creates a peak splitting of the FGB response. Then, when the grating is near the influence of the crack singularity (Fig. 4.5c), a non-uniform strain field will also modify the shape of the reflected peak. After the crack passes the FBG sensor, the shape of the reflected peak will go back to the original shape, and the sensor response will again be a simple wavelength shift, because at this stage only uniform strains will be present at the FBG.

4.3.1.1 Embedded FBG Response: Strain

As mentioned before, the FBG response to strain and temperature variation can be described by Eq. (4.3). However, during crack growth the temperature variation can be neglected. The wavelength shift $\Delta\lambda_b$ (Fig. 4.5a) is given by (4.5):

$$\frac{\Delta\lambda_b}{\lambda_b} = (1\text{-}p_e)\,\varepsilon_1 \tag{4.5}$$

4.3.1.2 Embedded FBG Response: Transverse Stress

The compression field formed ahead of the crack tip will reach the grating area, which will create a peak split of the FBG reflected signal (Fig. 4.5b). This peak split phenomenon is due to a birefringent effect, which can be defined as the change of the refractive index n_{eff} in the two directions n_{effy} and n_{effz}, when the grating is subjected to a transverse force (Sørensen et al. 2007; Jülich and Roths 2010). The increase in the width of the reflected peak, $\Delta\lambda_{wv}$, is given by Eq. (4.6):

$$\Delta\lambda_{wv} = 2\Lambda\left|\Delta n_{effy}\text{-}\Delta n_{effz}\right| = \frac{\Lambda n_0^3}{E_f}\left[(1\text{-}\nu_f)\,p_{12}\text{-}(1+\nu_f)\,p_{11}\right]\left|\sigma_y\text{-}\sigma_z\right| \tag{4.6}$$

where $\sigma_{y,z}$ is the transverse stress, E_f is the elastic modulus of the optical fibre, ν_f is the Poisson's ration, n_0 is the initial refractive index, p_{11} and p_{12} are the photo-elastic coefficients of the optical fibre.

4.3.1.3 Embedded FBG Response: Non-Uniform Strain

A non-uniform strain changes the periodicity of the grating pattern along the sensor length, modifying the grating pattern configuration from "uniform" to "chirped". As demonstrated by Peters et al. (2001), in a uniform grating the applied strain will induce a change in both grating period and the mean index. These two effects can be superimposed by applying an effective strain of "$(1-p_e)\,\varepsilon_1(x)$". Then it is possible to rewrite the grating period as:

$$\Lambda\,(x) = \Lambda_0\,[1 + (1\text{-}p_e)\,\varepsilon_x\,(x)] \tag{4.7}$$

where Λ_0 is the grating period with zero strain. The non-uniform strain effect can be approximated by using the maximum and minimum strain values along the grating. So, the maximum grating period Λ_{max} and minimum Λ_{min} can be calculated using the Eq. (4.1). Thus, an approximated increase of the width of the reflected peak due to a non-uniform strain, $\overline{\lambda}$, is given by combining Eqs. (4.7) and (4.1):

$$\overline{\lambda} = 2n_{eff}\,[\Lambda_{max}\text{-}\Lambda_{min}] \tag{4.8}$$

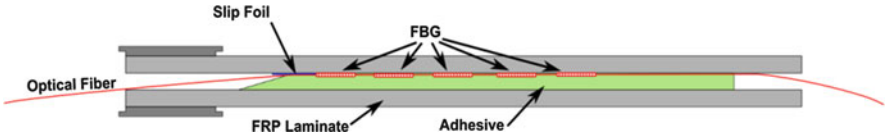

Fig. 4.6 DCB specimen geometry and FBG sensor array configuration

4.3.2 Delamination Detection in Fibre Reinforced Polymer Specimen Using Embedded FBG Sensor: Material and Testing Procedure

To validate the crack detection technique double cantilever beam (DCB) specimens were tested in a fracture testing machine, developed by Sørensen (2010). The DCB specimens were loaded with different combination of moments, giving different type of fracture modes that simulates different crack/delamination cases. The DCB specimens were manufactured using two FRP material arms, made of unidirectional and triaxial glass fibre layers (SAERTEX UD and TRIAX), with a layup stacking of : [90/+45/−45/04/04/+45/−45/90], glued by a commercial epoxy structural adhesive (Epikote MGS BPR 135G/Epikote MGS BPH137G). A thin slip foil was placed in the edge of the structural adhesive, to act as a pre-crack and ease crack initiation.

An array of 5 uncoated single mode (SM) FBG sensors, each with a length of 10 mm, was embedded in the interface of the composite material with the structural adhesive. The gratings array were spaced by 10 mm from each other, and the first grating was positioned 10 mm from the edge of the adhesive. In Fig. 4.6, the DCB specimen and FBG sensor array configuration is presented. The sensors were connected to an Optical Spectral Analyser (OSA) FS2200—Industrial BraggMETER from FiberSensingTM.

4.3.2.1 Experimental Results

In Figs. 4.7 and 4.8, the strain distribution on the surface of the DCB specimen (left pictures) and the FBG sensor output (right picture), before and during the propagation of the crack/delamination are shown. Before the crack starts to propagate in the material, it is observed a build-up of strain caused by the increase of load. Once the crack start to grow, a compression field is formed ahead the crack tip due to the formation of a crack bridging zone. This compression stress area can be observed in Fig. 4.7 (in the top left image, the DIC measurement is shown as a blue spot). At the same time, a decrease in the material compliance due to the growth of the crack causes a rapid local increase of strain, creating a gradient of strain near the crack tip (non-uniform strain), which can be observed in Fig. 4.8 (the bottom left image depicts the DIC measurement).

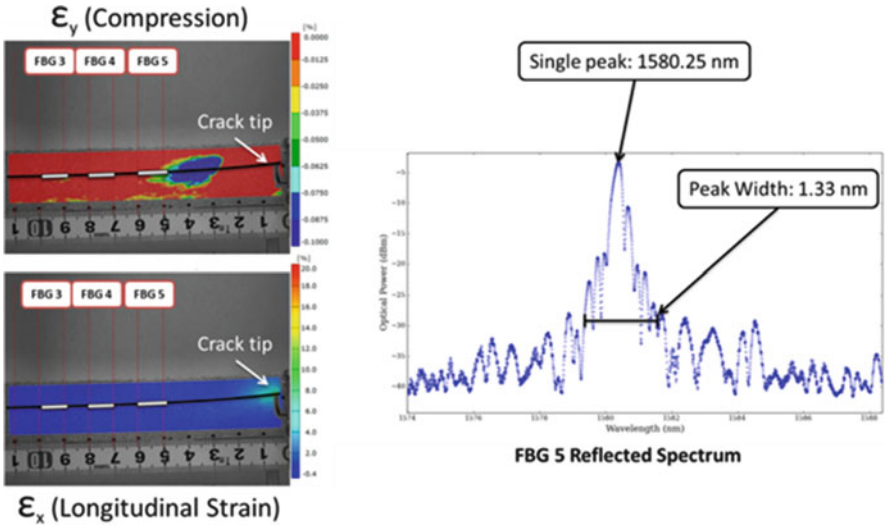

Fig. 4.7 FBG sensor output and DIC measurement before crack growth

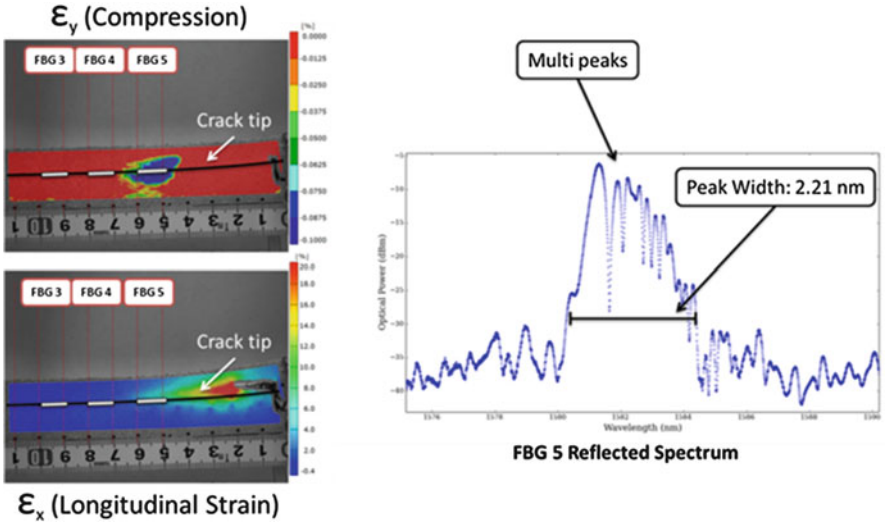

Fig. 4.8 FBG sensor output and DIC measurement during crack growth

The wavelength shift and peak width at −30 dBm, computed from the output of the FBG array in three different loading conditions, it is presented in Fig. 4.9. The different colours plotted correspond to each Bragg grating in the sensor array. The FBG5 (Orange colour line) is the grating located closest to adhesive edge and the FBG1 (Black colour line) is the grating more distant. The crack growth in the order: FBG $5 \rightarrow 4 \rightarrow 3 \rightarrow 2 \rightarrow 1$. The wavelength shift is dependent on the loading

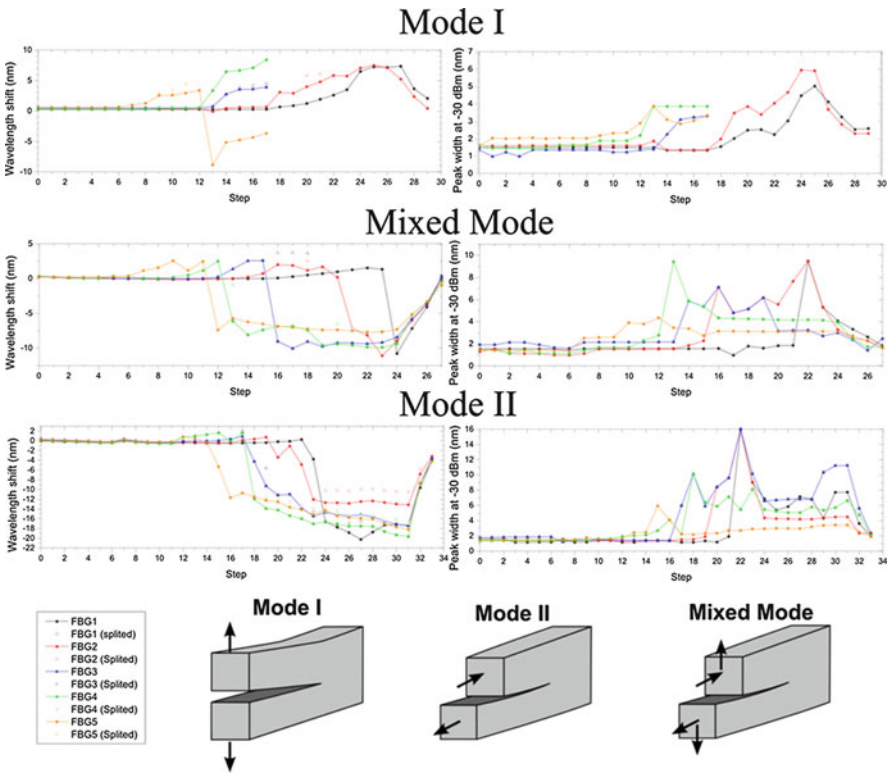

Fig. 4.9 Sensor array output during crack growth

type, but the increase in the width of the peak is related to the presence of the crack (Birefringent effect and non-uniform strain). Using this information it is possible to track the crack by measure an abrupt variation of the wavelength and/or increase in the width of the reflected peak.

4.4 Application of the FBG Crack Detection Method

By using this method it becomes possible to extract two types of information from the sensor: one type dependent of the loading and geometry, ε_{zz}, which give information about the global strain/loading state of the structure; The other type, ε_{zz} (z) and $\sigma_{x,y}$, independent and only affected by the proximity of a crack.

To demonstrate the applicability of this technique to other structures or materials, this monitoring method was implemented in a Finite Element Method (FEM) Model of the DCB specimen, which simulates the response of the FBG sensor during the process of the crack growth, as shown in Fig. 4.10.

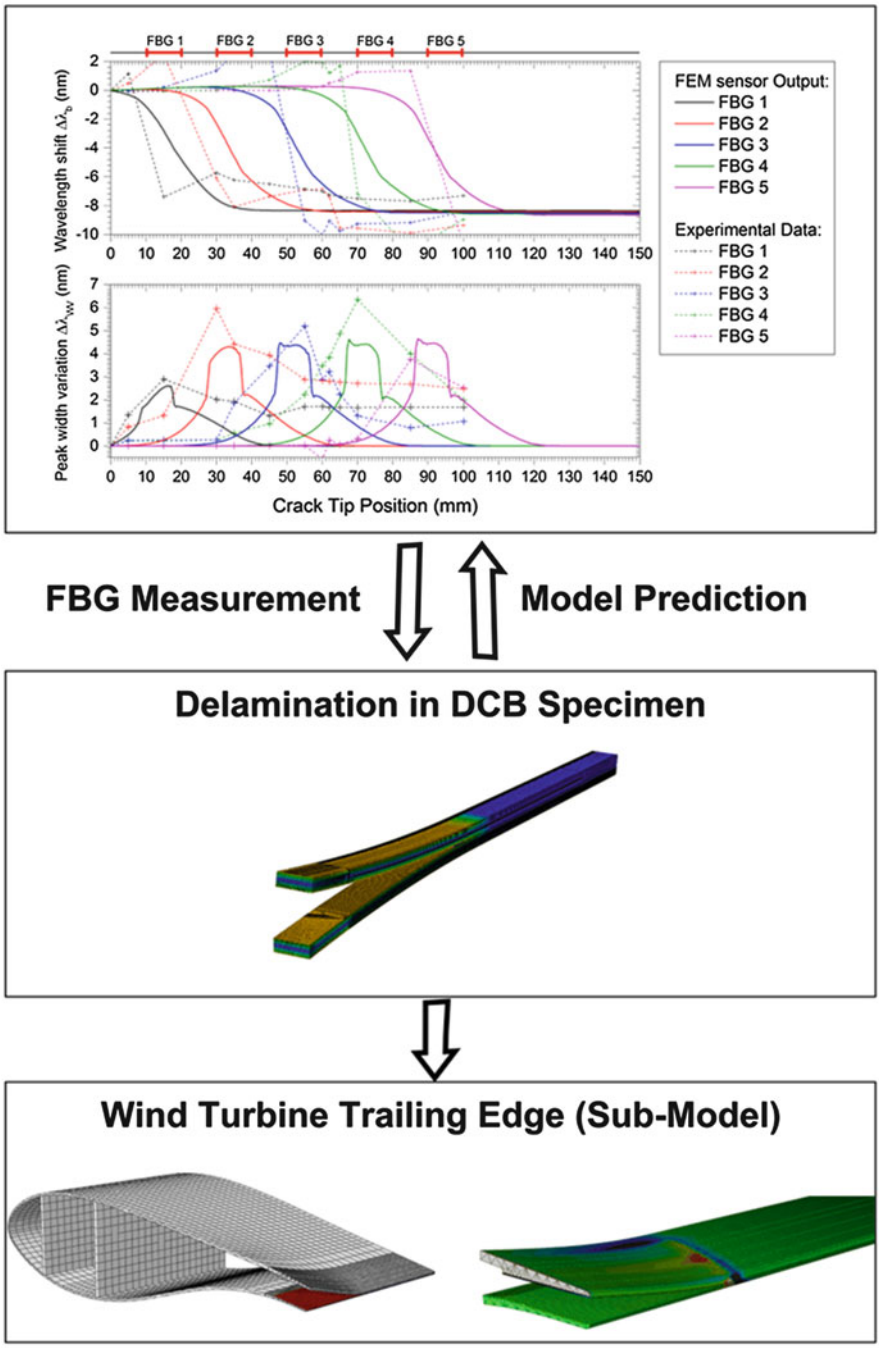

Fig. 4.10 Application of the FBG crack detection method in a DCB specimen and Wind Turbine trailing edge

4.5 Fibre Bragg Grating as a Multi-Stage Structure Health Monitoring Sensor: Published Work

A compiled list of select references pertaining to Fibre Bragg grating sensors and their role in the monitoring structure health at multiple stages:

- Pereira G, Mikkelsen LP, McGugan M (forthcoming) Crack Detection in Fibre Reinforced Plastic Structures Using Embedded Fibre Bragg Grating Sensors: Theory, Model Development and Experimental Validation. Plos One
- Pereira G, Mikkelsen LP, McGugan M (forthcoming) Fibre Bragg Grating Sensor Signal Post-Processing Algorithm: Crack Growth Monitoring in Fibre Reinforced Plastic Structures. Springer Proc Phys
- Pereira G, Mikkelsen LP, McGugan M (2014) Damage tolerant design: failure and crack propagation in composites. In: Abstracts of the 10th EAWE PhD Seminar on Wind Energy in Europe. European Academy of Wind Energy, Orléans, 28–31 Oct 2014
- Pereira G, Mikkelsen LP, McGugan M (2014). FEM model of Embedded Fibre Bragg Grating Sensor Response: Crack Growing Detection. In: Abstracts of the NAFEMS NORDIC – Simulation Verification and Validation (V&V): A Key Enabler for Virtual Product Development, NAFEMS, Copenhagen, 3–4 November 2014
- Pereira G, Mikkelsen LP, McGugan M (2015) Crack Growth Monitoring by Embedded Optical Fibre Bragg Grating Sensors. In: Abstracts of the 3rd International Conference on Photonics, Optics and Laser Technology, Berlin, 13–15 March 2015
- Pereira G, Mikkelsen LP, McGugan M (2015) Embedded Fibre Bragg Grating Sensor Response Model: Crack Growing Detection in Fibre Reinforced Plastic Materials. In: DAMAS 2015. 11th International Conference on Damage Assessment of Structures, Ghent, August 2015. Journal of Physics: Conference Series, Vol 628. Institute of Physics, Temple Back, p 012115. doi:10.1088/1742-6596/628/1/012115
- Pereira G, Mikkelsen LP, McGugan M (2015), Structural Health Monitoring Method for Wind Turbine Trailing Edge: Crack Growth Detection Using Fibre Bragg Grating Sensor Embedded in Composite Materials. Paper presented at the 20th International Conference on Composite Materials, ICCM20, Copenhagen, 19–24 July 2015

References

Hill KO, Meltz G (1997) Fiber Bragg grating technology fundamentals and overview. J Lightwave Technol 15(8):1263–1276

Jülich F, Roths J (2010) Comparison of transverse load sensitivities of fibre Bragg gratings in different types of optical fibres. In: Berghmans F, Mignani AG, van Hoof CA (eds) Optical sensing and detection. SPIE, Brussels, May 2010. SPIE proceedings, vol 7726. SPIE, Washington. doi:10.1117/12.854019

Magne S, Rougeault S, Vilela M et al (1997) State-of-strain evaluation with fiber Bragg grating rosettes: application to discrimination between strain and temperature effects in fiber sensors. Appl Optics 36:9437–9447. doi:10.1364/AO.36.009437

Pereira G, Mikkelsen LP, McGugan M (2015) Embedded fibre Bragg grating sensor response model: crack growing detection in fibre reinforced plastic materials, 2015 In: DAMAS 2015. 11th International conference on damage assessment of structures, Ghent, August 2015. Journal of Physics: Conference Series, Vol 628. Institute of Physics, Temple Back, p 012115. doi:10.1088/1742-6596/628/1/012115

Peters K, Studer M, Botsis J et al (2001) Embedded optical fiber Bragg grating sensor in a nonuniform strain field: measurements and simulations. Exp Mech 41(1):19–28

Sørensen L (2010) Cohesive laws for assessment of materials failure: Theory, experimental methods and application. Dissertation, Technical University of Denmark

Sørensen L, Botsis J, Gmür T et al (2007) Delamination detection and characterisation of bridging tractions using long FBG optical sensors. Compos Part A Appl Sci Manuf 38(10):2087–2096

Chapter 5
Analysis and Design of Bend-Twist Coupled Wind Turbine Blades

Alexander R. Stäblein

Abstract Bend-twist coupling allows wind turbine blades to self-alleviate sudden inflow changes, as in gusty or turbulent conditions, resulting in reduced ultimate and fatigue loads. If the coupling is introduced by changing the fibre direction of the anisotropic blade material, the assumptions of classical beam theory are not necessarily valid. This chapter reviews the effects of anisotropic material on the structural response of beams and identifies those relevant for wind turbine blade analysis. A framework suitable for the structural analysis of wind turbine blades is proposed and guidance for the design of bend-twist coupled blades is given.

5.1 Introduction

Bend-twist coupling (BTC) is used to improve the aeroelastic response of wind turbine blades. As the name suggests, BTC creates a coupling between bending and twist of the blade. The coupling links the aerodynamic forces, which induce bending in the blade, with the twist of the blade. The twist of the blade in turn changes the angle of attack and thereby the aerodynamic forces. This feedback loop, when twisting towards a lower angle of attack, enables the blade to self-alleviate sudden inflow changes, as in gusty or turbulent conditions, leading to a reduction in ultimate and fatigue loads. The aeroelastic response of a bend-twist coupled blade section is illustrated in Fig. 5.1. When subjected to a sudden increase in inflow velocity ΔW the lift force increases and the blade deflects until the elastic forces ΔF are in equilibrium with the increased lift ΔL at deflection Δu, shown in the middle of the figure. For a blade section twisting to feather as shown on the left, the angle of attack reduces by $\Delta\alpha$. A lower angle of attack results in a reduced lift increase $\Delta L - \rho W^2 c\pi\Delta\alpha$ and smaller blade deflections $\Delta u_f < \Delta u$ are required to obtain force equilibrium. For a blade section twisting to stall as shown on the right, the angle of attack increases and with it the lift force $\Delta L + \rho W^2 c\pi\Delta\alpha$ resulting in larger deflections $\Delta u_s > \Delta u$ to obtain equilibrium. As BTC intends to reduce the

A.R. Stäblein (✉)
Department of Wind Energy, Technical University of Denmark (DTU), DTU Risø Campus, Frederiksborgvej 399, 4000 Roskilde, Denmark
e-mail: alsta@dtu.dk

W. Ostachowicz et al. (eds.), *MARE-WINT*, DOI 10.1007/978-3-319-39095-6_5

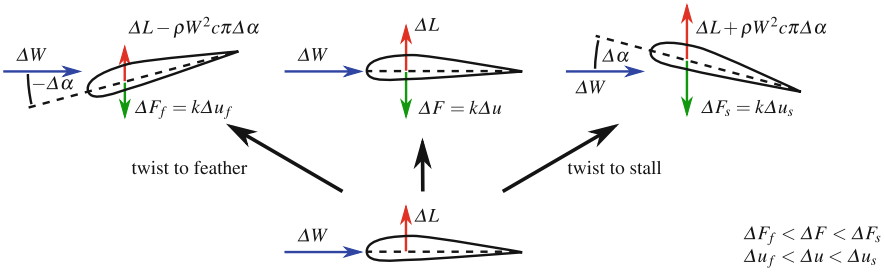

Fig. 5.1 Aeroelastic response to a sudden change in inflow velocity ΔW of a bend-twist to feather coupled (*left*), uncoupled (*middle*) and bend-twist to stall coupled (*right*) blade section

aerodynamic loads on the blade, the coupling is designed to twists towards a lower angle of attack (twist to feather) for modern, pitch regulated wind turbines.

BTC can be achieved by either sweeping the planform of the blade (geometric coupling) which induces additional torsion when the blade is loaded, or by changing the fibre direction of the blade material (material coupling) in the spar caps and/or skin of the blade. The change in fibre direction results in coupling of the normal and shear stresses on lamina level which can be used to induce bend-twist coupling in the cross-section of the beam. The effects resulting from this anisotropic material behaviour are not representable with conventional Euler-Bernoulli or Timoshenko beam theory. This chapter reviews the effects of anisotropic material on the structural response of beams and identifies those relevant for wind turbine blade analysis. A framework suitable for the structural analysis of wind turbine blades is subsequently proposed. The cross-sectional properties of anisotropic beams are discussed and related to classical beam properties. And a Timoshenko beam element for fully coupled cross-sectional stiffness matrices is presented. The next section provides guidance on the design of bend-twist coupled blades and presents a pre-twisting procedure to reduce the power loss associated with coupled blades. To maintain stiffness (e.g. for tower clearance), the blade regions where coupling is most efficiently applied are also identified.

5.2 Analysis of Anisotropic Beams

The analysis of fibre-reinforced polymer (FRP) beams is complex due to the anisotropic properties of the composite material. FRP usually consists of glass or carbon fibres that are embedded in a polymer matrix. Due to the different material properties of fibres and matrix, the longitudinal and transverse stiffness of a FRP ply can differ by several orders of magnitude. A considerable amount of papers have been published on the analysis of anisotropic composite beams. Reviews of those literature is provided by e.g. Hodges (1990b) and Jung et al. (1999). This section provides an overview of the behaviour of composite beams and identifies the

effects that are relevant for wind turbine blade analysis. A framework suitable for the analysis of wind turbine blades is proposed, consisting of cross-section analysis, beam element and co-rotational formulation. The cross-sectional properties of an anisotropic beam are discussed and related to classical beam properties, elastic and shear centre and principle axes. Finally, a Timoshenko beam element for anisotropic beams is presented.

5.2.1 Structural Properties of Anisotropic Beams

Euler-Bernoulli is considered the most fundamental beam formulation. It allows for bending about the two principle axes of the cross-section and extension along the beam axis. It assumes that the cross-section plane remains plane after deformation (i.e. no warping) and perpendicular to the elastic axis of the beam (no shear deformation). The Euler-Bernoulli theory is deemed valid for the static analysis of long, slender beams and the dynamic analysis of lower modes.

5.2.1.1 Shear Deformations

The beam formulation by Timoshenko (1921) allows for transverse shear deformations by dropping the assumption of a cross-section plane that is perpendicular to the beam axis. The 'plane sections remain plane' assumption is maintained. The Timoshenko formulation gives better results for short, stocky beams and the dynamic analysis of higher modes where the wavelength approaches the thickness of the beam. For composite beams, Chandra and Chopra (1992) separate the shear effect into two categories: a direct effect due to the shear stiffness of the section (i.e. Timoshenko) and an effect via shear-related coupling. Smith and Chopra (1991) and Jung et al. (1999) suggest that transverse shear deformations cannot be neglected in composite beams, particularly when coupling is present. Smith and Chopra report that bending-shear coupling reduces the effective bending stiffness of a strongly coupled box-beam by more than 30 %. Volovoi et al. (2001) on the other hand claim that correct deformations can also be obtained with an Euler-Bernoulli formulation if shear deformations are considered correctly when calculating the cross-sectional stiffness. However, in an earlier publication (Rehfield et al. 1990) one of the authors concludes that the direct shear flexibility term may not be negligible and that bending-shear coupling must be present in any general-purpose analysis of composite beams. Cortínez and Piovan (2002) suggest that the shear effect is more important for composite than for isotropic beams due to the high ratio between the longitudinal and transverse modulus of elasticity. Their results show that the shear deformations have a significant effect even on the first frequency of a slender uncoupled composite beam.

5.2.1.2 Torsional Warping

The Euler-Bernoulli and Timoshenko beam theories can be extended by St. Venant's torsion. St. Venant's torsion theory assumes that out-of-plane warping is unrestrained and therefore does not cause axial stress in the section. The free warping assumption is deemed valid for closed sections where torsional warping contributes little to the normal stresses or when warping is unrestrained by e.g. supports. Vlasov's torsion theory allows to restrain the torsional warping by introducing an additional degree of freedom along the beam. The restrained warping can cause significant stresses in the beam direction, in particular for open cross-sections (i.e. I-beams). Chandra and Chopra (1992) show that constrained warping has a stronger influence on the torsional stiffness of composite I-beams than isotropic I-beams. For the closed cross-section beams in their study the constrained warping effect is not important. Rehfield et al. (1990) relate the effect of restrained warping to the decay length which can be split into a material and a geometric part. The geometric part is mainly influenced by the slenderness of the beam. The material part depends on the axial and transverse stiffness and on how much they are coupled. Rehfield et al. (1990) conclude that an additional variable for warping would be important for certain laminated structures. The work of Smith and Chopra (1991) suggests that restrained warping along the beam can have a significant influence on coupled composite beams with closed sections. However, they assume that locally restrained warping is negligible for 'very slender' beams. The results of Cortínez and Piovan (2002) show that torsional warping has a great influence on the vibration and stability behaviour of open sections but it is negligible for closed sections.

5.2.1.3 General Warping

So far, the effects of out-of-plane warping due to transverse shear and in-plane warping have not been considered. Attempts to include those in an analytical solution are made by Smith and Chopra (1991) who introduce the concept of zero net in-plane forces and moments into the constitutive relations of the cross-section. Their results show that load deflection for an anti-symmetric box beam is altered by 30–100 % if in-plane warping is not accounted for. A general approach to calculate the properties of arbitrary cross-sections of anisotropic material is proposed by Giavotto et al. (1983). The formulation invokes the virtual work per unit beam length to obtain a linear system of second-order differential equations with constant coefficients that have a homogeneous and particular solution. The particular (or central) solution is used to determine a 6×6 cross-section stiffness matrix while the homogeneous (or extremity) solution, which is related to warping, is generally ignored. Hodges (1990b) suggests to use the homogeneous solutions to introduce additional degrees of freedom to account for restrained warping at the end of the blade. Another general approach for calculating the cross-section stiffness matrix is proposed by Cesnik and Hodges (1997). The formulation is based on the variational-asymptotic method by Berdichevskii (1979).

5.2.1.4 Superelements

An approach that avoids some of the conjectures of beam analysis is the use of superelements by static condensation. The concept originated from aerospace engineering in the early 1960s (Guyan 1965). Superelements are created by reducing the structural degrees of freedom (static condensation) of a higher fidelity model, often comprised of shell and/or solid elements. While the process of static condensation is reasonably straightforward, due attention must be given to the interpolation function if the many degrees of freedom of a beam cross-section are to be reduced to a single node to obtain beam like elements.

5.2.1.5 Large Displacements

Using non-linear finite element methods, various approaches exist to model a beam undergoing large displacements. Bathe and Bolourchi (1979) present an updated and a total Lagrangian degenerate beam formulation. Variational formulations, where the beam strains are derived from internal virtual work, are proposed by e.g. Simo and Vu-Quoc (1986) and Cardona and Geradin (1988). A further approach is the co-rotational formulation (Crisfield 1990; Battini and Pacoste 2002) that separates rigid body motions from local deformations. The separation is achieved by introducing a local coordinate frame that follows the rigid body motions of the element. Within the local frame (at element level) small displacements and strains are assumed. The method therefore allows to use existing elements (or superelements), which are not able to represent large displacements, in a geometrical non-linear analysis. The co-rotational approach is not restricted to beam elements but also applicable to shell and continuous elements.

The above beam formulations generally assume isotropic material properties. For the large displacement analysis of anisotropic beams, the theory of Giavotto et al. (1983) is extended by Borri and Merlini (1986) to allow for finite strains. Hodges (1990a) presents a mixed variational formulation for the large displacement analysis of anisotropic beams. Kim et al. (2013) present a beam element assuming polynomial shape functions of arbitrary order where the shape function coefficients are eliminated by minimizing the elastic energy of the beam. The element by Stäblein and Hansen (2016) is an extension of a Timoshenko beam element by Bazoune et al. (2003) to allow for the analysis of anisotropic cross-sectional properties. The formulations by Kim et al. (2013) and Stäblein and Hansen (2016) assume small displacements and are intended for the application in a co-rotational or multibody formulation.

5.2.1.6 Wind Turbine Blade Analysis

Wind turbine blades are made of anisotropic material and have a closed cross-section. Previous research indicates that the analysis of blades should therefore consider shear deformations and general warping as those effects have a

considerable influence on the response of anisotropic beams. Restrained warping is less important for closed cross-sections, which also applies for anisotropic beams, and can therefore be neglected. Wind turbine blades are subjected to large displacements ($w/l = 0.14$ for the DTU 10 MW Reference Wind Turbine (DTU 10 MW RWT) (Bak et al. 2013)) and rotations, geometrical non-linear effects should therefore be considered in the analysis. A suitable framework for the analysis of wind turbine blades could be comprised of a cross-section analysis that considers general warping and the coupling effects from the anisotropic material (Giavotto et al. 1983; Borri and Merlini 1986), and a beam element formulation which allows for anisotropic cross-sectional properties and large displacements, either through its formulation (Borri and Merlini 1986; Hodges 1990a) or by embedding it in a co-rotational or multibody formulation (Kim et al. 2013; Stäblein and Hansen 2016).

5.2.2 *Anisotropic Cross-Sectional Properties*

The analysis framework for wind turbine blades proposed above comprises the calculation of anisotropic cross-sectional properties. Those properties are usually expressed in a 6×6 cross-sectional stiffness matrix, the entries of which are briefly discussed below.

A Cartesian coordinate system as shown in Fig. 5.2 is assumed for the cross-section. The beam axis x is normal to the cross-sectional plane which is defined by axes y and z. Displacements and rotations are denoted u_i and θ_i, and forces and moments are F_i and M_i. The indices $i \in \{x, y, z\}$ are used to indicate the direction or rotation axis. By introducing the cross-sectional stiffness matrix

$$\boldsymbol{K}_{cs} = \begin{bmatrix} K_{11} & K_{12} & K_{13} & K_{14} & K_{15} & K_{16} \\ & K_{22} & K_{23} & K_{24} & K_{25} & K_{26} \\ & & K_{33} & K_{34} & K_{35} & K_{36} \\ & & & K_{44} & K_{45} & K_{46} \\ & \text{sym.} & & & K_{55} & K_{56} \\ & & & & & K_{66} \end{bmatrix}, \tag{5.1}$$

the beam strain vector

$$\boldsymbol{\varepsilon} = \{u_x',\ u_y' - \theta_z,\ u_z' + \theta_y,\ \theta_x',\ \theta_y',\ \theta_z'\}^T, \tag{5.2}$$

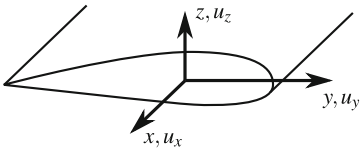

Fig. 5.2 Coordinate system of blade cross-section

where u_i and θ_i are the displacements and rotations of the beam axis and $(\ )'$ are derivatives with respect to x, and the vector of the cross-sectional forces and moments

$$\boldsymbol{F} = \{F_x,\ F_y,\ F_z,\ M_x,\ M_y,\ M_z\}^T, \tag{5.3}$$

the cross-sectional constitutive relation can be written as

$$\boldsymbol{K}_{cs}\boldsymbol{\varepsilon} = \boldsymbol{F}. \tag{5.4}$$

For an isotropic and symmetric beam the diagonal entries K_{jj} for $j \in \{1, \ldots, 6\}$ of the cross-sectional stiffness matrix represent the classical beam properties

$$\begin{aligned} K_{11} &= EA & K_{44} &= GJ \\ K_{22} &= k_y GA & K_{55} &= EI_y \\ K_{33} &= k_z GA & K_{66} &= EI_z \end{aligned} \tag{5.5}$$

where E and G are elastic and shear modulus of the material, A is the area, I_y and I_z are the second moments of area, and J is the torsion constant of the cross-section. The Timoshenko shear coefficients are k_y and k_z. Entries K_{15} and K_{16} of the cross-sectional stiffness matrix are related to the elastic centre (y_e, z_e) which is defined as the point through which the normal force does not induce bending:

$$y_e = -\frac{K_{16}}{K_{11}}, \qquad z_e = \frac{K_{15}}{K_{11}} \tag{5.6}$$

Entries K_{24} and K_{34} of the cross-sectional stiffness matrix are related to the shear centre (y_s, z_s) which is defined as the point through which the shear force resultant does not induce twist:

$$y_s = \frac{K_{34}}{K_{33}}, \qquad z_s = -\frac{K_{24}}{K_{22}} \tag{5.7}$$

Entry K_{56} of the stiffness matrix is related to the angle β between the current axes and the principle axes which are defined as the axes where the moments of area are maximum and minimum and the product moment of area is zero. To obtain the angle β between the current axes and the principle axes, one of the eigenvectors $v = \{v_1, v_2\}^T$ of the sub-matrix $\begin{bmatrix} K_{55} & K_{56} \\ K_{56} & K_{66} \end{bmatrix}$ has to be determined. The angle β is then obtained from:

$$\beta = \arctan\left(\frac{v_2}{v_1}\right) \tag{5.8}$$

Entries K_{45} and K_{46} are associated with bend-twist coupling. Lobitz and Veers (1998) propose a coupling coefficient γ as a measure of bend-twist coupling:

$$K_{45/46} = \gamma \sqrt{K_{44} K_{55/66}}, \quad -1 < \gamma < 1 \tag{5.9}$$

The theoretical limit of $|\gamma| < 1$ results from the requirement of a positive definite stiffness matrix. In a realistic setting values up to 0.2–0.4 are deemed achievable for wind turbine blades (Capellaro and Kühn, 2010; Fedorov and Berggreen, 2014).

The remaining entries are K_{23} which is related to coupling between the shear forces and is usually non-zero for anisotropic beams. Entries K_{12} and K_{13}, which should be expected non-zero if bend-twist coupling is present. And K_{14} which is related to extension-twist coupling. Extension-twist coupling will most probably also cause K_{25}, K_{26}, K_{35} and K_{36} to be non-zero.

5.2.3 *Timoshenko Beam Element with Anisotropic Cross-Sectional Properties*

The anisotropic cross-sectional properties discussed in the previous section require a beam element formulation that accounts for all possible couplings between the cross-sectional forces. One such formulation is the two-noded, three-dimensional Timoshenko beam element proposed by Stäblein and Hansen (2016). The element is an extension of the formulation by Bazoune et al. (2003) to account for fully coupled cross-sectional properties.

The origin of the element coordinate frame is assumed at the first node of the element. The x axis points towards the second node and axes y and z define the cross-sectional plane of the beam as shown in Fig. 5.2. The lateral displacements along the beam axis u_x, and in the cross-sectional plane u_y and u_z are expressed as functions of the coordinate x along the beam length L. A first order polynomial is assumed for u_x and third order polynomials are assumed for u_y and u_z:

$$u_x(x) = c_1 x + c_2 \tag{5.10}$$

$$u_y(x) = c_3 x^3 + c_4 x^2 + c_5 x + c_6 \tag{5.11}$$

$$u_z(x) = c_7 x^3 + c_8 x^2 + c_9 x + c_{10} \tag{5.12}$$

The torsional displacements are expressed by a first order polynomial:

$$\theta_x(x) = c_{11} x + c_{12} \tag{5.13}$$

Timoshenko's assumption that the curvature of the beam equals the slope plus a contribution from shear deformation is used to define the rotational displacements

θ_y and θ_z around the beams cross-sectional axes:

$$\theta_y(x) = -u_z' + c_{13} \tag{5.14}$$

$$\theta_z(x) = u_y' - c_{14} \tag{5.15}$$

In the equations above c_k for $k \in \{1, \ldots, 14\}$ are shape function coefficients. The 14 coefficients are eliminated by introducing two equilibrium equations of the shear force and bending moment relationship:

$$M_y' - F_z = 0, \qquad M_z' + F_y = 0 \tag{5.16}$$

and 12 compatibility conditions (6 nodal displacements + 6 nodal rotations) at the element boundaries $x = 0, L$. With the displacements and rotations along the element determined, the elastic energy of the beam is calculated from:

$$V = \frac{1}{2} \int_0^L \boldsymbol{\varepsilon}^T \boldsymbol{K}_{cs} \boldsymbol{\varepsilon} \, dx \tag{5.17}$$

The element stiffness $\boldsymbol{K}_{el}$ is finally obtained by creating the Hessian of the elastic energy V with respect to the nodal degrees of freedom. The matrix notation of the beam element for implementation in a finite element code is presented in the original publication (Stäblein and Hansen 2016). A Python implementation of the beam element in a three-dimensional co-rotational formulation is available on Git Hub. https://github.com/alxrs/eccomas_2016.git

5.3 Design of Bend-Twist Coupled Blades

Bend-twist coupling intends to reduce the fatigue load of wind turbine blades. Fatigue load alleviation between 10 and 20 % have been observed in previous studies (Lobitz and Veers 2003; Verelst and Larsen 2010). While the load reduction is desired, bend-twist coupling is also associated with a reduction in energy production (Lobitz and Laino 1999; Verelst and Larsen 2010; Bottasso et al. 2013). The reduced energy yield is associated with a no longer optimal twist distribution along the blade. The twist distribution is typically designed to maximize power at a specific tip-speed ratio. For bend-twist coupled blades, however, the twist distribution depends on the bending in the blade which increases with the thrust between cut-in and rated wind speed. Figure 5.3 shows the power and thrust of the DTU 10 MW RWT (Bak et al. 2013) over its operational range. The thrust increases nearly linearly between cut-in at 4 m/s and rated at 12 m/s. With the twist distribution dependant on wind speed it

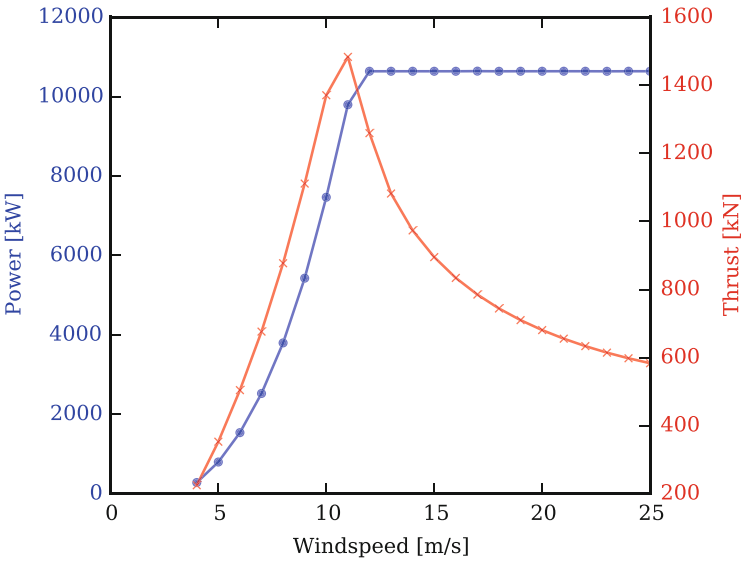

Fig. 5.3 Power and thrust curve of the DTU 10 MW RWT over the operational range

is no longer possible to design the blade for a specific tip-speed ratio. There are two approaches to deal with the non-optimal twist:

(1) Determine the optimal blade twist distribution for a tip-speed ratio (as for uncoupled blades). Choose a reference wind speed at which the twist distribution of the coupled blade should be optimal. Determine the pre-twist of the undeformed blade to match the optimal twist distribution under the aerodynamic load at reference speed.

    The procedure ensures that the twist is optimal for the reference speed. Away from the reference speed the twist distribution will deteriorate. However, the blade can be pitched to improve the energy yield in those regions. The reference speed for pre-twisting is chosen to maximize annual energy production which depends on the wind speed distribution of the site. A pre-twisting procedure for linear blade deflections is proposed by Lobitz and Veers (2003) and extended to non-linear blade deflections by Stäblein et al. (2016). The latter show that pre-twisting significantly reduces the power loss in annual energy production of the DTU 10 MW RWT.

(2) Optimize the twist, and probably also the chord, distribution of the coupled blade for a given wind speed distribution. The tip-speed ratio might also be considered an optimization variable. To the authors knowledge there has not been a study that pursued this approach.

In the following, the pre-twist procedure presented by Stäblein et al. (2016) is revisited. As a constant coupling coefficient is applied along the length of the blade,

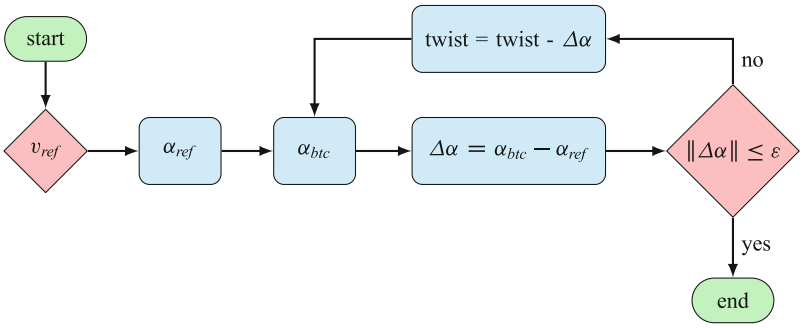

Fig. 5.4 Flowchart of the pre-twisting procedure presented by Stäblein et al. (2016)

the resulting pre-twist distribution provides a good indication of the blade regions where coupling is most efficient.

5.3.1 Pre-Twisting Procedure

Pre-twisting adjusts the structural twist of a coupled blade in an iterative procedure to provide the same angle of attack along the blade as the uncoupled blade for a given reference wind speed. The first step is to calculate the steady state angle of attack along the uncoupled α_{ref} and coupled blade α_{btc} at the reference wind speed v_{ref}. The angle of attack is chosen as a reference as it results in the same aerodynamic state, irrespective of the blade twist which is not uniquely defined for large displacements and rotations. The difference between the angles of attack $\Delta\alpha$ is then imposed on the coupled blade as a pre-twist. Both steps are repeated until the angle of attack along the uncoupled and coupled blade are identical at the reference speed. A flowchart of the procedure is shown in Fig. 5.4. The power curve is further improved by recalculating the optimal pitch angle over the operational range of the turbine. Pre-twisting results in an identical angle of attack along the blade at the reference wind speed v_{ref}. Below the reference speed, the thrust on the blade is lower which results in reduced bending and consequently less coupling induced twist. The blade therefore has a higher angle of attack slope along the blade as the blade twists towards stall. In this region, it is important to consider the angle of attack limit when determining the optimal pitch angle in order to avoid flow separation. Above the reference speed, where thrust is larger, the coupling will result in a lower angle of attack slope along the blade as the blade twists towards feather.

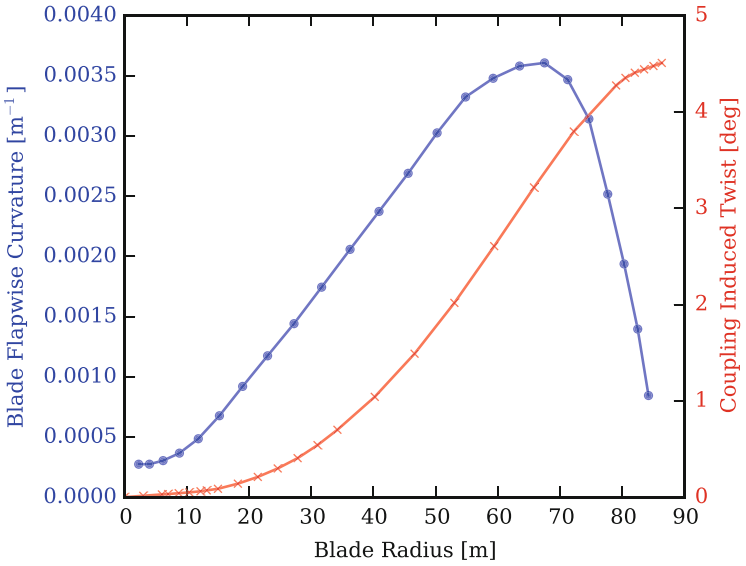

Fig. 5.5 Blade flapwise curvature and coupling induced twist at 8 m/s wind speed (Stäblein et al. 2016)

5.3.2 Coupling Distribution

If bend-twist coupling is introduced by utilising the anisotropic properties of the blade material, the change in fibre direction in the spar caps and/or skin of the blade results in a reduced bending stiffness. Previous studies (Fedorov and Berggreen 2014) have shown that coupling reduces the bending stiffness of the blade by 30–35 % when no material is added. As the tower clearance of the blade tip is often a governing design criteria a loss in stiffness is undesirable and it is advisable to introduce the coupling only in blade regions where it is most efficient. Figure 5.5 shows the coupling induced twist and the flapwise curvature at 8 m/s reference speed for the DTU 10 MW RWT with a constant flap-twist to feather coupling coefficient of 0.2 along the blade. It can be seen that the curvature correlates with the slope of the induced twist. The relationship can also be shown by reducing the cross-sectional constitutive relation (5.4) to flapwise moment and torsion. Assuming torsion to be zero, a linear relationship between curvature and twist rate can be established:

$$\begin{bmatrix} K_{44} & K_{45} \\ K_{45} & K_{55} \end{bmatrix} \begin{Bmatrix} \theta_x' \\ -u_z'' \end{Bmatrix} = \begin{Bmatrix} 0 \\ M_y \end{Bmatrix} \quad \Rightarrow \quad \theta_x' = \frac{K_{45}}{K_{44}} u_z'' \tag{5.18}$$

Returning to Fig. 5.5, the curvature-twist relationship shows that, for the DTU 10 MW RWT, coupling is most efficient in the outer half of the blade. A similar

observation is also made by Bottasso et al. (2013) who show that partially coupled blades exhibit a similar load alleviation performance as fully coupled blades.

5.4 Summary

Bend-twist coupling is a proven technique to reduce the fatigue loads of wind turbine blades. If the coupling is introduced by changing the fibre direction of the anisotropic blade material, it is important to account for the effects the material has on the structural response of the blade. Previous research indicates that shear deformations, general warping and the geometric non-linearity from large displacements need to be considered. An analysis framework that includes all those effects, consisting of cross-section analysis, beam element and co-rotational formulation, has been presented in this chapter. When designing bend-twist coupled blades, pre-twisting can be used to reduce the power loss associated with the coupling. To maintain blade stiffness for tower clearance while utilizing the load alleviation potential of coupled blades, the coupling should only be introduced in regions with high curvature as this is where it is most efficient.

References

Bak C, Zahle F, Bitsche R, et al (2013) The DTU 10-MW reference wind turbine. In: DTU orbit - the research information system. Available via Technical University of Denmark. http://orbit.dtu.dk/files/55645274/The_DTU_10MW_Reference_Turbine_Christian_Bak.pdf. Accessed 08 Apr 2016

Bathe KJ, Bolourchi S (1979) Large displacement analysis of three-dimensional beam structures. Int J Numer Methods Eng 14(7):961–986

Battini JM, Pacoste C (2002) Co-rotational beam elements with warping effects in instability problems. Comput Method Appl M 191(17):1755–1789

Bazoune A, Khulief YA, Stephen NG (2003) Shape functions of three-dimensional Timoshenko beam element. J Sound Vib 259(2):473–480

Berdichevskii VL (1979) Variational-asymptotic method of constructing a theory of shells. J Appl Math Mech 43(4):711–736

Borri M, Merlini T (1986) A large displacement formulation for anisotropic beam analysis. Meccanica 21(1):30–37

Bottasso CL, Campagnolo F, Croce A, Tibaldi C (2013) Optimization-based study of bend-twist coupled rotor blades for passive and integrated passive/active load alleviation. Wind Energy 16(8):1149–1166

Capellaro M, Kühn M (2010) Boundaries of bend twist coupling. In: Voutsinas S (ed) Torque 2010: the science of making torque from wind, Crete, 2010

Cardona A, Geradin M (1988) A beam finite element non-linear theory with finite rotations. Int J Numer Methods Eng 26(11):2403–2438

Cesnik CES, Hodges DH (1997) VABS: a new concept for composite rotor blade cross-sectional modeling. J Am Helicopter Soc 42(1):27–38

Chandra R, Chopra I (1992) Structural response of composite beams and blades with elastic couplings. Compos Eng 2(5–7):347–374, wOS:A1992HZ76200006

Cortínez VH, Piovan MT (2002) Vibration and buckling of composite thin-walled beams with shear deformability. J Sound Vib 258(4):701–723

Crisfield MA (1990) A consistent co-rotational formulation for non-linear, three-dimensional, beam-elements. Comput Method Appl M 81(2):131–150

Fedorov V, Berggreen C (2014) Bend-twist coupling potential of wind turbine blades. J Phys Conf Ser 524:012035

Giavotto V, Borri M, Mantegazza P, Ghiringhelli GL, Carmaschi V, Maffioli GC, Mussi F (1983) Anisotropic beam theory and applications. Comput Struct 16(1):403–413

Guyan RJ (1965) Reduction of stiffness and mass matrices. AIAA J 3(2):380–380

Hodges DH (1990a) A mixed variational formulation based on exact intrinsic equations for dynamics of moving beams. Int J Solids Struct 26(11):1253–1273

Hodges DH (1990b) Review of composite rotor blade modeling. AIAA J 28(3):561–565

Jung SN, Nagaraj VT, Chopra I (1999) Assessment of composite rotor blade modeling techniques. J Am Helicopter Soc 44(3):188–205

Kim T, Hansen AM, Branner K (2013) Development of an anisotropic beam finite element for composite wind turbine blades in multibody system. Renew Energ 59:172–183

Lobitz DW, Laino DJ (1999) Load mitigation with twist-coupled HAWT blades. In: ASME/AIAA wind energy symposium, Reno, NV, pp 124–134

Lobitz DW, Veers PS (1998) Aeroelastic behavior of twist-coupled HAWT blades. In: ASME/AIAA wind energy symposium, Reno, NV, pp 75–83

Lobitz DW, Veers PS (2003) Load mitigation with bending/twist-coupled blades on rotors using modern control strategies. Wind Energy 6(2):105–117

Rehfield LW, Atilgan AR, Hodges DH (1990) Nonclassical behavior of thin-walled composite beams with closed cross sections. J Am Helicopter Soc 35(2):42–50

Simo J, Vu-Quoc L (1986) A three-dimensional finite-strain rod model. Part II: computational aspects. Comput Method Appl M 58:79–116

Smith EC, Chopra I (1991) Formulation and evaluation of an analytical model for composite box-beams. J Am Helicopter Soc 36(3):23–35

Stäblein AR, Hansen MH (2016) Timoshenko beam element with anisotropic cross-sectional properties. In: VII European congress on computational methods in applied sciences and engineering (ECCOMAS 2016), Crete Island

Stäblein AR, Tibaldi C, Hansen MH (2016) Using pretwist to reduce power loss of bend-twist coupled blades. In: 34th wind energy symposium, p 1010

Timoshenko SP (1921) On the correction for shear of the differential equation for transverse vibrations of prismatic bars. Philos Mag 41(245):744–746

Verelst DR, Larsen TJ (2010) Load Consequences when sweeping blades - a case study of a 5 MW pitch controlled wind turbine. Tech. Rep. Risø-R-1724(EN), Risø National Laboratory for Sustainable Energy

Volovoi VV, Hodges DH, Cesnik CES, Popescu B (2001) Assessment of beam modeling methods for rotor blade applications. Math Comput Modell 33(10–11):1099–1112

Chapter 6
Improvement of Wind Turbine Blade Performance by Means of Rod Vortex Generators

Javier Martinez, Pawel Flaszynski, Piotr Doerffer, and Oskar Szulc

Abstract Wind turbines are complex energy conversion fluid-flow machines which entail coupled aero-mechanical issues. From an aero-acoustical point of view, wind turbine blades present two main problems: first, a reduced aerodynamic performance due to flow separation, and second, the level of noise emissions. Flow separation appears on the blade as a result of high angles of attack causing a decrease in the aerodynamic efficiency. In this chapter, the application of rod vortex generators (RVGs) to control and decrease the flow separation—by the creation of streamwise vorticity on the blade—is presented. The NREL Phase VI wind turbine rotor and the S809 airfoil are used as reference cases. The validation of NREL Phase VI model rotor against experimental data is found to be satisfactory. A study into the effects of RVGs' chordwise location and spanwise distance is presented for selected cases and a range of inflow conditions. It is shown that the proposed RVGs lead to an improvement of the aerodynamic performance, and can be successfully applied by the wind energy industry.

6.1 Introduction

The wind energy sector has experienced rapid growth in the last few decades. The developments in the materials science, engineering and allied fields have ushered in turbines of increasing sizes; turbines with rotor diameters of up to 160 m (Vestas V164 8 MW) have been developed, and the current trend of increasing sizes is expected to continue in the future (Bak et al. 2012).

The increasing sizes of wind turbines pose new challenges for engineers. One particular challenge is that large rotor dimensions result in non-uniform inflow conditions along the blade span—which leads to increased flow separation even after the application of traditional flow control approaches. As a consequence of

J. Martinez (✉) • P. Flaszynski • P. Doerffer • O. Szulc
Aerodynamics Department, Institute of Fluid Flow Machinery, Polish Academy of Sciences, ul. Fiszera 14, 80-231 Gdańsk, Poland
e-mail: javier.martinez@imp.gda.pl; pawel.flaszynski@imp.gda.pl; piotr.doerffer@imp.gda.pl; oskar.szulc@imp.gda.pl

W. Ostachowicz et al. (eds.), *MARE-WINT*, DOI 10.1007/978-3-319-39095-6_6

the boundary layer separation, the air flow on the blade is detached leading to increased aerodynamic losses and noise generation (Wagner et al. 2012). In order to reduce the flow separation, different flow control devices have been developed and implemented on the blades during the last few decades (Van Dam et al. 2008). Several flow control devices, such as trailing edge flaps, microtabs, microflaps, plasma actuators, active flexible walls or vortex generators, have been proposed in literature (Van Dam et al. 2007, 2008; Andersen et al. 2010; Johnson et al. 2010; Nelson et al. 2008; Gao et al. 2015). Of these, the current chapter focuses on vortex generators.

Vortex generators (VGs) are located in the boundary layer in order to create a streamwise vorticity, which influences the transport of momentum in the direction normal to the wall. The fluid with higher momentum transported to the near wall zone energizes the boundary layer. This leads to increased shear stresses and higher resistance to the adverse pressure gradient effect which results in reduction or even complete removal of the separation.

The first VG investigations were conducted by Taylor (1947) in the late 1940s. These initial devices, of height (h) higher or equal to the boundary layer (δ), were called vane vortex generators (VVGs). During the 1950s, air jet vortex generators (AJVGs) were developed. It was found that they could be considered as an effective alternative to traditional VGs for separation reduction (Wallis and Stuart 1962). In the 1980s, Taylor's VGs were replaced by smaller devices, with the introduction of low profile VGs ($h/\delta < 0.65$) (Rao and Kariya 1988); these devices generate lower disturbance and flow non-uniformity outside boundary layer in comparison with the classical vanes as they are submerged inside the boundary layer. As an effect, the drag is lower and the effectiveness of the flow control method can be higher. However, these devices generally need to be located closer to the critical zone than classical vanes due to faster decaying streamwise vorticity (Lin 2002).

In the last few decades VGs have been widely researched and new concepts of non-solid VGs—such as synthetic jets or pulsed jets (Lin 2002; Wiltse and Glezer 1993; Amitay et al. 1998; McManus et al. 1994; Kostas et al. 2007)—have been proposed. It has been demonstrated that active VGs provide similar benefits as passive VGs, but with a major added advantage: when they are not functional, there is no increment in the parasitic drag (Paul et al. 2013). Despite the clear benefits of active VGs, different configurations of vane-type VGs are still a commonly implemented solution on wind turbine blades.

This chapter focuses on the investigation and application of a new type of VG, called Rod Vortex Generator (RVG) (Doerffer et al. 2009), on wind turbine blades. Optimized RVGs have demonstrated a capability to generate similar streamwise vortex intensity as the one generated by the AJVGs (Tejero et al. 2015). Furthermore, RVGs do not require complex installation, as is the case with AJVGs. In contrast to the traditional vane-type VGs, RVGs can be combined with Micro-Electro-Mechanical Systems (MEMS) technology, thus allowing for activation during the system operation if the conditions require its application.

RVGs can be defined by five parameters: diameter (D), height (h), skew angle (θ), pitch angle (α) and spacing (W), as shown in Fig. 6.1. The first four parameters

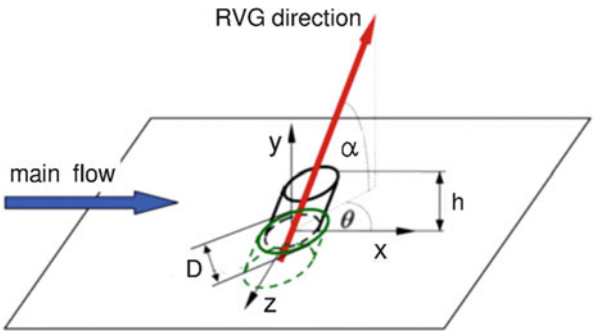

Fig. 6.1 Rod vortex generator configuration

define the geometry and orientation of the rod, while the spacing (W) refers to the spanwise distance between rods. The orientation angles (θ and α) are optimized to obtain the maximum streamwise vorticity. The rod diameter and the height are proportional to the boundary layer thickness. The chordwise location of the RVG along the blade (x_{RVG}/c) is also a crucial parameter which has to be taken into account.

The application of RVGs on wind turbine blades, as a flow control device to improve aerodynamic performance, is analysed for the NREL Phase VI wind turbine rotor. The NREL turbine was selected because of the large amount of experimental data available (Hand et al. 2001) and the detailed geometry description (Lindenburg 2003) which is highly advantageous for the validation step.

6.2 Flow Solver

The numerical investigations have been carried out by means of FINE™/Turbo Numeca. The compressible, mass-weighted RANS equations are solved adopting a preconditioning scheme (Hakimi 1997; Choi and Merkle 1993). A full multigrid technique is applied in order to increase the convergence rate. Spatial discretization is based on a cell centred control volume approach, and a 2nd order central difference scheme with scalar artificial dissipation formulated by Jameson (1991) is applied. The results presented in this chapter are obtained for turbulence models (Spalart and Allmaras 1992), k-ω SST (Menter 1994) and Explicit Algebraic Reynolds Stress Model (EARSM) (Menter et al. 2012). A perfect gas model is employed for closure of the system of differential equations. The dynamic viscosity is calculated using the Sutherland's law (Sutherland 1893).

6.3 The NREL Phase VI Wind Turbine Rotor

6.3.1 Experimental Set-Up

The computational model is validated by the comparison of numerical simulations results with the experimental data available in the National Renewable Energy Laboratory (NREL) database for the Unsteady Aerodynamics Experiment Phase VI (Hand et al. 2001). The geometry of the investigated configuration is shown in Fig. 6.2.

The two-bladed rotor was located in the 24.4 m × 36.6 m NASA Ames Wind Tunnel and tested under several different inflow conditions, with velocities ranging from 0 to 25 m/s. The stall regulated rotor was equipped with two linearly tapered, non-linearly twisted blades of radius R = 5.209 m with rounded tip caps (Lindenburg 2003). The tapered region of the blades starts at r/R = 0.25 with a chord length c = 0.737 m, and ends at the tip, c = 0.357 m. The non-linearly twisted blade, defined with respect to the r/R = 0.75 section and considered positive towards feather, varies from 20.05° at r/R = 0.25 to −1.82° at tip.

During the sequence S of the experimental campaign (Hand et al. 2001), the blade tip pitch angle was set to 3° with respect to the rotor plane, the rotational speed to 72 rpm, and the cone angle to 0°. Static pressure measurements were obtained at five spanwise locations (r/R = 0.3, 0.466, 0.633, 0.80 and 0.95). Yaw angles were varied from 0 to 180°, but only the results from the 0° yaw angle case were harnessed for validation purposes. In the present work, only wind speeds of 5,7,10 and 13 m/s are considered. Table 6.1 summarizes the operational conditions for the computed cases (Hand et al. 2001; Sørensen and Michelsen 2000).

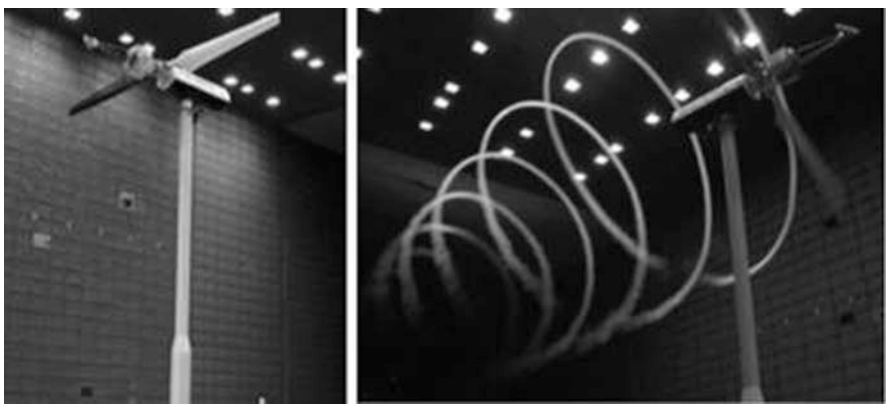

Fig. 6.2 NREL Phase VI wind turbine at NASA Ames (Lindenburg 2003)

Table 6.1 NREL Phase VI operating conditions

Wind speed [m/s]	Density (ρ) [kg/m^3]	RPM	Temperature [K]
5.0	1.243	71.7	284.25
7.0	1.246	71.9	284.25
10.0	1.246	72.1	284.15
13.1	1.227	72.1	286.85

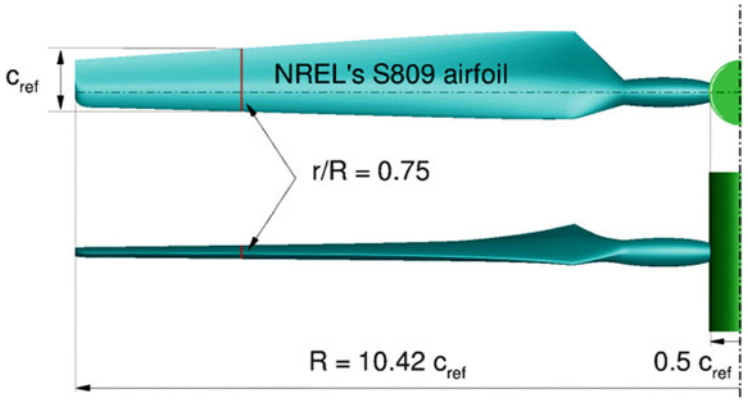

Fig. 6.3 NREL Phase VI rotor model

6.3.2 Numerical Modelling

A numerical model is created for the NREL Phase VI rotor. The section $r/R = 0.75$ was taken as the reference section, and the local chord was set to unit ($c_{ref} = 1$). The blade radius to reference chord length ratio (AR $\approx$ 10.42) was kept constant in comparison with the full scale model. Thus the blade radius was rescaled to $R = \text{AR} \cdot c_{ref}$. The pitch and sectional twists were not affected by the process. The nacelle was modelled as a cylinder with radius $0.5 \cdot c_{ref}$ (Fig. 6.3) (Martinez et al. 2015a).

The rotational periodicity of the flow allows the use of a computational domain defined by a half of cylinder with a single blade in the middle. Farfield boundary conditions are applied at the outer cylinder, located at a distance of 3 blade radius (R) from the rotor axis. The inlet and outlet are located at a distance equal to $3 \cdot R$ from the rotor plane. At the inlet, a uniform velocity distribution in normal direction to the rotor plane is applied, while at the outlet, atmospheric static pressure is imposed. The blade is defined as a non-slip wall, while at the cylindrical surface (hub) an Euler wall (no shear stress at the wall) condition is applied. This enables one to save resources and computational time (Fig. 6.4).

The computational domain consists of 8.8 million cells distributed amongst 76 hexahedral full-matching connection blocks. The structured grid is of C type in the crosswise direction, and H type in the spanwise and freestream directions, as shown

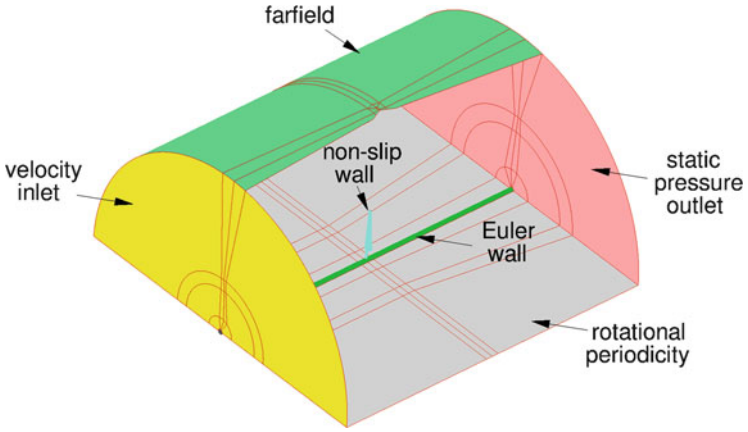

Fig. 6.4 NREL Phase VI rotor computational domain and boundary conditions

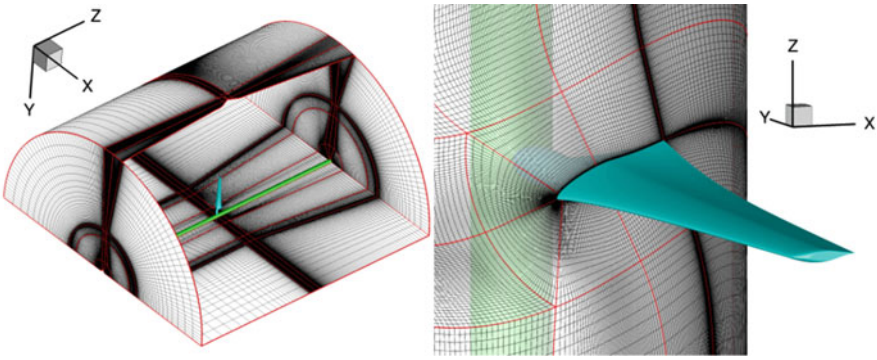

Fig. 6.5 NREL Phase VI rotor C-H-H grid

in Fig. 6.5. The blade surface is discretized by 294 nodes around the airfoil and 91 nodes in the spanwise direction. The non-dimensional distance of the first cell layer close to the wall is of the order of $y^+ \sim 1$.

6.3.3 Numerical Results

The numerical simulations for the NREL wind turbine rotor show good agreement with measurements of the total thrust and torque. The only difference noted is for a wind speed 10 m/s (Fig. 6.6), where torque is over-predicted (Martinez et al. 2015b).

It is shown in Fig. 6.6 that the predictions obtained by means of 2-equation k-ω SST and EARSM models are almost identical. One has to emphasize that in case of

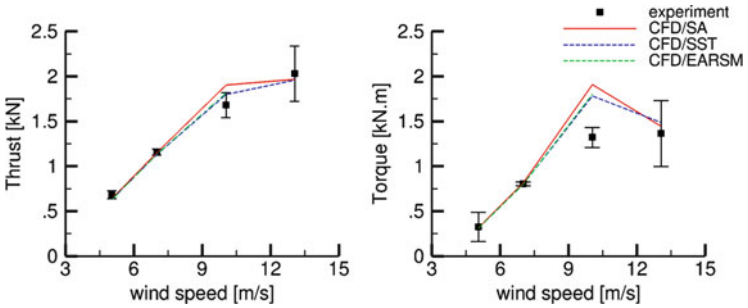

Fig. 6.6 Integrated thrust (*left*) and torque (*right*) for NREL Phase VI rotor

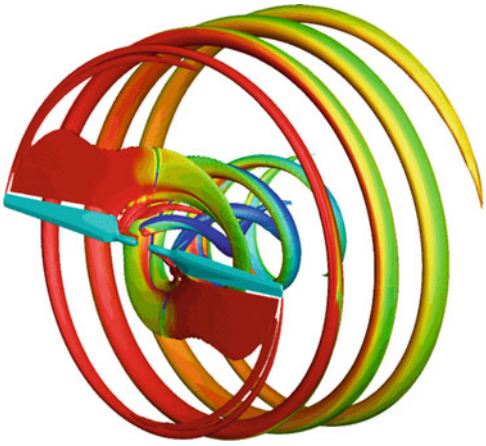

Fig. 6.7 NREL Phase VI rotor aerodynamic wake at 5 m/s

thrust measurements, computed values are within the measurement accuracy. The discrepancy is higher for the SA model.

A Q-criterion (coloured by the vorticity magnitude) visualization of the rotor wake (Fig. 6.7) was extracted from the numerical solution for an inflow wind velocity of 5 m/s, and the one equation Spalart-Allmaras turbulence model. The rotor wake created by wind turbines is closely related to the amount of energy extracted from the wind, and its prediction is of primary importance in the assessment of performance and power. An example of the wake prediction by numerical model, described in more details in Martinez et al. (2015a, b), is shown in Fig. 6.7.

For validation purposes a more detailed analysis of the flow properties (particularly, flow attachment state and local blade loading) is needed. The blade surface streamlines and friction coefficient c_f provide information of utmost importance regarding the flow attachment state and developed flow patterns. The blade loading analysis is given by the sectional chordwise pressure coefficient c_p, and spanwise

normal c_N and tangential c_T force coefficients distributions. The friction coefficient c_f is defined as:

$$c_f = \frac{\mu \frac{du_s}{dn}}{0.5\rho U_\infty{}^2} \tag{6.1}$$

where u_s is the component of cross sectional velocity tangential to the surface, n is the direction normal to the blade surface, U_∞ the cross sectional reference velocity, μ the freestream viscosity and ρ the density.

The friction coefficient c_f along with velocity streamlines are shown in Fig. 6.8 for the 4 wind speeds ranging from 5 to 13 m/s. Contours for c_f, obtained only from the Spalart-Allmaras turbulence model, are shown. Analogous behavior is observed in case of the two equation turbulence models.

It is observed that in the case of 5 and 7 m/s wind speeds, the flow stays fully attached—except for the inner section, where the cylindrical shape (close to root) induces local separation. At 10 m/s, according to the SA model prediction, the previous local separation moves towards the outer span of blade until $r/R = 0.95$. The plot for the wind speed of 13 m/s reveals that the flow is completely detached on the suction side, except for a very narrow region at the blade tip. Further increasing of the wind speed causes the detached flow area to increase.

An example of pressure coefficient distributions c_p located at four blade cross sections (r/R = 0.30, 0.466, 0.80 and 0.95) and the non-dimensional force coefficient c_N are compared to the experimental data in the Figs. 6.8 and 6.9 for wind

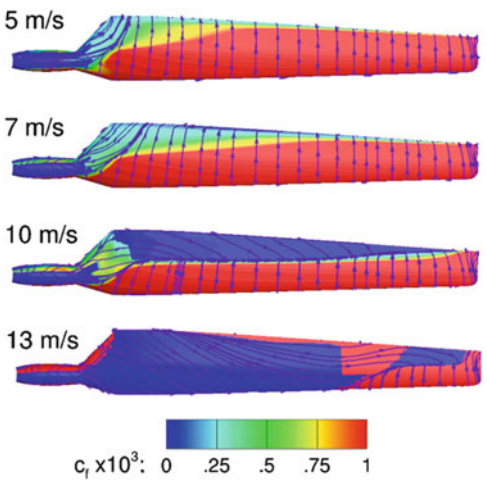

Fig. 6.8 Skin friction coefficient c_f and surface streamlines (suction side)

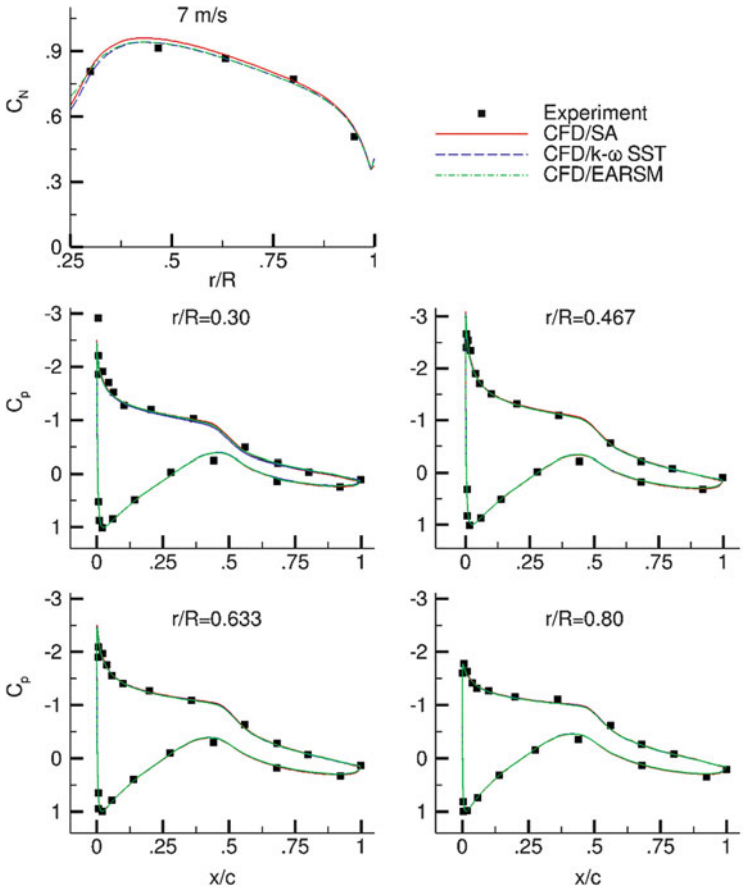

Fig. 6.9 Pressure coefficient c_p and normal force c_N distributions at 7 m/s

speeds of 7 and 10 m/s, respectively. The sectional normal force coefficient c_N distributions predictions were obtained by the integration of the c_p distributions along each one of the 100 cross sections employed. Figure 6.9 shows an exemplary agreement with the experimental data. A slight difference among models is observed at the 30 % cross section.

As the wind speed increases to 10 m/s the prediction of SA model fails to reproduce the normal force coefficient distribution, although the k-ω SST and EARSM models predictions are still close to the experimental data (Fig. 6.10). The 10 m/s case shows important discrepancies between the c_p distribution predicted and the experimental data for the 46.6 % span section. The experimental data seems to show a local separation at this section, which is not predicted by numerical simulations, while a reasonably good agreement with the experimental data is obtained in the remaining sections.

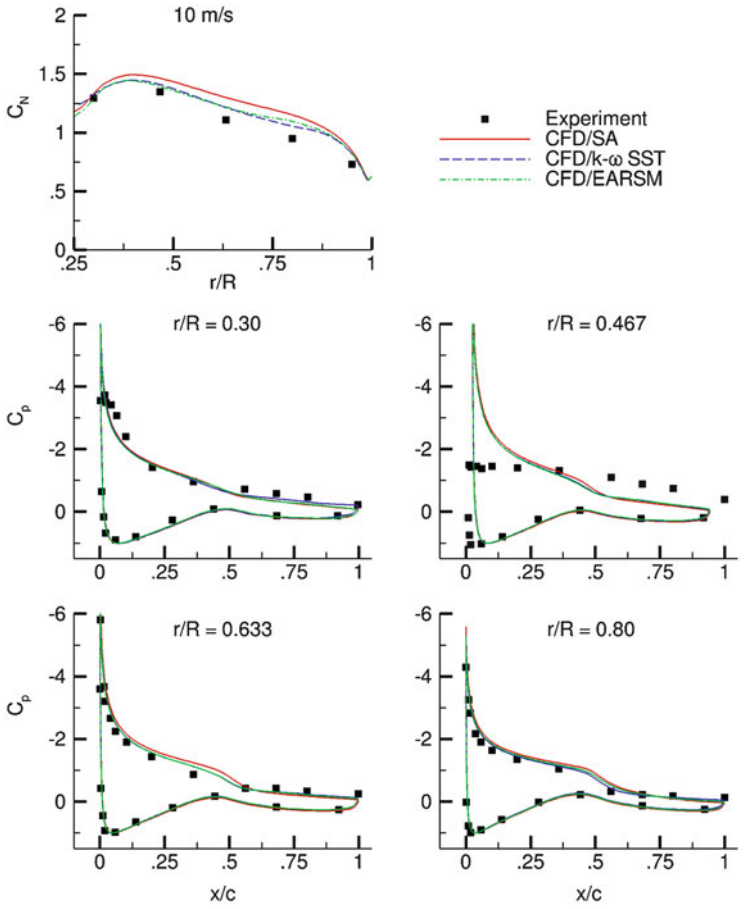

Fig. 6.10 Pressure coefficient c_p and normal force distributions c_N at 10 m/s

Disregarding the 46.6 % span section, a reasonably good agreement between experimental and numerically predicted c_p distributions has been shown for the turbine operating at wind speeds ranging from 5 to 13 m/s (see Martinez et al. 2015a). Consequently, a flow structure similar to the displayed in Fig. 6.8 is expected to have been developed during the experimental campaign.

The optimum tip speed ratio is close to 5.4 (wind speed 7 m/s) (Martinez et al. 2015a, b); thus, as the wind speed increases beyond the optimum, the flow separation comes out on the blade, affecting the rotor performance. It influences the rising flow structure complexity, and causes difficulties with the prediction accuracy of the solver. The area of detached flow in the 10 m/s case is quite susceptible of being decreased by means of rod vortex generator, thus improving the aerodynamic

performance and delaying the separation as the wind speed increases. When the flow on the blade is totally detached, however, the application of RVGs is not expected to bring significant (if any) aerodynamic improvement. Besides, modern horizontal axis wind turbine rotors equipped with individual pitch control are more likely to operate with partially flow-separated blades, than in a strong stall situation. Thus the 10 m/s case is chosen as a reference for a flow control study in wind turbines.

6.4 The S809 Aerofoil (Clean Case)

The NREL Phase VI rotor blades employ the 21 % thickness S809 aerofoil. For this reason a validation study is performed for this aerofoil. Designed for wind turbines applications using the Eppler code (Eppler and Somers 1980), a short ramp of adverse pressure is present on the upper surface of this profile, downstream of the mid-chord. It promotes an efficient laminar to turbulent transition, followed by a low drag concave pressure recovery region (Somers 1997).

The S809 aerofoil was tested in the Ohio State University (OSU) and Delft University of Technology (DUT) facilities and experimental data is available for several angles of attack (Somers 1997) and Reynolds numbers (Ramsay et al. 1995). The validation against experimental data was performed for a Reynolds number of $1 \cdot 10^6$ to ensure that the analysis was representative of the studied flow around the NREL Phase VI blade.

The aerofoil surface was modelled as a non-slip wall. A C type grid was used, and the farfield was located at 40 chords from the aerofoil. The total computational cells amount to 0.3 million, distributed into 13 blocks. The S809 aerofoil surface is defined by 737×145 nodes in the wrap-around and normal directions, respectively (Fig. 6.11).

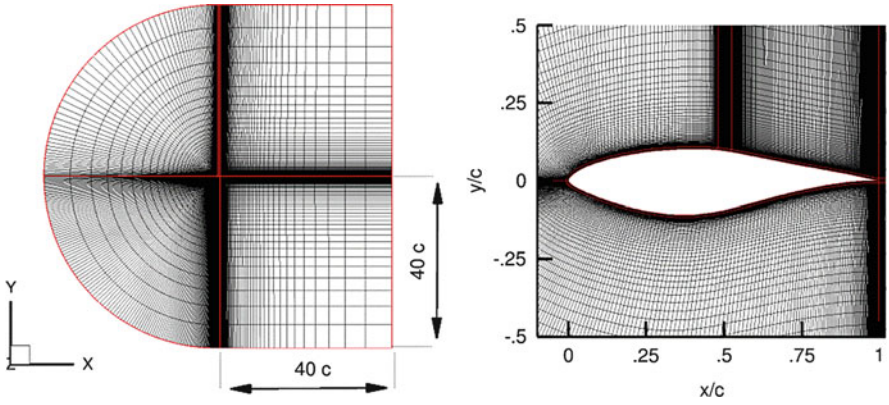

Fig. 6.11 C type grid around the S809 aerofoil

Numerical RANS simulations were performed with and without a transition model. The γ - Re_θ transition model is used. This model is based on two transport equations, one for intermittency, γ, and the second one for the transition momentum thickness Reynolds number, Re_θ. For simulations performed without the transition model, the flow is assumed to be fully turbulent and the one equation Spalart-Allmaras and the two equation k-ω SST and EARSM models were employed. The gamma Reynolds theta transitional model (γ- Re_θ) is adopted together with the k-ω SST and the EARSM turbulent models. Additionally, a Hakimi preconditioning scheme is applied for all the simulations.

Figure 6.12 depicts the evolution of lift c_l and drag c_d coefficients with respect the angle of attack. It is apparent that numerical models have a good ability to predict the lift for moderate angles of attack, but overestimate the value for larger angles. Considering the drag prediction, the turbulence models including transition effect have proven to have a better prediction capability.

Comparisons between the predicted pressure coefficient c_p distribution along the aerofoil and experimental data are shown in Fig. 6.13. Two selected angles of attacks, 4.1 and 13.3°, are compared. A pressure overestimation is given on the suction side by the SA model for the 13.3° angle of attack, while the other two fully turbulent models provide a good agreement. For the 4.1° angle of attack, both transition models are able to predict accurately the laminar separation bubble located just aft of the mid-chord on the suction side of the aerofoil.

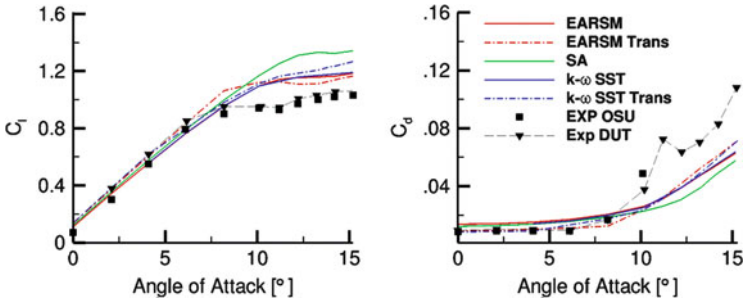

Fig. 6.12 Lift c_l and drag c_d coefficients versus angle of attack for S809 aerofoil

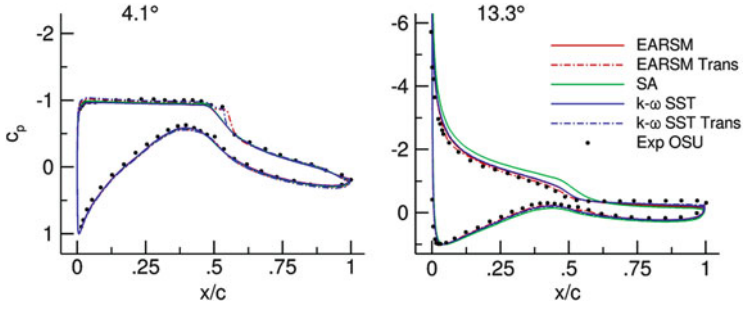

Fig. 6.13 Pressure coefficient c_p distributions for S809 aerofoil

The better prediction obtained with the 2 equation turbulent models compared to the 1 equation SA model, makes the former more adequate for the analysis of the complex flow structure developed inside the boundary layer when flow control devices are applied. Simulations for RVGs applied on blade are computationally demanding and only one turbulence model is selected for the further analysis.

The nonlinear constitutive relations of the EARSM model are capable of reproducing the anisotropy of the stress distribution—which is a very important feature beyond the possibilities of linear eddy viscosity turbulence models (SA, k-ω SST)—and makes this model even more suitable for the RVG implementation study.

6.5 The S809 Aerofoil (Flow Control Case)

6.5.1 Basic Configuration

Once the numerical methods have been favourably validated against experimental data for the NREL Phase VI wind turbine rotor and the S809 profile, the obtained results can be employed to the rod vortex generators design and optimization. In particular, the numerical predictions for the S809 aerofoil given by the fully turbulent EARSM model are employed for the dimensioning of the RVGs (h, D) and for the optimization of their chordwise location (x_{RVG}/c) and spanwise distribution (W). Table 6.2 summarizes the parameters of the basic RVG configuration.

Four flow cases are taken into consideration for flow control investigations. All of them are selected for high inflow angles: 11.2, 12.2, 13.3 and 13.9°, with the separation onset located at x/c = 0.88, 0.65, 0.55 and 0.53, respectively. As the angle of attack increases the separation moves upstream to the mid-chord in the case of the highest loading considered.

The case of the 13.9° inflow angle, where the most severe flow conditions exist, is taken as the reference and the rods are initially located slightly upstream of the separation onset ($x_{RVG}/c = 0.50$).

Boundary layer thickness is estimated based on the comparison of simulated velocity v and ideal velocity v_{id} profiles normal to the wall at a certain location.

Table 6.2 Parametric values for RVG

Parameter	Value
Pitch angle, θ [°]	45
Skew angle, α [°]	30
Height, h/δ [-]	0.36
Diameter, D/δ [-]	0.20
Spacing, W/D [-]	10

The ideal velocity profile can be obtained from the isentropic relation given in Eq. (6.2) for a constant total pressure P_0 (the value outside of the boundary layer):

$$v_{id} = \left[\left(\left(\frac{P_0}{P}\right)^{\frac{\gamma-1}{\gamma}} - 1\right) 2C_p T\right]^{1/2} \tag{6.2}$$

The boundary layer thickness, δ, is defined as the distance normal to the wall at which $v = 0.99 \cdot v_{id}$. In Eq. (6.2), T is static temperature and P is static pressure. Coefficient C_p is the heat capacity of the gas at constant pressure and γ the heat capacity ratio. The boundary layer thickness δ at the rod location for the reference case 13.9° amounts to $\delta \approx 0.0216 \cdot c$ and RVGs are scaled according to parameters established in Table 6.2.

Due to the small spacing among rods ($W \approx 0.043 \cdot c$) a large amount of them would be needed to cover the entire spanwise length of the experimental models employed by Somers (1997) and Ramsay et al. (1995). Besides, a large grid clustering is needed in the vicinities and downstream of the rod location in order to properly capture the development of streamwise vorticity. Additionally, the complexity of the model to be solved increases rapidly, and the computational resources needed for the full 3D configuration would be far beyond the available resources. Therefore, the 3D computational domain was limited to a slice of the original experimental model, inside which a single rod was placed and the periodic boundary conditions were applied in the spanwise direction, at lateral surfaces. The RVGs and aerofoil surface were modelled as walls (Fig. 6.14). The proximities of the RVG are resolved by means of a butterfly mesh topology.

The computational domain was divided into a total of 29 blocks. Full non matching boundary (FNMB) connections were applied, so the final number of mesh cells is 3.3×10^6. The NMB connections were applied at an approximate distance of $0.13 \cdot c$ from the aerofoil wall (Fig. 6.14).

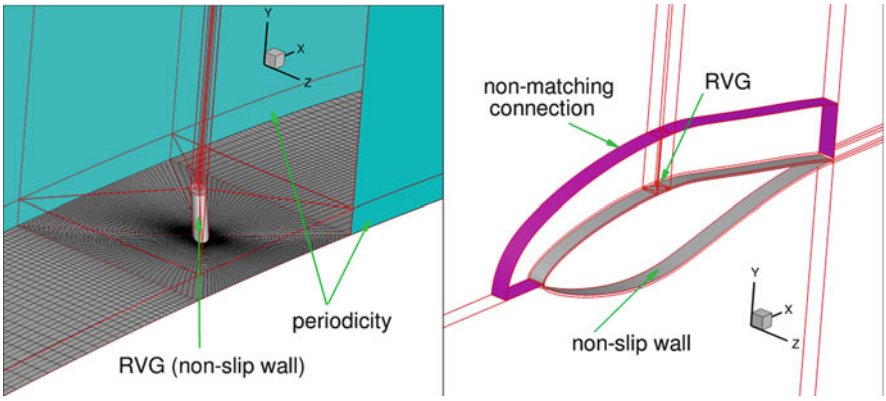

Fig. 6.14 Topology and boundary conditions for flow control case

In order to avoid the influence of grid nodes distribution in the streamwise direction for the case with and without RVG, the mesh employed for both cases is the same apart from the blocks with the RVG presence. Thus, the S809 aerofoil surface is defined by $737 \times 145 \times 33$ nodes in the wrap-around, normal and spanwise directions, respectively.

Lift c_l and drag c_d coefficients as a function of the angle of attack, obtained numerically for both cases (with and without RVG), are compared in Fig. 6.15. It is shown that for the selected flow cases the application of RVGs provides not only a higher lift force, but also leads to slight reduction of drag. The maximum improvement is observed for an angle of attack of 12.2°, where the lift coefficient c_l is increased by 5.2 % with respect to the clean case and drag is reduced by 1.2 % ($\Delta c_l = 5.2\%$, $\Delta c_d = -1.2\%$).

It is important to notice that the RVGs dimensions and spacing are kept constant at the defined location while the increasing inflow angle influences on boundary layer development, so the boundary layer thickness δ is not the same for all cases. Thus, for an angle of attack of 11.2° the ratio RVGs height to boundary layer thickness is approximately $h/\delta \approx 0.47$ ($\delta \approx 0.0165 \cdot c$) and for 12.2°, $h/\delta \approx 0.42$ ($\delta \approx 0.0185 \cdot c$), thus verifying the low profile VGs condition ($h/\delta < 0.65$) defined by Rao and Kariya (1988).

6.5.2 RVGs Chordwise Location

RVGs were initially located slightly upstream of the separation onset for an angle of attack of 13.9°, at the chordwise position $x_{RVG}/c = 0.50$, and designed according to the local boundary layer height using the parametric values summarized in Table 6.2. Notwithstanding the aerodynamic performance improvement obtained by implementing the RVGs at this location, it is prudent to conduct a study of the chordwise location effect on the devices' effectiveness. The flow control devices should be neither positioned too close to the separation (not enough space to develop vortical structures), nor too far away (vorticity diffusion). Four additional

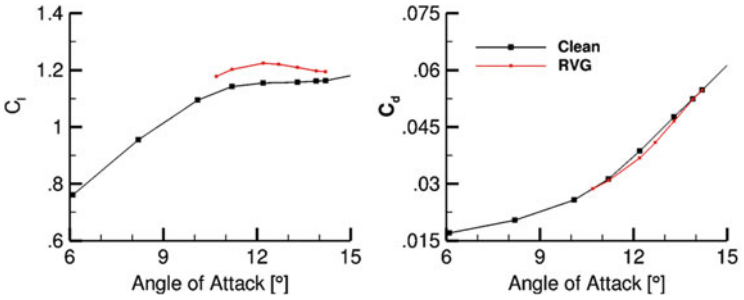

Fig. 6.15 Lift c_l and drag c_d coefficients vs angle of attack for clean and flow control cases

chordwise locations ($x_{RVG}/c = 0.35,\ 0.40,\ 0.45$ and 0.55) were considered and rods dimensioned in relation to the local boundary layer height at each one of the four chordwise locations for a 13.9° inflow angle. The spacing between rods (W) was kept the same as for the initial configuration. The number of grid nodes and spacing was also preserved—except in the region of the device location, where the refinement is adjusted in order to diminish the grid influence.

A comparison was done for four angles of attack 11.2, 12.2, 13.3 and 13.9°. As mentioned above, increasing the inflow angle from 11.2 to 13.9° enforces earlier separation, so flow control devices should be located further upstream in order to improve aerofoil performance.

Lift c_l and drag c_d variations for the considered RVG locations and inflow angles, in respect to the case without flow control, are shown in Fig. 6.16. The values indicate configurations for which the positive or negative effect is obtained. It can be observed that a lift increase is obtained for all locations and inflow angles, except for the angle of attack 13.9° and $x_{RVG}/c = 0.55$, where RVG is located inside the separation bubble. A reduction of drag is obtained for certain rods locations and angles of attack. However, the configuration of maximum lift increase corresponds with the area of drag reduction, leading to aerodynamic improvement.

When the angle of attack is 11.2°, the maximum lift is for RVGs located at $x_{RVG}/c = 0.55$. The lift decreases as these are moved closer to the leading edge. Simultaneously, as the RVG location is moved upstream, the drag increases. This means that even if the higher vorticity is created by the RVG located further upstream, the streamwise vortices would dissipate faster than if they were located closer to separation.

A similar effect to the one analysed above is obtained for an inflow angle of 12.2°. The maximum improvement in aerodynamic performance by the implementation of flow control devices is obtained for $x_{RVG}/c = 0.50$.

As the angle of attack increases to 13.3° the separation line moves to $x/c = 0.55$ and the optimum RVG placement is at the mid-chord. Further upstream locations provide smaller increases in lift (vortices are more dissipated) and higher drag. For

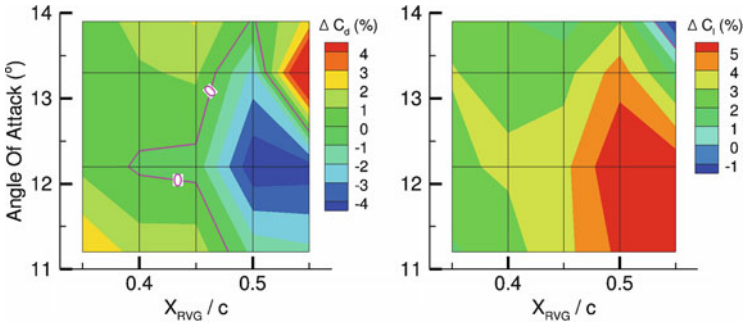

Fig. 6.16 Effect of RVGs chordwise location x_{RVG}/c on c_l and c_d coefficients

$x_{RVG}/c = 0.55$, the lack of distance to the separation onset impedes the development of the vortex structure and results in a high drag penalty.

Further increasing of the angle of attack up to 13.9°, leads to a more modest profit with the RVG inclusion. The RVGs located at $x_{RVG}/c = 0.55$ show a negative effect on the aerodynamic performance—which is expected since the devices are located inside the region of detached flow (separation onset is at $x/c = 0.53$). At this inflow angle only RVGs located at mid-chord provide a drag reduction.

Based on the contour map analysis, one can conclude that for the selected spanwise distance, W $\approx 0.043 \cdot c$, the optimum RVG location is at mid-chord, $x_{RVG}/c = 0.50$.

6.5.3 RVGs Spanwise Separation

Experimental investigations were conducted to assess the effectiveness of RVGs by varying different parameters; based on the results of these experimental investigations, it was found that the most effective spanwise distance (W) to rod diameter (D) ratio is equal to 10. Consequently, this spanwise distance was used together with the other parameters summarized in Table 6.2 for the initial RVG design. However, due to another flow conditions investigated in the presented chapter, the four RVG spacing scenarios ($W/D = 7.5,\ 10,\ 15$ and 20) are analysed in order to determine a possible influence on separation. The remaining parameters are kept unchanged. Grid influence was minimised by keeping the same number of nodes—except in the spanwise direction, where the number of cells was adjusted according to the increased spanwise distance.

In Fig. 6.17, contour maps of skin friction coefficient c_f on the suction side of the S809 aerofoil, at the angle of attack 11.2°, are shown. The case without RVG is shown at the top; below, the cases for rising RVG spanwise distance are compared. The skin friction provides information on the shear stresses distribution and the presence of separation. Additionally, streamlines displayed on top of the skin friction contours allow one to assess the development of flow patterns on the aerofoil. In the presented flow control cases, RVGs were located at the optimum chordwise position previously identified (Sect. 6.5.2): $x_{RVG}/c = 0.50$.

It is clearly visible in Fig. 6.17 that skin friction along the chord increases downstream of the RVGs' location and it is higher than in the case of "uncontrolled" flow. Narrow regions of lower friction are present in the zones between rods. This structure is originated by the streamwise vortices. The convected vortices transport momentum from the outer region of the boundary layer to the layer closer to the wall on one vortex side, while lifting the boundary layer on the opposite one.

Assuming a spanwise distance equal to 10 rod diameters (reference configuration), the region of detached flow existing in the clean case vanishes and shrunken backflow zones appear between RVGs at around 75 % of the chord. It is also clearly visible that a spanwise velocity component is generated by the RVGs, rooted in the spanwise migration of the created vortices.

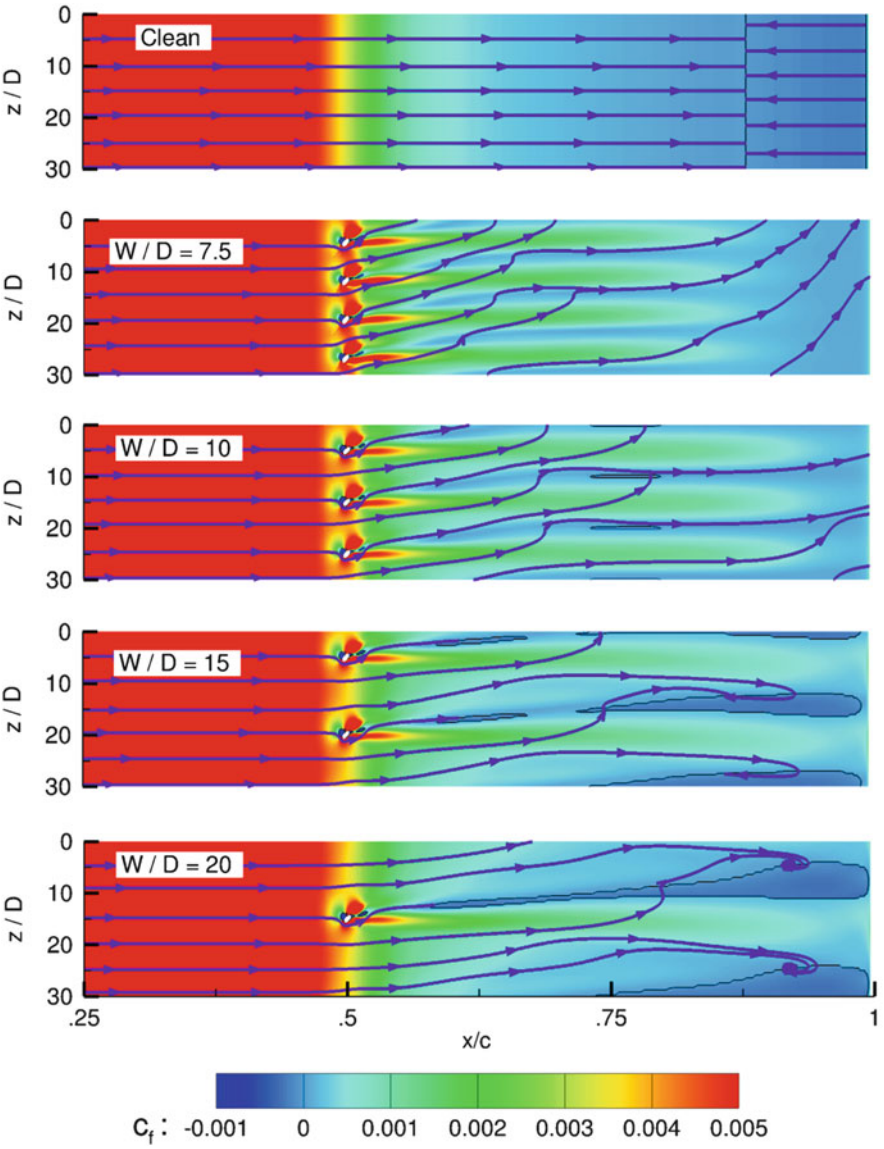

Fig. 6.17 Skin friction coefficient c_f and surface streamlines for different RVGs spanwise distance ***W/D***

When the distance is decreased to 7.5 diameters, the small separation bubbles between streamwise vortices vanished and no detached flow is noticed. Notwithstanding this fact, the skin friction contour map reveals that the penetration of the streamwise vorticity has been shortened in comparison with the reference configuration ($10 \cdot D$). Consequently, a possible interaction of streamwise vortices

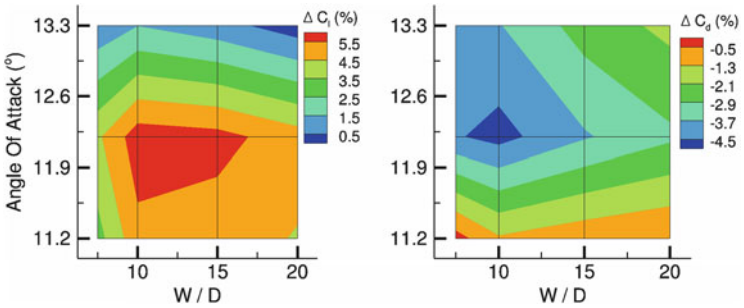

Fig. 6.18 Effect of RVGs spanwise separation **W/D** in $\mathbf{c_l}$ and $\mathbf{c_d}$ coefficients

appeared in the flow for a distance $7.5 \cdot D$ which could decrease the RVG effectiveness.

As the separation between rods increases from the reference to 15 diameters, the length and width of the backflow bubbles located between rods also increases. The separation onset is moved upstream to 70 % of the chord. Furthermore, for this RVG configuration, the trailing edge separation was only partially eliminated and the elongated regions of detached flow in the proximities of the trailing edge still exist. For a further rods spacing increase to $20{\cdot}D$, one can observe that the previously described backflow bubbles have merged into a long recirculation region. In any case, the global separated area is still lower compared to a case without RVG.

In Fig. 6.18, the contourmaps of lift c_l and drag c_d variations with respect to the clean case for RVGs at chordwise location $x_{RVG}/c = 0.5$ are presented. It is clearly shown that for an angle of attack of 11.2° a separation of 7.5 rod diameters provides the minimum drag reduction and lift increase, which strengthen the previous hypothesis of interaction between streamwise vortices. Spanwise distances of $10 \cdot D$ and $15 \cdot D$ provide the highest increases of lift coefficient for all angles of attack. However, the implementation of a spanwise distance $10 \cdot D$ allows for further decrease of the drag in the studied angles of attack. At 13.3° the separation has moves upstream to x/c = 0.55 and the decay of maximum streamwise vorticity in chordwise direction is more intensive than for lower angles of attack. Nevertheless, aerodynamic improvement obtained by means of implemented RVG is still positive, although the global extremum is found for $W = 10 \cdot D$.

6.6 Conclusions

The numerical simulations carried out for NREL Phase VI rotor configurations indicated a good agreement of obtained results with experimental data. This validated the model, and proved its capability to predict aerodynamic performance. Hence, the validated model was used to investigate rod vortex generators as a means of improving aerodynamic performance. The effect of RVGs and generated

streamwise vortices on the separation reduction was analysed on a S809 aerofoil. Numerical simulations for a blade section defined by the S809 aerofoil were also validated by experimental data, and the results were considered as the reference case for the flow control analysis. A study was conducted to analyse the effect of varying the location and spanwise direction of rod vortex generators: the subsequent numerical results confirmed the effectiveness of RVGs as a means of flow separation reduction and increasing aerodynamic performance.

Acknowledgments The authors would like to acknowledge the European Commission for their research grant under the project FP7-PEOPLE-2012-ITN 309395 "MARE-WINT" (new MAterials and REliability in offshore WINDd Turbines technology). The research was supported in part by the PL-Grid Infrastructure and TASK Supercomputing Centre in Gdansk.

References

Amitay M, Smith BL, Glezer A (1998) Aerodynamic flow control using synthetic jet technology. In: Abstracts of the 36th AIAA aerospace sciences meeting exhibit, Reno, 12–15 January 1998

Andersen PB, Henriksen L, Gaunaa M et al (2010) Deformable trailing edge flaps for modern megawatt wind turbine controllers using strain gauge sensors. Wind Energy 13:193–206

Bak C, Bitsche R, Yde A et al (2012) Light rotor: the 10-MW reference wind turbine. Paper presented at the EWEA 2012 – European wind energy conference and exhibition, Copenhagen, 16–19 April 2012

Choi YH, Merkle CL (1993) The application of preconditioning in viscous flows. J Comput Phys 105(2):207–223

Doerffer P, Flaszyski P, Szwaba R (2009) Rod patent. Poland patent PL38968

Eppler R, Somers DM (1980) A computer program for the design and analysis of low-speed airfoils. In: NASA Technical Reports. Available via NASA Technical Reports Server (NTRS) http://hdl.handle.net/2060/19810005410. Accessed 07 Apr 2016

Gao L, Zhang H, Liu Y et al (2015) Effects of vortex generators on a blunt trailing-edge airfoil for wind turbines. Renew Eneryg 76:303–311

Hakimi N (1997) Preconditioning methods for time dependent Navier-Stokes equations: application to environmental and low speed flows. Dissertation, Vrije Universiteit

Hand MM, Simms DA, Fingersh L et al (2001) Unsteady aerodynamics experiment phase VI: wind tunnel test configurations and available data campaigns: NREL/TP-500-29955. In: National Renewable Energy Laboratory (NREL) Publications. Available via NREL. http://www.nrel.gov/docs/fy02osti/29955.pdf. Accessed 06 Apr 2016

Jameson A (1991) Time dependent calculations using multigrid, with applications to unsteady flows past airfoils and wings. In: Abstracts of the 10th computational fluid dynamics conference, fluid dynamics and co-located conferences, AIAA, Honolulu, 24–26 June 1991

Johnson SJ, Baker JP, Van Dam CP et al (2010) An overview of active load control techniques for wind turbines with an emphasis on microtabs. Wind Energy 13:239–253

Kostas J, Foucaut JM, Stanislas M (2007) The flow structure produced by pulsed-jet vortex generators in a turbulent boundary layer in an adverse pressure gradient. Flow Turbul Combust 78:331–363

Lin JC (2002) Review of research on low-profile vortex generators to control boundary-layer separation. Prog Aerosp Sci 38:389–420

Lindenburg C (2003) Investigation into rotor blade aerodynamics: analysis of the stationary measurements on the UAE phase-VI rotor in the NASA-AMES wind tunnel ECN-C–03-025. In: Energy Research Centre of the Netherlands (ECN) Publications. Available via ECN. https://www.ecn.nl/publications/PdfFetch.aspx?nr=ECN-C--03-025. Accessed 07 Apr 2016

Martinez J, Doerffer P, Szulc O et al (2015a) Aerodynamic analysis of wind turbine rotor blades. Task Q 19(2):129–140

Martinez J, Doerffer P, Szulc O (2015b) CFD validated technique for prediction of aerodynamic characteristics on horizontal axis wind energy turbines. Poster presented at the Offshore 2015 Conference, The European Wind Energy Association, Copenhagen, 10–12 March 2015

McManus K, Legner HH, Davis SJ (1994) Pulsed vortex generator jets for active control of flow separation. In: Abstracts of the fluid dynamics conference, AIAA, Colorado Springs, 20–23 June 1994

Menter FR (1994) Two-equation eddy-viscosity turbulence models for engineering applications. AIAA J 32(8):1598–1605

Menter FR, Garbaruk AV, Egorov Y (2012) Explicit algebraic Reynolds stress models for anisotropic wall-bounded flows. Prog Flight Phys 3:89–104

Nelson RC, Corke TC, Othman H (2008) A smart wind turbine blade using distributed plasma actuators for improved performance. In: Abstracts of the 46th AIAA aerospace sciences meeting and exhibit, Reno, 7–10 January 2008

Paul AR, Joshi S, Jindal A et al (2013). Comparison active-passive: experimental studies of active and passive flow control techniques applied in a twin air-intake. Sci World J. doi:10.1155/2013/523759

Ramsay RR, Hoffman MJ, Gregorek GM (1995) Effects of grit roughness and pitch oscillations on the S809 airfoil NREL/TP-442-7817. In: National Renewable Energy Laboratory Reports. Available via NREL. https://wind.nrel.gov/airfoils/OSU_data/reports/3x5/s809.pdf. Accessed 07 Apr 2016

Rao DM, Kariya TT (1988) Boundary-layer submerged vortex generators for separation control-an exploratory study. In: Abstracts of the 1st national fluid dynamics conference, AIAA, Cincinnati, 25–28 July 1988

Somers DM (1997) Design and experimental results for the S809 airfoil NREL/SR-440-6918. NREL Report: In: National Renewable Energy Laboratory Reports. Available via NREL. www.nrel.gov/docs/legosti/old/6918.pd. Accessed 07 Apr 2016

Sørensen NN, Michelsen JA (2000) NREL/NWTC aerodynamics code blind comparison. In: Abstracts of the 2 science panel meeting, NREL Boulder, Colorado, 5–6 December 2000

Spalart PR, Allmaras SR (1992) A one-equation turbulence model for aerodynamic flows. In: Abstracts of the 30th AIAA aerospace sciences meeting and exhibit, AIAA, Reno, 6–9 January 1992

Sutherland W (1893) LII. The viscosity of gases and molecular force. Philos Mag Ser 5 36(223):507–531

Taylor HD (1947) The elimination of diffuser separation by vortex generators. United Aircraft Corporation Research Department Report No. R-4012-3

Tejero F, Doerffer P, Szulc O (2015) Shock wave induced flow separation control by air-jet and rod vortex generators. Task Q 19(2):167–180

van Dam CP, Chow R, Zayas JR et al (2007) Computational investigations of small deploying tabs and flaps for aerodynamic load control. J Phys Conf Ser. doi:10.1088/1742-6596/75/1/012027

van Dam CP, Berg DE, Johnson SJ (2008) Active load control techniques for wind turbines. In: Department of Energy Scientific and Technical Information (OSTI). Available via OSTI. http://www.osti.gov/scitech/servlets/purl/943932. Accessed 07 Apr 2016

Wagner S, Bareiss R, Guidati G (eds) (2012) Wind turbine noise. Springer, Berlin

Wallis RA, Stuart CM (1962) On the control of shock induced boundary layer separation with discrete air jets. In: National Advisory Committee for Aeronautics (NACA) Archives. Available via NACA. http://naca.central.cranfield.ac.uk/reports/arc/cp/0595.pdf. Accessed 07 Apr 2016

Wiltse JM, Glezer A (1993) Manipulation of free shear flows using piezoelectric actuators. J Fluid Mech 249:261–285

Chapter 7
Trailing and Leading Edge Flaps for Load Alleviation and Structure Control

Vladimir Leble and George N. Barakos

Abstract This chapter presents the results of numerical computations for a 10-MW wind turbine rotor equipped with the trailing and leading edge flaps. The aerodynamic loads on the rotor are computed using the Helicopter Multi-Block flow solver. The method solves the Navier-Stokes equations in integral form using the arbitrary Lagrangian-Eulerian formulation for time-dependent domains with moving boundaries. The trailing edge flap was located at 75%R, and the leading edge flap was located at 60%R, where R is the radius of the blade. The chapter is divided in the description of employed numerical methods, mesh convergence study, and the cases with trailing and leading edge flaps. Also, the chapter defines flap geometry, deformation and frequency of motion. The blade structure was assumed rigid for all presented cases. The comparison of the flap performance is conducted using non-dimensional parameters, and conclusions are drawn at the end of the chapter.

7.1 Numerical Methods

The HMB3 code is a 3D multi-block structured solver for the 3D Navier-Stokes equations. HMB3 solves the Navier-Stokes equations in integral form using the arbitrary Lagrangian-Eulerian formulation for time-dependent domains with moving boundaries. The solver uses a cell-centred finite volume approach combined with an implicit dual-time method. Osher's upwind scheme (Osher and Chakravarthy 1983) is used to resolve the convective fluxes, and MUSCL (Van Leer 1979) variable extrapolation is used to provide formally third-order accuracy on uniform grids. Central differencing (CD) spatial discretisation is used for the viscous terms. The non-linear system of equations that is generated as a result of the linearization is solved by integration in pseudo-time using a first-order backward difference method based on Jameson's pseudo-time integration approach (Jameson 1991). A Generalised Conjugate Gradient (GCG) method is then used (Eisenstat et al. 1983)

V. Leble • G.N. Barakos (✉)
Division of Aerospace Sciences, School of Engineering, University of Glasgow, James Watt South Building, Glasgow G12 8QQ, UK
e-mail: v.leble.1@research.gla.ac.uk; George.Barakos@glasgow.ac.uk

W. Ostachowicz et al. (eds.), *MARE-WINT*, DOI 10.1007/978-3-319-39095-6_7

in conjunction with a Block Incomplete Lower-Upper (BILU) factorisation as a preconditioner. The HMB3 solver has a library of turbulence closures including several one- and two- equation models. Turbulence simulation is also possible using either the Large-Eddy or the Detached-Eddy simulation approach (Spalart et al. 1997). The solver was designed with parallel execution in mind and the MPI library along with a load-balancing algorithm are used to this end. The flow solver can be used in serial or parallel fashion for large-scale problems. Depending on the purposes of the simulations, steady and unsteady wind turbine CFD simulations can be performed in HMB3 using single or full rotor meshes generated using the ICEM-Hexa tool. Rigid or elastic blades can be simulated using static or dynamic computations. HMB3 allows for sliding meshes to simulate rotor-tower interaction (Steijl and Barakos 2008). Alternatively, overset grids can be used (Jarkowski et al. 2013). To account for low-speed flows, the Low-Mach Roe scheme (LM-Roe) developed by (Rieper 2011) is employed for wind turbine cases (Carrión et al. 2013).

The HMB3 CFD solver has so far been validated for several wind turbine cases, including the NREL Annex XX experiments (Gómez-Iradi et al. 2009), where the effect of the blades passing in front of the tower was captured. The pressure and PIV data of the MEXICO project (Carrión et al. 2014) have also been used for validation, where the wake was resolved on a fine mesh capable to capture and preserve the vortices downstream the rotor, which enabled the prediction of the onset of wake instabilities (Carrión et al. 2015).

A new flap deflection algorithm was implemented in HMB3 to allow for arbitrary flap motion. The algorithm is based on the surface interpolation, where the mean, maximum, and minimum flap deflections are defined by separate surfaces. Then, the linear interpolation is employed for each point on the surface between the mean and deflected shape of the flap. The motion of the flap can be a complex function of time i.e. not a simple function like $sin(\omega t)$ or $cos(\omega t)$. In this case the motion is described by a Fourier series of arbitrary number of harmonics. It must be noted here, that since only mean and maximum surfaces are known to the solver, the interpolation tends to shrink the flap slightly. To understand this behaviour, consider a 2D rod-like flap shown in Fig. 7.1. As can be seen, the linear interpolation tends to shrink the flap, but the effect is not pronounced for relatively small angles of deflection.

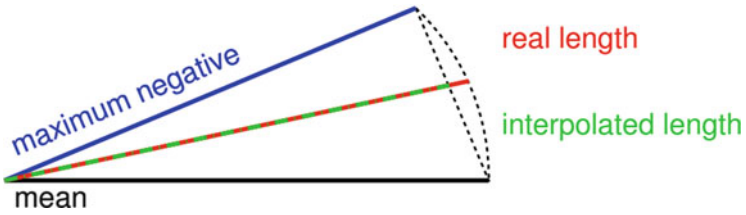

Fig. 7.1 Schematic of the trailing edge flap, showing mean and maximum negative deflections, and real and interpolated length of the flap during motion

The computational mesh is updated at each time step after the deformation of the surface. The Trans-Finite Interpolation (TFI), described by Dubuc et al. (2000), is applied to the blocks attached to the deformed surface. The TFI interpolates the block face deformation from the edge deformations and then the full block deformation from the deformation of the block faces. The grid deformation uses a weighted approach to interpolate a face/block from the boundary vertices/surfaces respectively. The weight depends on the curvilinear coordinate divided by the length of the curve.

7.2 Numerical Parameters

This work employed the DTU 10 MW reference wind turbine design of Bak et al. (2013). For all presented cases, the density of air was assumed to be $\rho = 1.225$ kg/m^3, the dynamic viscosity of the air was $\mu = 1.8 \times 10^{-5}$ N s/m^2, and the speed of sound was 340 m/s. Further, a fully turbulent flow was assumed with free-stream level of turbulence of 2.6 % and uniform inflow velocity distribution was set across the inflow boundary. The k-ω SST turbulence model was employed for all tests, unless otherwise stated. The y^+ parameter was estimated based on the flat-plate boundary layer theory. For given Reynolds number, inflow velocity U_∞, density ρ, dynamic viscosity μ and cord length c the y^+ parameter was computed in the following steps:

1 Estimate the skin friction coefficient from Schlichting's correlation:

$$C_f = [2 \cdot log_{10}(Re) - 0.65]^{-2.3} \tag{7.1}$$

2 Obtain the wall shear stress from the definition of C_f:

$$\tau_w = C_f \cdot 0.5 \cdot \rho \cdot U_\infty^2 \tag{7.2}$$

3 Compute the friction velocity from:

$$U_* = \sqrt{\tau_w / \rho} \tag{7.3}$$

4 Compute the y^+ parameter from the definition, where y is the employed spacing next to the wall:

$$y+ = y \cdot \rho \cdot U_* / \mu \tag{7.4}$$

For the presented cases with trailing and leading edge flaps, the inflow wind speed was set to 11.4 m/s, and the rotational speed of the rotor was set to 9.6 rpm, giving a tip speed ratio of 7.83.

7.3 Mesh Convergence Study

The mesh convergence study was performed before various test cases were computed to find the required density of the mesh and cell distribution in the vicinity of the blade surface. Only 70 % of the blade was modelled for this study—from 0.3R to 1R, where R is the radius of the blade. The flow around the blade was considered to be periodic in space and time. This allowed the use of the HMB3 "hover" formulation described by Steijl et al. (2006). The formulation includes a combination of mesh motion and additional source terms in the Navier-Stokes equations. The spinner was approximated with a long cylinder running parallel to the flow along the computational domain. The free-stream was kept to the level of turbulence of 2.6 %, and the k-ω turbulence model was employed. The conditions selected for the mesh convergence study are presented in Table 7.1. The domain size and boundaries are shown in Fig. 7.2, and the results of the mesh convergence study are presented in Fig. 7.3. This study showed that a mesh density between 3 and 5 M cells per blade is sufficient to obtain mesh independent solutions.

Table 7.1 Computational conditions for the mesh convergence study

Parameter	Value
U_{wind}	11 m/s
U_{tip}	82.437 m/s
RPM	8.836
Re_{tip}	$34.817° \times °10^6$
$M_{tip} = U_{tip}/U_{sound}$	0.243
λ	7.494
Pitch angle	0°

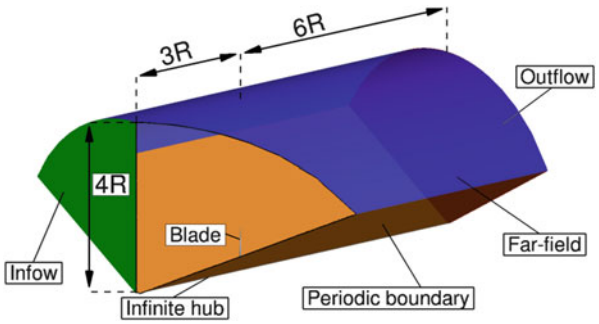

Fig. 7.2 Computational domain for mesh convergence study with employed boundary conditions. Part of the domain removed to expose the blade

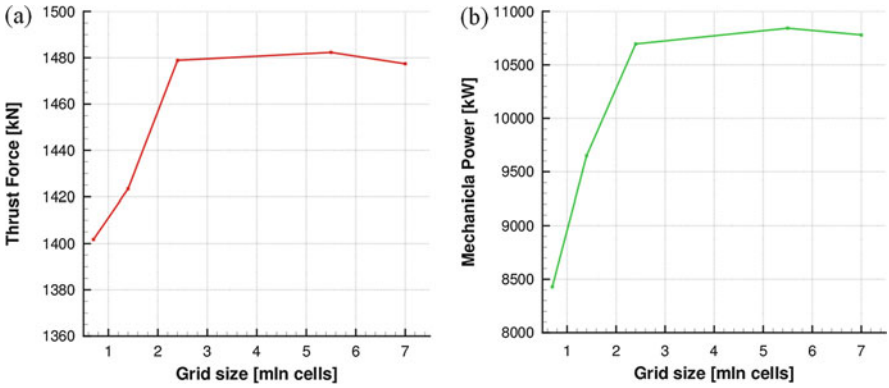

Fig. 7.3 Thrust force (**a**) and mechanical power (**b**) as function of computational grid density

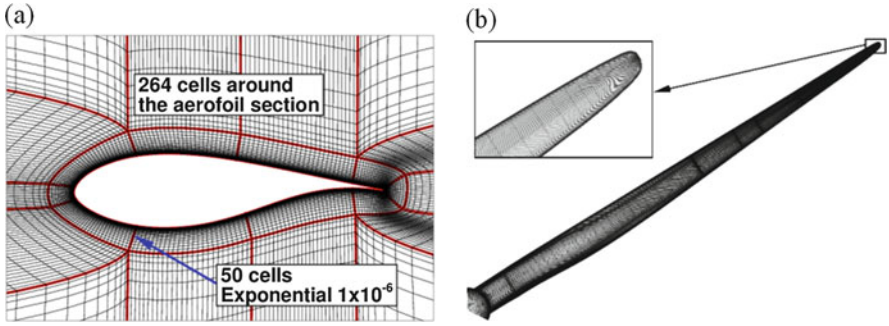

Fig. 7.4 Slices through the mesh near the surface of the blade (**a**); and surface grids (**b**) for the 9.2 M cell grid

7.4 Computational Grid

Based on the mesh study, a fine mesh consisting of 9.2 M points was constructed and included the necessary refinement to allow for the flaps. The computational domain had the same dimensions as for the grid convergence study shown in Fig. 7.2. The grid included the complete DTU 10 MW RWT blade in a straight configuration (no pre-bending or pre-coning), and employed an O-grid topology around the aerofoil sections, as shown in Fig. 7.4a. The first cell wall distance was $10^{-6}c$, where $c = 6.206\ m$ is a maximum chord of the blade. The y^+ parameter for this gird at rated conditions was 0.2. Figure 7.4b shows the surface grid on the blade for the 9.2 M cells grid.

The blade was modelled in a straight configuration with a simplified nacelle, as shown in Fig. 7.5. The simplified nacelle shape was obtained by rotating the hub of the rotor by 180°.

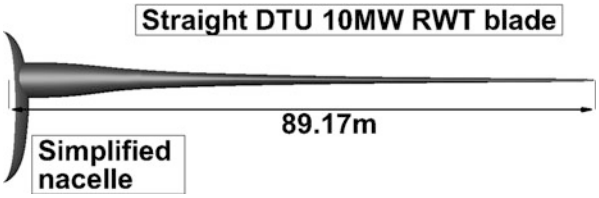

Fig. 7.5 Shape of the DTU 10 MW RWT blade with simplified nacelle as employed for the 9.2 M cells mesh

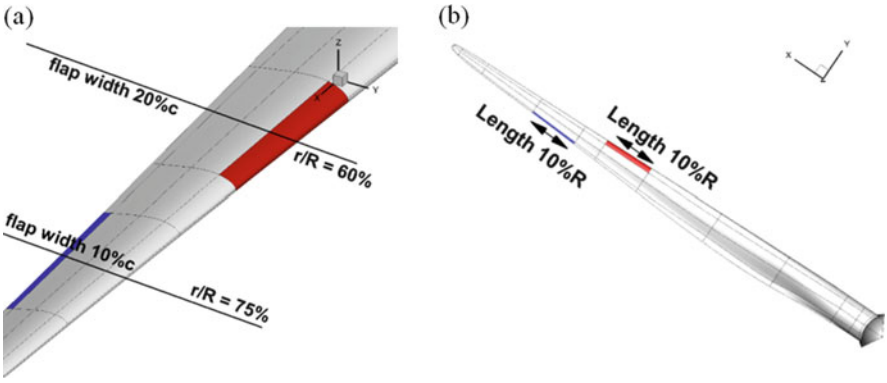

Fig. 7.6 The location and dimensions of the trailing and leading edge flaps. (**a**) Location and width of the flaps. (**b**) Length of the flaps

7.5 Definition of the Flaps

The DTU 10-MW RWT blade was equipped with leading and trailing edge flaps. The leading edge (LE) flap was located at 60%R station, and the trailing edge (TE) flap was located at 75%R. The length of each flap was 10%R, but the width of the TE flap was 10 % of the local chord, whereas the width of the LE flap was 20 % of the local chord, as shown in Fig. 7.6a, b. The choice of the TE flap width was made under the understanding that flaps will be used for load control and elevation. For the LE flap, it was assumed that its operation is similar but less efficient to that of the TE flap. The width in this case is increased to 20 % so as to allow larger control surface and a smooth transition of the surface slope.

The deformation of the flaps was defined with respect to the mean line of the aerofoils as indicated in Fig. 7.7. The deformation of the mean line was defined by the shape function $\eta(\xi) = \alpha\xi^2(3-\xi)/2$, where $\xi \in [0,1]$ and depends on the location of the deformed point x, and α is providing the maximum deflection for given time instance. For the trailing edge flap $\xi^{TE} = \left(x/c - x_0^{TE}\right) / \left(1 - x_0^{TE}\right)$, and for the leading edge flap $\xi^{LE} = \left(x_0^{LE} - x/c\right) / \left(x_0^{LE}\right)$, where x_0^{TE} and x_0^{LE} are the x/c locations of the hinge point for the trailing and leading edge flap, respectively; and

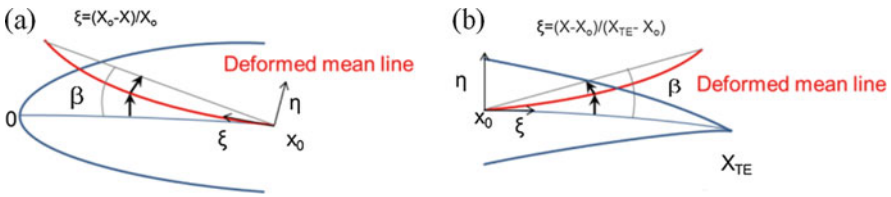

Fig. 7.7 Definition conditions for the LE (**a**) and TE (**b**) flap deformation

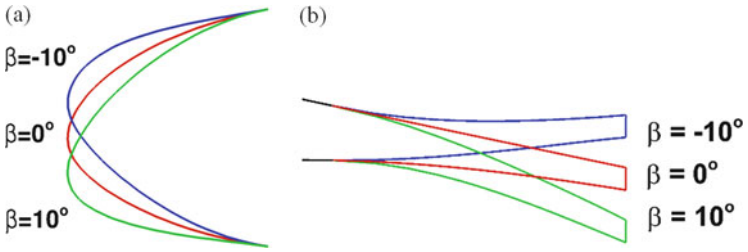

Fig. 7.8 Definition of the positive and negative deflection for the LE (**a**) and TE (**b**) flap

c is the local chord. From the equation for the shape function it follow that $\eta(\xi) \in [0, \alpha]$. In principle, $\alpha \equiv \alpha(t) = \alpha_m \sin(\omega t)$, where α_m. is the maximum value of deflection determined by the maximum deflection angle β. Here, the maximum deflection was obtained as $\alpha_m^{TE} = \left(1 - x_0^{TE}\right) \tan(\beta)$ and $\alpha_m^{LE} = \left(x_0^{LE}\right) \tan(\beta)$ for trailing and leading edge flap, respectively. By denoting the point at which the flap starts with x_0, the process to compute flap deflection is as follows: For each point $x > x_0$, define $\xi = \xi(x)$ based on the length along the chord line; compute point displacement α based on the maximum deflection angle β and time t; compute shape function $\eta(\xi)$; apply shape function and obtain deformed flap shape.

The flaps were deflected form $-10°$ to $10°$ with the shape and notation presented in Fig. 7.8. The frequency of flap motion was set to 0.96 Hz, or six times per revolution.

7.6 Results for the TE Flap

Span-wise load distributions for the DTU 10-MW reference wind turbine equipped with the trailing edge flap are shown in Fig. 7.9. The Flap oscillates at frequency 0.96 Hz—six times per revolution. The length of each section in radial direction used in pressure integration is $\Delta r = 2.15m$.

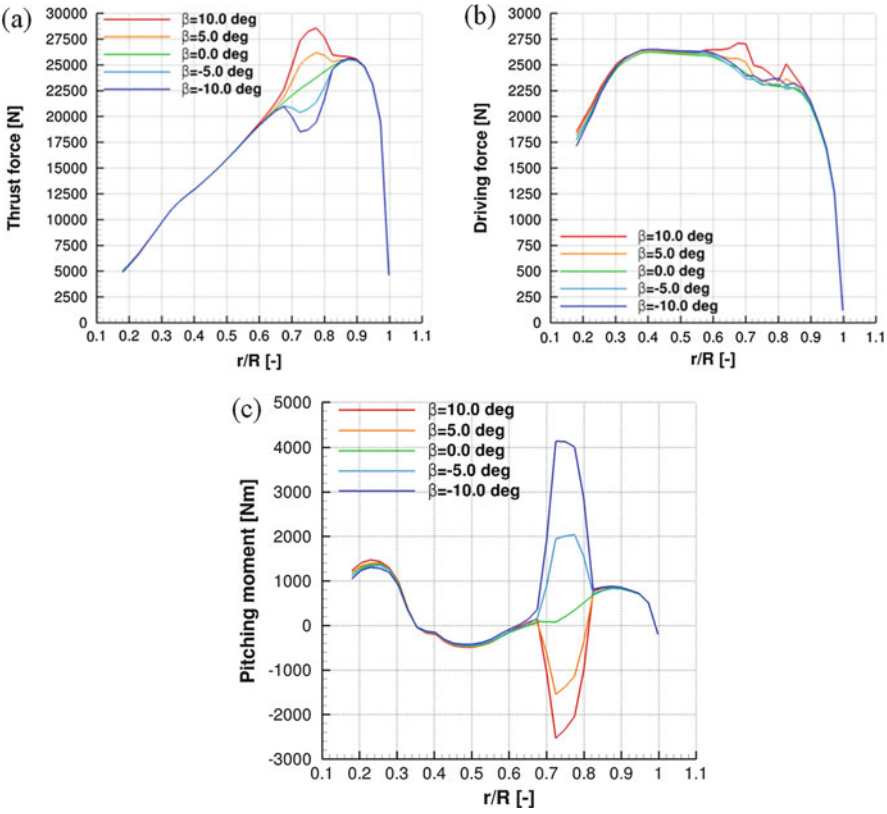

Fig. 7.9 Spanwise distribution of thrust force (**a**), driving force (**b**) and pitching moment (**c**) for DTU blade equipped with TE flap. Flap motion frequency f = 0.96 Hz (6 times per revolution)

7.7 Results for the LE Flap

Span-wise load distributions for the DTU 10-MW reference wind turbine equipped with the leading edge flap are shown in Fig. 7.10. Flap oscillates at frequency 0.96 Hz—six times per revolution. The length of each section in radial direction used in pressure integration is $\Delta r = 2.15m$.

7.8 Comparison of the Performance

In order to conduct a meaningful comparison of the performance of both flaps the non-dimensional coefficients were used. This was chosen, since flaps are located at different radial positions and have different inflow conditions. For this, the normal

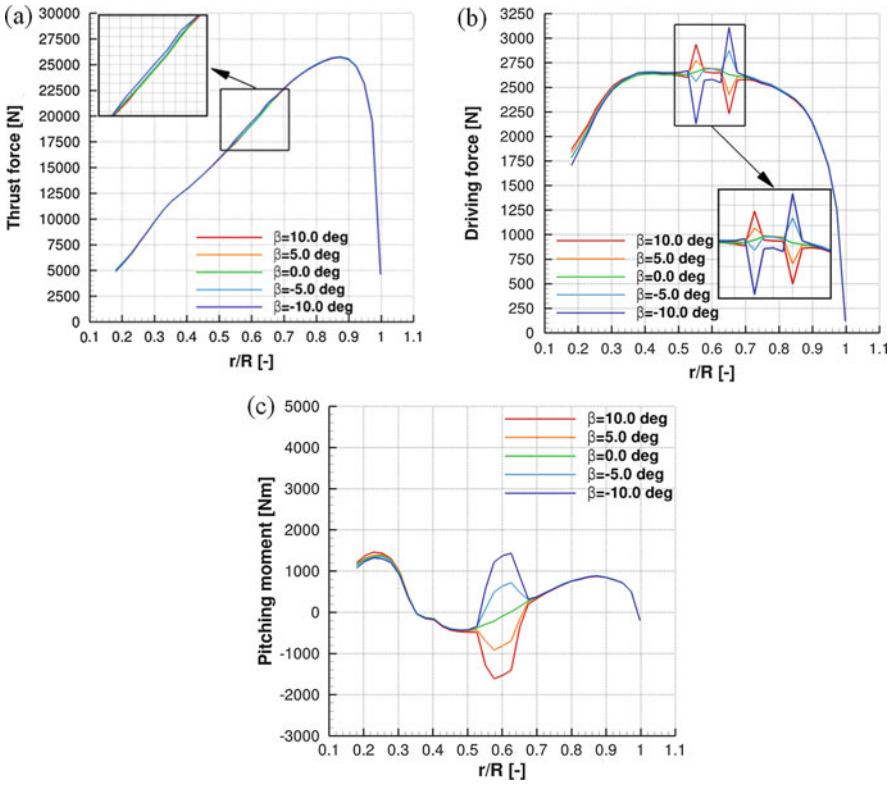

Fig. 7.10 Spanwise distribution of thrust force (**a**), driving force (**b**) and pitching moment (**c**) for DTU blade equipped with LE flap. Flap motion frequency f = 0.96 Hz (6 times per revolution)

force coefficient (CN), tangential force coefficient (CT) and pitching moment coefficient (CM) were computed. First, the thrust and driving forces were projected on the normal and tangential directions using local geometrical pitch angle α as:

$$F_N = T_F \cdot \cos(\alpha) + D_F \cdot \sin(\alpha) \tag{7.5}$$

$$F_T = D_F \cdot \cos(\alpha) - T_F \cdot \sin(\alpha) \tag{7.6}$$

The thrust (T_F) and driving (D_F) forces are defined in Fig. 7.11, and were obtained from the surface pressure integration in the middle of the flap with the length of the section in radial direction $\Delta r = 2.15m$. Note, that the geometrical pitch angle α is defined in Bak et al. (2013), and is constant i.e. it does not change

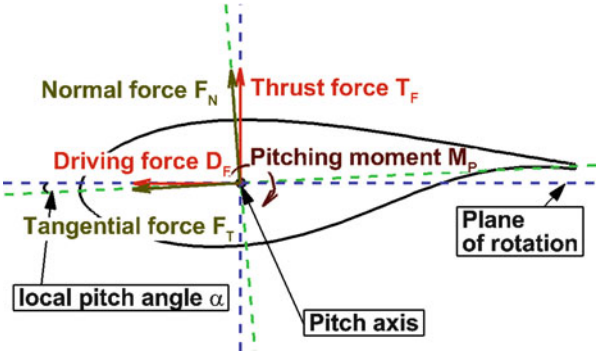

Fig. 7.11 Definition of the normal force, tangential force and pitching moment. Quantities shown in the directions defined as positive

with the flap angle β. Then, the forces and moment were non-dimensionalized as:

$$CN = \frac{F_N}{0.5\rho U^2 A} \tag{7.7}$$

$$CT = \frac{F_T}{0.5\rho U^2 A} \tag{7.8}$$

$$CM = \frac{M_P}{0.5\rho U^2 A c} \tag{7.9}$$

where U and A are the geometrical local inflow velocity and the local platform area, respectively. The inflow velocity is defined as:

$$U^2 = (\Omega r)^2 + U_{wind}^2 \tag{7.10}$$

and the platform area is defined as:

$$A = \Delta r \cdot c \tag{7.11}$$

where c is the local chord in the middle of the flap.

The obtained coefficients for both flaps as functions of the flap angle β are compared in Fig. 7.12. As can be seen, the trailing edge flap significantly modifies all three non-dimensional coefficients. On the other hand, leading edge flap has the most pronounced effect on the pitching moment coefficient, and almost negligible (as compared to the TE flap) influence on the normal force coefficient. Further, the relative change and slope of the pitching moment coefficient is higher for the trailing edge flap. Finally, both flaps can change the tangential force coefficient, but the TE flap has higher hysteresis loop, as compared to the results for the LE flap.

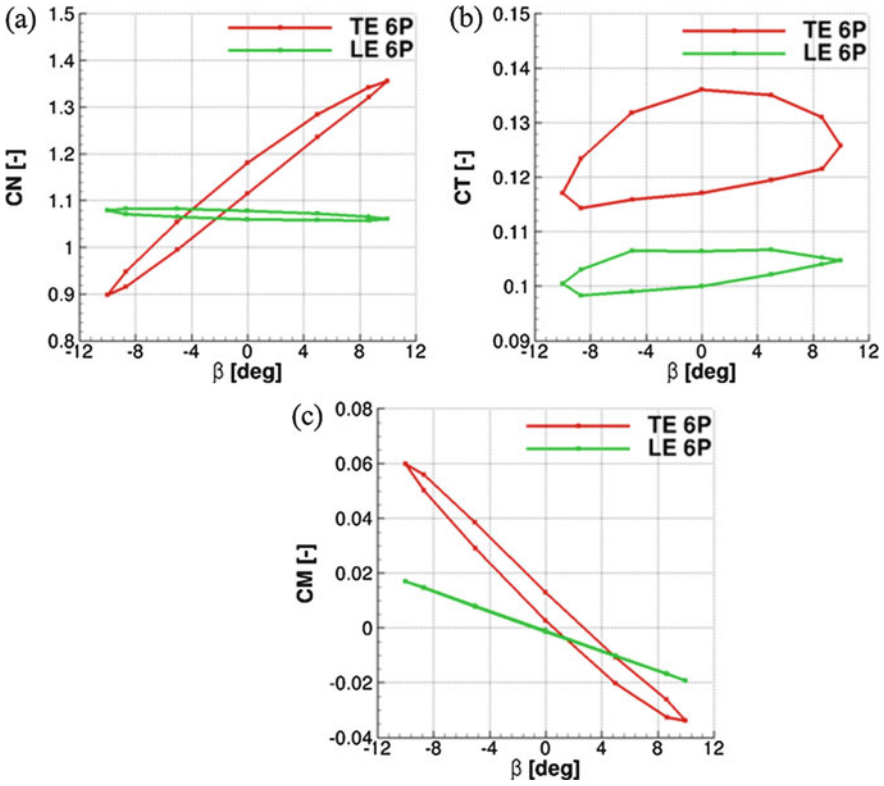

Fig. 7.12 Comparison of the performance of TE and LE flaps based on the non-dimensional coefficients as function of flap deflection angle. (**a**) Normal force coefficient. (**b**) Tangential force coefficient. (**c**) Pitching moment coefficient

7.9 Summary

The results showed a significant, but localized effect of the flap deflection on the distribution of the loads. The trailing edge flap can modify both thrust force and pitching moment, whereas trailing edge flap mostly affects the pitching moment. That suggests, that trailing edge flaps can be used to locally change aerodynamic loads on the blades, possibly eliminating the adverse effect of the blade passing in front of the tower. On the other hand the leading edge flap can be used to counter the additional pitching moment created by the deflection of the trailing edge flap.

Acknowledgments Results were obtained using the EPSRC funded ARCHIE-WeSt High Performance Computer (www.archie-west.ac.uk). EPSRC grant no. EP/K000586/1.

References

Bak C, Zahle F, Bitsche R et al (2013) The DTU 10-MW reference wind turbine. In: DTU Orbit – The Research Information System. Available via Technical University of Denmark. http://orbit.dtu.dk/files/55645274/The_DTU_10MW_Reference_Turbine_Christian_Bak.pdf. Accessed 06 Apr 2016

Carrión M, Woodgate M, Steijl et al (2013) Implementation of all-Mach Roe-type schemes in fully implicit CFD solvers – demonstration for wind turbine flows. Int J Numer Methods Fluids 73(8):693–728. doi:10.1002/fld.3818

Carrión M, Steijl R, Woodgate M et al (2014) Computational fluid dynamics analysis of the wake behind the MEXICO rotor in axial flow conditions. Wind Energy 18:1025–1045. doi:10.1002/we.1745

Carrión M, Woodgate M, Steijl R et al (2015) Understanding wind-turbine wake breakdown using computational fluid dynamics. AIAA J 53(3):588–602. doi:10.2514/1.J053196

Dubuc L, Cantariti F, Woodgate M et al (2000) A grid deformation technique for unsteady flow computations. Int J Numer Methods Fluids 32(3):285–311

Eisenstat S, Elman H, Schultz M (1983) Variational iterative methods for nonsymmetric systems of linear equations. Siam J Numer Anal 20:345–357. doi:10.1137/0720023

Gómez-Iradi S, Steijl R, Barakos G (2009) Development and validation of a CFD technique for the aerodynamic analysis of HAWT. J Sol Energy Eng. doi:10.1115/1.3139144

Jameson A (1991) Time dependent calculations using multigrid, with applications to unsteady flows past airfoils and wings. In Abstracts of the 10th computational fluid dynamics conference, fluid dynamics and co-located conferences, AIAA, Honolulu, 24–26 June 1991

Jarkowski M, Woodgate M, Barakos G et al (2013) Towards consistent hybrid overset mesh methods for rotorcraft CFD. Int J Numer Methods Fluids 74(8):543–576. doi:10.1002/fld.3861

Osher S, Chakravarthy S (1983) Upwind schemes and boundary conditions with applications to Euler equations in general geometries. J Comput Phys 50:447–481. doi:10.1016/0021-9991(83)90106-7

Rieper F (2011) A low-Mach number fix for Roe's approximate Riemann solver. J Comput Phys 230(13):5263–5287. doi:10.1016/j.jcp.2011.03.025

Spalart P, Jou W, Strelets M et al (1997) Comments on the feasibility of LES for wings, and on a hybrid RANS/LES approach. In: Liu C, Liu Z (eds) Proceedings of the first AFOSR international conference on DNS/LES, Louisiana, 1997

Steijl R, Barakos G (2008) Sliding mesh algorithm for CFD analysis of helicopter rotor-fuselage aerodynamics. Int J Numer Methods Fluids 58:527–549. doi:10.1002/fld.1757

Steijl R, Barakos G, Badcock K (2006) A framework for CFD analysis of helicopter rotors in hover and forward flight. Int J Numer Methods Fluids 51(18):819–847. doi:10.1002/fld.1086

Van Leer B (1979) Towards the ultimate conservative difference scheme, a second order sequel to Godunov's method. J Comput Phys 32:101–136

Part II
Enabling Technologies for Drivetrain and Gearbox Analysis